ABSTRACT

Title of Document: HIGH FREQUENCY ELECTRICAL TRANSPORT PROPERTIES OF CARBON NANOTUBES

Enrique Darío Cobas, Doctor of Philosophy, 2010

Directed By: Professor Michael Fuhrer, Physics Department

Carbon nanotubes (CNTs) have extraordinary electronic properties owing to the unique band structure of graphene and their one-dimensional nature. Their small size and correspondingly small capacitances make them candidates for novel high-frequency devices with cut-off frequencies approaching one terahertz, but their high individual impedance hampers measurements of their high-frequency transport properties. In this dissertation, I describe the fabrication of carbon nanotube Schottky diodes on high-frequency compatible substrates and the measurement of their rectification at frequencies up to 40GHz as a method of examining the high-frequency transport of individual CNTs despite their high impedance. The frequency dependence of the rectified signal is then

used to extract the Schottky junction capacitance as a function of applied bias and ambient doping and to look for resonances which might be a signature of a room-temperature Luttinger Liquid.

HIGH FREQUENCY ELECTRICAL TRANSPORT PROPERTIES OF CARBON NANOTUBES.

By

Enrique Darío Cobas

Dissertation submitted to the Faculty of the Graduate School of the
University of Maryland, College Park, in partial fulfillment
of the requirements for the degree of
Doctor of Philosophy
2010

Advisory Committee:
Professor Michael Fuhrer, Research Advisor and Chair
Professor Ichiro Takeuchi, Academic Advisor
Professor Romel Gomez
Professor John Cummings
Professor Steven Anlage, Dean's Representative

Dedication

To failed experiments, blind alleys, dead-ends, abandoned projects, unpublishable results and the overlooked researchers who drew those short straws but without whom science would not move forward.

Acknowledgements

My nearly ten years as Michael's student, first as an eager unpaid undergraduate and later as a graduate student, has been not just an educational experience leading to a certificate, nor just an accumulation of skills enabling the future career I certainly look forward to, although it is both of those things. Rather, it has been ten years of doing what I find emotionally rewarding, ten years surrounded by like-minded and brilliant people. It has been ten years producing and contributing to brand-new research and of being what I have long wanted to be: a scientist. It's also been years of working largely unencumbered (or shielded from) more mundane concerns of utilitarianism and capitalism.

Scientific research, by definition probing the unknown, is challenging, time-consuming and often frustrating. Probable and frequent failure is frustrating enough without having to justify our painfully difficult, slow and often doomed efforts in terms of speculation about the future. I am grateful to my research advisor, Michael Fuhrer, for allowing his students to pursue our projects free from pressures of project funding and marketing that he is more exposed to, and likewise to this university, to academia in general and to the people at funding agencies that see inherent value in scientific progress. Credit for nearly ten years of valuable advice, support, education and discussion regarding this and previous projects goes to Michael. The support, expertise and advice of Steven Anlage has likewise been invaluable to me for several years and I am immensely grateful to him.

In projects involving new and unfamiliar techniques, such as this one, the final product presented is the result of many failures and learning experiences. In a full recounting, all of these dead ends and time-consuming troubleshooting experiments would be described in detail to convey the full difficulty of the achievement. But neither writing nor reading about failures is as enjoyable as discussing success, so most failures are conveniently forgotten. However, that also fails to acknowledge the contribution of people who encountered those failures and worked to find the solutions that were implemented. Those people contributed something intangible but crucial to this project: new knowledge. Alexander Manasson designed the improved high-frequency device geometry and the photo mask layout, and troubleshooted the CNT alignment recipe and the photolithography process with me. Daniel Black somehow performed dozens of nanotube growth and imaging trials while juggling a full load of freshman year engineering courses. Thanks also go to Paola Barbara at Georgetown University and her collaborator, Mohamed Rinzan, for access and assistance performing a rectification experiment using their facilities.

This project would have been even more challenging or impossible without the advice and work of our valuable clean room staff including Tom Loughram, Jon Hummel and John Abrahams. In addition, since our research group facilities are kept in working order by fellow students, the parts of the project necessitating use of an atomic force microscope, automated probe station or scanning electron microscope are also attributable to Tarek Ghanem, Alex Curtin, Adrian Southard and Dan Lenski. Dan's

programming assistance also helped the data analysis in Chapter 6 take days instead of months and saved me from a tedious existence reviewing C++.

Ten years is a long time and I've had the pleasure of working with over a dozen very pleasant and interesting students and post-docs throughout. In particular, Todd Brintlinger, from whom I learned much about putting together a lab, working in one and generally getting things done. Only later did I realize he had only just learned some of those things himself. I am still seeking his advice today. I have long missed the humor, attitude and general good company of Tobias Durkop and Anthony Ayari, the balance of Yung-Fu Chen, who restrains his kindness and benevolence lest it overwhelm us, the dirty humor and quieter introspection of Gokhan Esen, the loud, echoing laughter of Tarek Ghanem, as well as his insight into more important life matters. I will miss chats with Chaun Jang about physics, careers and more, Dan Lenski's enthusiasm at anything technological or linguistic, and many memorable discussions with Alex Curtin about social issues, trust and friendship, in addition to cars and bikes, of course.

Fortunately, many of the friendships that were forged in this research group remain frequently revisited today. Todd Brintlinger and Stephanie Getty remain friends of mine (and certainly each other!), and most importantly, Adrian Southard will likely remain a close friend for life. Although our regular work-outs have been suspended these last few weeks of dissertation writing, don't worry Adrian, they should resume shortly.

Finally, none of this work would have been possible at all without the patience and support of my parents, Nellys and Ruben, and my wife, Sarah. Although they may not share or understand my passion for this career, I'm grateful that they enabled me to selfishly pursue it anyway.

Table of Contents

List of Tables

List of Figures

Figure 4.4 Optical image of an electrode set and source/drain probes during microwave measurement. The microwave horn antenna was positioned orthogonal to the probes axis (top, not shown) with the polarization oriented in-plane with the probes. Another electrode set can be seen at the top edge of the image.

Figure 4.5. DC current-voltage characteristics of a CNT Schottky diode (black line) and corresponding fit to Eqn. 1 (red circles) with $n = 1.00$ and $R_s = 420\text{k}\Omega$. The data shown is from Device 2 pictured in Figure 4.2.

Figure 4.6. Rectified output signal from a CNT-SD as a function of dc bias under various powers of 7GHz (red squares) and 18GHz (blue triangles) microwave excitation. The corresponding microwave intensities are (top to bottom) -14dBm, -17dBm and -20dBm for the 7GHz data and -8dBm and -11dBm for the 18GHz data. Inset shows the model equivalent circuit, ignoring the stray capacitance which is bias-independent.

Figure 4.7. Rectified current ratio at 7GHz vs.18GHz as a function of dc bias. Solid lines are calculated from the measured junction resistance data $R_j(V)$ and the model equivalent circuit in figure 3 for junction capacitances $C\text{j} = 10^{-19}$ F (blue circles), 10^{-18} F (green rhombi), 10^{-17} F (orange squares), 10^{-16} F (red triangles). The experimentally observed ratio (scaled to 1.0 at high bias) is shown as black stars.

Figure 5.1. SEM micrograph of a horizontally aligned CNT film produced for this experiment at U. Maryland. The scale bar is 20μm, indicating a tube density of approximately 1 μm^{-1}.

Figure 5.2. Left: Statistical distribution of CNT diameters resulting from a growth recipe using ferritin catalyst on an r-plane sapphire substrate, measured by AFM. Right: AFM image of aligned CNTs on quartz substrate, showing multiple tubes with diameters under 2 nm. All synthesis, imaging and measurements performed by myself, for this work, at University of Maryland.

Figure 5.3. Design drawing of the CPW CNT-SD array including two-port diodes and transmission lines (top) and one-port devices (center and bottom). Highlighted devices (cyan outline) are the shortest channel lengths. The corner features are alignment markers. A thick transparent border (left and right edges) was created to aid mask alignment.

Figure 5.4. Left: Drawing of two one-port CNT-SD CPW devices. Contact pads are 100 μm wide, 150 μm in pitch (50 μm gap). The Schottky contact (black outline) is the inverse U-shaped contact comprising both outer pads. The Ohmic contact (blue) is the thinner center electrode. Right: Close-up view showing the active device area (highlighted by a red box) where nanotubes remain after patterned plasma etching.

Figure 6.2. Microwave rectification parameters for device A1 under ambient conditions. (left) Observed cut-off frequency (black circles) as a function of junction voltage (V_J) compared to simulated results of equation 6.2 using the observed R_S and $R_J(V_J)$ values and junction capactances of 1 aF (red line), 10 aF (green line) and 100 aF (blue line). (right) Junction capacitance as a function of junction voltage (V_J) clculated from equation 6.3.

Figure 6.3. Microwave rectification parameters for device D2 under ambient conditions. Left: Observed cut-off frequency (black circles) as a function of junction voltage (V_J) compared to simulated results of equation **6.2** using the observed R_S and $R_J(V_J)$ values and junction capacitances of 1 aF (red line), 10 aF (green line) and 100 aF (blue line). Right: Junction capacitance as a function of junction voltage (V_J) calculated from equation 6.3.

Figure 6.6. Junction capacitance corresponding to observed cut-off frequency values, according to equation 6.3, for diode A1 (top left), D2 (top right) , M2 (bottom left) and M6 (bottom right), measured under high vacuum to reduce doping. A weak positive trend is evident in the shorter, small-capacitance diodes (D2, M2 and M6). Diode A1 is 20 μm long, and appears dominated by stray capacitance of about 100 aF.

Figure 6.7. A three-dimensional rendering (left) of the first simulation geometry: a nanotube, modeled as a perfectly conducting cylinder (red), is placed on top of a quartz substrate (green). The electrode (blue) is modeled as a 100 nm thick rectangular conductor with an attached 50 nm nanotube parallel to the channel nanotube, modeling the situation in device A1. The separation, *D*, between channel and electrode is better seen in the close-up image of the contact area (right).

Figure 6.8. Capacitance for the model shown in figure 6.7 as a function of size of the simulated region (boundary position) in units of percentage of the size of simulated objects along each dimension. For a 2μm x 1μm x 1μm simulated device, setting X and Y padding to 100% increased the simulated region to 6 μm x 6 μm x 1 μm. All boundary conditions explored (including 125% Z-padding) had a negligible effect on capacitance.

Figure 6.9. Cross-section of the electric field magnitude (left) and a close-up of the field intensity near the depletion zone (right).

Figure 6.10. A 3D vector plot of the electric field intensity and direction in the model shown in figure 6.7. The infinitely sharp boundary between the cylindrical nanotube and the planar substrate surface leads to very high localized electric fields.

Figure 6.11 A three-dimensional rendering (left) of the overall simulation geometry, and a close-up of the simulated junction (a gap between a conducting cylinder and an electrode). Unlike in the first simulation, here the nanotube is embedded in quartz,

avoiding the sharp boundaries of a perfect cylinder meeting an ideal plane. The nanotube diameter is 5nm.

Figure 6.12. Capacitance as a function of simulation parameters a) depletion length, represented by the gap between the conducting cylinder and the electrode, and b) nanotube radius, for the geometry shown in figure 6.11.

Figure 6.13. Calculated capacitance as a function of a) nanotube channel length and b) electrode width for nanotubes of length 1μm (black squares), 6μm (red circles) and 11μm (green triangles).

Figure 6.15. Rectified current data (unprocessed) from device M2 a) in ambient, Log scale, showing rectified current of 100nA at 40GHz under 1.4 V of forward bias, and b) in vacuum, linear scale. Plot b shows a decrease in rectified current near 25GHz for bias values between 0.7 V and 1.0 V, followed by a recovery at higher frequencies.

Figure B.1. Microwave rectification parameters for device J3 under ambient conditions. (left) Observed cut-off frequency (black circles) as a function of junction voltage (V_J) compared to simulated results of equation 6.2 using the observed R_S and $R_J(V_J)$ values and junction capactances of 1 aF (red line), 10 aF (green line) and 100 aF (blue line). (right) Junction capacitance as a function of junction voltage (V_J) calculated from equation 6.3, fitted to an exponential dependence on junction voltage using Equation B.1.

Figure B.2. Left: SEM image of diode J3, comprised of a small but unknown number of nanotubes buried under photoresist residue. Right: Schottky junction IV curve for device J3 in terms of junction bias (black circles) with a fit to the diode equation (red line).

Chapter 1

Introduction to Carbon Nanotubes

"*I am among those who think that science has great beauty. A scientist in his laboratory is not only a technician: he is also a child placed before natural phenomena which impress him like a fairy tale.*" – Marie Curie

1.1 Overview

The aim of this work was to measure high-frequency electrical transport in carbon nanotubes (CNTs). The remainder of chapter 1 is an introduction to carbon nanotubes, their composition, structure, synthesis mechanisms and properties, with a particular focus on electronic properties relevant to this work. This chapter attempts to explain why carbon nanotubes are appealing for new high-frequency devices and why understanding their transport properties at these frequencies is a worthwhile objective. In Chapter 2 I review novel phenomena that arise in one-dimensional conductors. Some of these phenomena hamper the measurement and technological integration of one-dimensional electronic materials, others make possible new kinds of devices, and some do both simultaneously. Chapter 3 introduces the method used in this work, i.e. measurement of rectified current from carbon nanotube Schottky diodes (CNT-SDs). As such, it includes a review of Schottky diodes, their nature, formation, properties and models governing their behavior both in bulk and new one-dimensional semiconductors.

Chapter 4 describes my successful first attempt at fabrication of CNT Schottky diodes (CNT-SDs) as well as their dc and microwave characterization. Much of the material in chapter 4 was published by myself and my advisor Michael Fuhrer, in Applied Physics Letters 93, 043120 (2008) and online supplementary materials. The preliminary results in chapter 4, combined with newly developed experimental techniques, pointed the way to significant improvements to the experiment. Better control of nanotube diameters and placement, impedance-matched (50 Ω) coplanar-waveguide device geometries and vastly improved RF measurement equipment are some of the changes implemented and described in detail in chapter 5. Finally, chapter 6 presents several experimental results employing the technique of microwave rectification by carbon nanotube Schottky diodes. Specifically, the extraction of the Schottky junction capacitance and demonstration of rectification of signals up to 40 GHz (limited by equipment). The results are in agreement with electrostatic simulations and have implications for future high-frequency electronics using 1D conductors.

1.2 Carbon Nanotubes

Carbon nanotubes are a family of seamless, hollow, cylindrical all-carbon molecules with diameters as small as 1nm. Their walls are composed entirely of graphene, a hexagonal lattice of sp^2 bonded carbon atoms which is one layer of graphite[1] (Figure 1.1). Although theoretically of unlimited length, experimentally the longest[2] CNTs created are currently about 18cm. In addition to dozens of various

types, CNTs exist in single-walled varieties (SWCNTs shown in Figure 1.1) and mutli-walled varieties (MWCNTs, shown in Figure 1.2) composed of various concentric SWCNTs. CNTs have a variety of extraordinary physical, electronic and thermal properties.

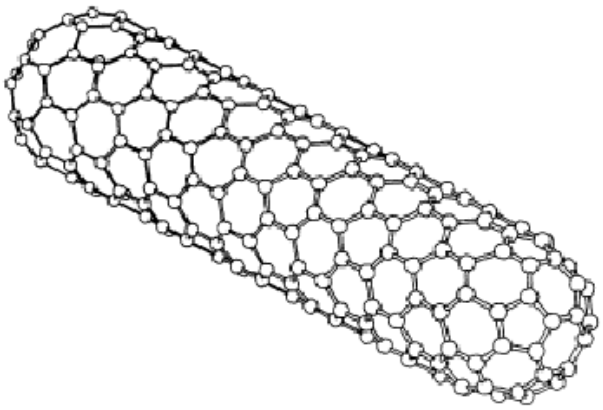

Figure 1.1. A schematic of a carbon nanotube. Adapted from reference 1.

Their small size and large aspect ratio makes CNTs a bridge between the macro world we directly experience and nano scale of interesting quantum phenomena we are still exploring and hope to exploit. They are narrow enough to behave as simple, perfect 1D structures and also long enough to be accessible to current-day fabrication, imaging and measurement techniques. Their spontaneous self-assembly makes them easy to obtain with low-cost starting materials and equipment using established processes (chemical vapor deposition (CVD)[3-5], arc discharge[6], laser ablation[7]). The development of scanned probe microscopy (SPM) techniques such as scanning tunneling microscopy (STM)[8] and atomic force microscopy (AFM)[9] and their variations, as well the availability of scanning and transmission electron microscopy (SEM and TEM resepctively) has enabled detailed

characterization of these molecules. CNT's chemical inertness allows their structure and properties to be mostly unaffected by exposure to air and to aqueous and organic solvents which are a part of microelectronics fabrication techniques. Lastly, their excellent and varied electrical properties lend themselves well to established electric measurement techniques and equipment and also imply potential technological applications.

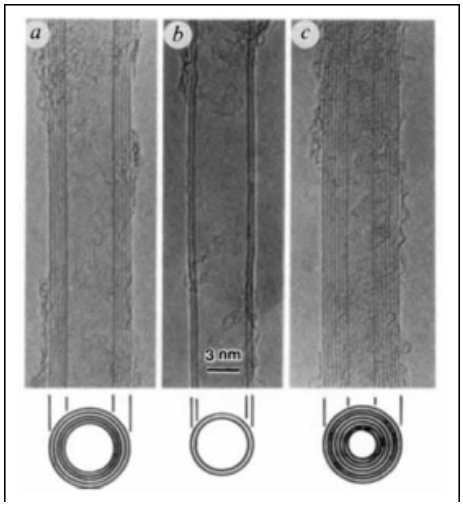

Figure 1.2. Multi-Walled Carbon Nanotubes (MWCNTs) as imaged by Iijima[1].

As silicon transistor features sizes shrink beyond 22nm[10], the advantages of self-assembled metallic and semiconducting molecules with line widths of 1nm and superior electrical and thermal conductances become obvious. CNTs' small size and associated capacitances[11-13], combined with their high current density[14], leads to intrinsic cut-off frequencies (1/RC) in excess of 1THz[15-20]. Consequently, carbon nanotubes have been explored as a future basis for high-frequency, low-power, low-cost and flexible electronic devices as well as sensors and fibers. CNT's nanoscale

dimensions lead to interesting phenomena unique to 1D conductors and nanostructures like quantized conductance[21-23], quantized capacitance[24], kinetic inductance [25], coulomb blockade[26] and Luttinger liquid[27-30] transport. These novel phenomena will be reviewed in chapter 2.

1.3 Brief History of Carbon Nanotubes

The early history of CNTs is a story of the failure of communication and imagination. CNT-like structures were discovered and characterized multiple times in TEM images dating back to the work of Bykov, Lukyanovich and Radushkevich in 1952[31] (Figure 1.3). As explained by Monthioux and Muznetsov[32], several other research groups observed carbon nanotubes via TEM between 1952 and 1991. Indeed, a patent was granted in 1987 for a method of producing "cylindrical discrete carbon fibrils," composed of "continuous layers of ordered carbon atoms," with diameters as small as 3.5nm[33]. Unfortunately, in most of these cases carbon nanotubes were seen as a curious or undesirable impurity, an obstacle to achieving some other goal. It was not until Iijima's experimental observation in 1991 of MWCNTs (Figure 1.2) in the byproduct soot from fullerene manufacture (as opposed to the catalytic growth on metals described in earlier works), his careful identification of these objects as seamless carbon cylinders[1] and the near-simultaneous (but uncorrelated) theoretical studies of the properties of SWCNTs,[34-36] that carbon nanotubes became an intense area of study. Furthermore, creation of SWCNTs was

not experimentally confirmed until 1993 with the works of Iijima and Ichihashi[37] and Bethune et al.[38]

The recognition of carbon nanotubes' significance owes much to events that unfolded in the 1980s, including the discovery of fullerenes by Richard Smalley in 1985 [39], the invention of scanned probe microscopy by Binnig and Rohrer [8] in 1982, Richard Feynman's advocacy of nano-science, the publication of Engines of Creation by Eric Drexler in 1986[40] (which popularized the nascent field of nanotechnology), and progress and interest in shrinking integrated circuits past the micron scale. Each of these events helped open our minds to the possibility of these beautifully simple, symmetric all-carbon molecules and their potential applications and gave us the tools to see and manipulate them, thereby motivating further experiments and discoveries.

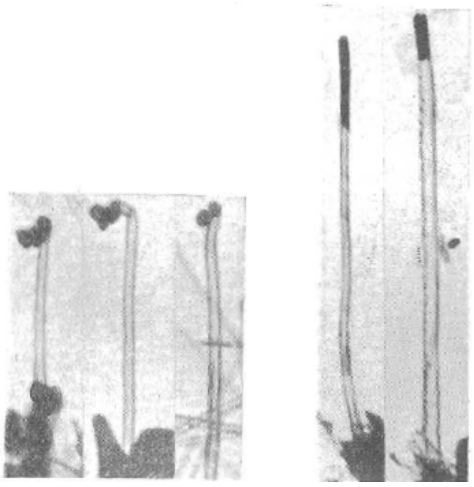

Figure 1.3. Carbon nanotubes as imaged by Radushkevich and Lukyanovich in 1952.[31]

1.4 Physical Structure and Properties

A carbon nanotube is a seamless hollow cylinder with walls of hexagonally sp^2-bonded carbon atoms (i.e. Graphene, a single layer of graphite). The orientation of the nanotube axis with respect to the lattice vectors of the graphene wall can vary, so a pair of integer indexes *a,b* is used to uniquely identifiy a type of nanotube (its "chirality") and reflects its geometrical structure. These indices compose a vector on the two-dimensional graphene lattice, $\boldsymbol{C} = a\boldsymbol{a}_1 + b\boldsymbol{a}_2$ where $\boldsymbol{a}_1$ and $\boldsymbol{a}_2$ are the lattice vectors of graphene. This 'roll-up' vector represents the circumference of the nanotube relative to that lattice, such that the nanotube axis is perpendicular to it. Besides the length, the roll-up vector *(a,b)* is all that is needed to completely specify the physical structure of a nanotube and its electronic and other properties. Limitations on bond strain and realistic catalyst particle size place lower and upper limits, respectively, on the diameter of synthesized CNTs and reduce the number of observed nanotube types to a few hundred. Nanotubes where the two indices are equal (a=b) are called *armchair* nanotubes (Figure 1.4a), and those in which index a is zero (a=0) are referred to as *zigzag* nanotubes (Figure 1.4b). All other types are called chiral nanotubes. Because there are hundreds of species of nanotubes, it is important to note that properties can vary greatly among them. Mechanically, their stiffness, tensile strength and thermal conductivity have been measured at 4TPa[41], 63GPa[41] and 3,000 Km/W[42], all values rivaling diamond as the strongest and most

thermally conductive material known to humans. Their electronic properties are just as surprising, more relevant to this work, and deserving of closer attention.

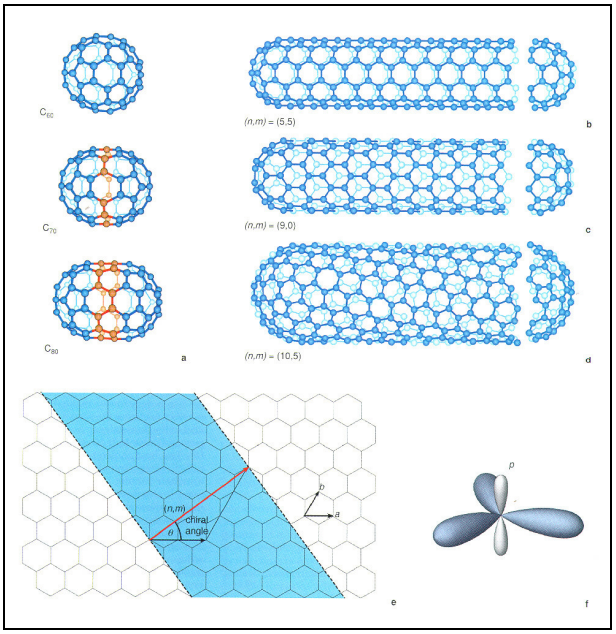

Figure 1.4. Artistic representation of a) C_{60}, C_{70} and C_{80} buckminsterfullerenes, b) an armchair (a=b) carbon nanotube, c) a zig-zag (b=0) carbon nanotube, d) a chiral carbon nanotube, e) the roll-up vector f) the triangular sp^2 orbital hybridization that enables the hexagonal carbon lattice. Image courtesy of Richard Smalley.

1.5 Electronic Structure and Properties

The sp^2 orbital hybridization present in CNTs results in a conjugated hexagonal network of overlapping π-orbitals, which imparts excellent electrical conductance to CNTs as it does to graphite. The electronic band structure of carbon nanotubes are fundamentally modifications of the band structure of graphene. This structure was calculated by Wallace[43] as

$$E(k) = E_F \pm \gamma_0 \sqrt{1 + 4\cos(\sqrt{\frac{3k_x a}{2}}\cos(\frac{k_y a}{2}) + 4\cos^2(\frac{k_y a}{2})} \qquad \text{(Eq. 1.1)}$$

where γ_0 is the nearest-neighbor overlap, a is the interatomic bond distance and k_x and k_y are the momentum vectors on the two-dimensional graphene lattice. In this structure, the valence and conduction bands meet at a single location, with no overlap, at the K-points in the corners of the hexagonal Brillouin zone. In proximity to this point (at low energy) the valence band can be approximated as a cone and the conduction band as an inverted cone (Figure 1.5).

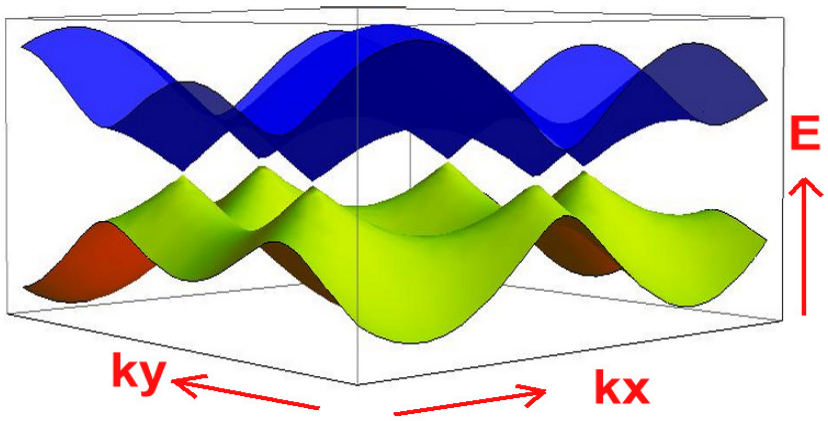

Figure 1.5 Graphene band structure. The valence band (yellow) and conduction band (blue) intersect at six points (K-points) on the Fermi surface but do not overlap, making graphene and metallic CNT zero-bandgap semiconductors. Further, the band structure near the K-point is approximately conical.

The cylindrical topology of CNTs naturally introduces a periodic boundary condition on the momentum vector pointing along the circumference of the nanotube. This restriction reduces the continuous allowed k_y values to a discrete set where

$$k_y \cdot C = 2\pi n \qquad \text{(Eq. 1.2)}$$

figuratively slicing the graphene band structure into various possible cross-sections. These sections take the shape of conical sections near the K-point (Figure 1.6).

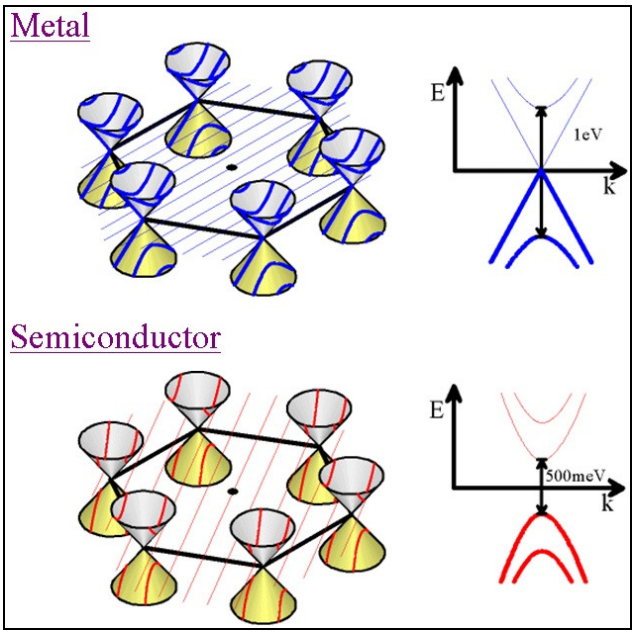

Figure 1.6. Schematic showing the quantization of the 2D graphene band structure into a set of allowed k-vectors. Image courtesy of Michael Fuhrer.

The distance (in momentum space) from the allowed k values to the K-point where the conduction and valence bands meet depends on the roll-up vector (n,m). Wider nanotubes will exhibit less quantization, having a larger set of allowed k_y

values within the finite graphene band structure and bands that lie closer to the K-point. This results in an inverse relationship between tube diameter and band gap of approximately $d / 750 = E_g$ with d in nanometers and E_g in electron volts[44]. For nanotubes with a diameter of 19.5nm, any energy gap between valence and conduction bands will be smaller than kT at room temperature and such a nanotube would not exhibit gate-controlled conductance modulation. If the difference between the indices is a multiple of three ((a – b) = 3i, where i is an integer), the allowed k_y values include the K-point and the band gap is theoretically zero, yielding metallic nanotubes with a massless dispersion relation similar to graphene's. However, more recent experimental studies have revealed that some types of such nanotubes have a small band gap due to subtle curvature effects[45].

1.6 Formation Mechanism and Production Methods

Carbon nanotubes self-assemble given the right conditions, generally a carbon gas atmosphere (e.g. methane, ethylene, ethanol or carbon monoxide) high temperature (700 – 1200C) and their assembly can be catalyzed by metal nanoparticles (e.g. Iron, Cobalt). The growth mechanism is thought to be a vapor-liquid-solid (VLS)[46, 47] process where the carbon gas species dissociates and the carbon becomes dissolved in the metal particle. Once the particle becomes saturated or supersaturated with carbon, a graphitic hemispherical shell begins to form on the surface, followed by extrusion of the nanotube wall.[48, 49] There have been four common techniques combining these three ingredients: electric arc discharge

between graphite rods[1], thermal decomposition of a metal-containing gas species in a carbon monoxide atmosphere[50], laser ablation of carbon and metal targets[7] and chemical vapor deposition (CVD).[3]

For metal-catalyzed techniques, the catalyst particle composition and size is a critical factor in determining the CNT diameter. Since the bandgap of semiconducting nanotubes is inversely related to their diameter (Section 1.4), small-diameter nanotubes are preferable for semiconducting applications. Furthermore, large-diameter CNTs tend to be of the multi-walled (MWCNT) variety (Figure 1.6), which combines the properties of various CNT types. For example, a MWCNT composed of a metallic CNT within a semiconducting CNT would show gate-controlled conductance modulation but high current leakage in its off state due to current traveling throught the metallic tube.

The main obstacles to technological integration of CNTs are control of nanotube type and placement. All currently available techniques produce a mixture of at best several types of SWCNTs and at worst dozens of SWCNTs and MWCNTs. Efforts to selectively synthesize, destroy or separate certain species or sub-types are ongoing[51,52]. The work described in this thesis uses small-diameter (<2nm) nanotubes produced by metal-catalyzed CVD as described in Chapter 4 and Chapter 5. Due to their small size, these CNTs are presumed to be single-walled (SWCNTs)[47] or few walled MWCNTs although this was not explicitly verified by TEM observations.

Chapter 2

Introduction to One-Dimensional Phenomena

"The fact that we live at the bottom of a deep gravity well, on the surface of a gas covered planet going around a nuclear fireball 90 million miles away and think this to be normal is obviously some indication of how skewed our perspective tends to be."

-Douglas Adams

2.1 Introduction

As integrated circuit technology shrinks towards the nanometer scale, we are forced to re-examine the validity of some assumptions and contend with added complexity. The quantum nature of electronic transport at the nano scale is evident in the form of quantized conductance, or a *minimum channel resistance* that is independent of material properties and has implications for high-frequency devices. Meanwhile, channel lengths shorter than the mean free path result in ballistic conduction. This is particularly important in CNTs which have unusually long mean free paths as a result of reduced dimensionality and reduced carrier scattering. The small number of charge carriers and high carrier velocities in CNTs give rise to quantized capacitance and kinetic inductance that could be ignored in larger devices. Nanotubes' small diameter and hollow structure make them extremely sensitive to changes in their surroundings. Unlike a metal wire which has a solid conductive core of atoms shielded from the outside environment, all of the atoms and conduction channels on a SWCNT are exposed to its environment, and the extremely small

diameter forces electrical signals traveling along the tube to interact with even tiny defects on or near the tube. This sensitivity to environment makes SWCNTs useful as chemical or biological sensors; they could potentially sense the presence of a single molecule disturbing electrical conduction. Several such sensors are being explored.[53-55] This same property implies challenges in manufacturing individual-CNT devices with uniform electronic behavior.

Changes in the dimensionality of the channel give rise to different electronic screening than in traditional electronic devices. Further, assumptions of the Fermi gas model of electric conduction, namely that electron-electron Coulombic interactions are screened out and negligible, must be questioned in a one-dimensional system where electrons are confined together. The resulting theory is Tomonaga-Luttinger Liquid (TLL) theory and provides some interesting predictions. Traditional assumptions in device design, such as a high density of interface states at electronic contact surfaces, must be discarded because few such states exist given such a small channel. These implications of one-dimensionality will be explored below, starting with modifications to the normal definitions of conductivity, capacitance and inductance.

2.2 Quantized Conductance

Looking more closely at the idea of conductance, we find that the classical definition applies to systems with a large number of quantum channels, whereas one-

dimensional conductors like CNTs often have very few channels. The conductance of a single quantum channel between two large reservoirs (source and drain) was formulated by Landauer in terms of transmission of electron waves through the system[56, 57]. I will briefly review the most important result of the Landauer treatment of electrical conduction, namely that the conductance of a 1D wire is finite and quantized in the absence of scattering.

In the Landauer model of electrical transport, the source - drain voltage $V_{sd} = (V_s - V_d)$ can be described as the difference in source drain electric electric potentials $V_s = \mu_s$ and $V_d = \mu_d$, and from the dispersion relation of the system $\varepsilon(k)$, these potentials correspond to a range of momentum states by $\mu_s = \varepsilon(k_s)$ and $\mu_d = \varepsilon(k_d)$. We assume (among other simplifying assumptions) that all the forward-moving states in the system between these two energy levels are occupied. The resulting current is then the electron charge times the sum of all available states between k_s and k_d :

$$I = \frac{e}{h}\int_{k_d}^{k_s}\frac{d\varepsilon(k)}{dk}dk = \frac{e}{h}\int_{\mu_d}^{\mu_s}d\varepsilon = \frac{e}{h}\varepsilon(\mu_s - \mu_d) = \frac{e^2 V_{SD}}{h}$$

(Eq. 2.1)

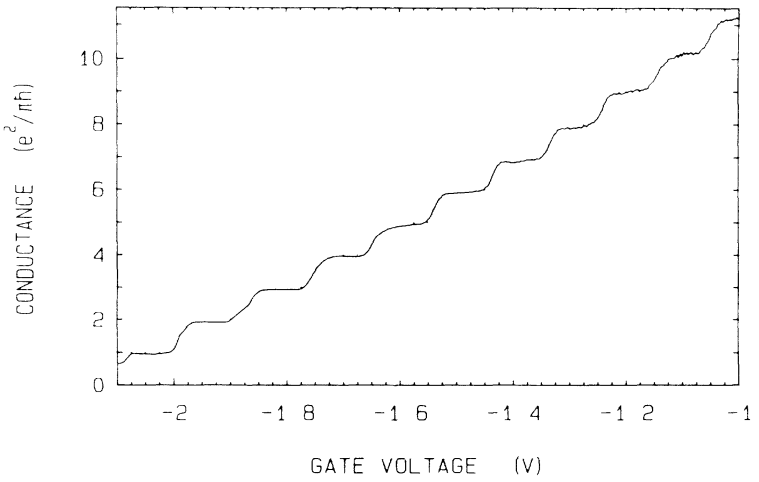

Figure 2.1. Point-contact conductance in a two-dimensional electron gas, exhibiting conductance plateaus in integer values of G_0. From Vanwees.[21]

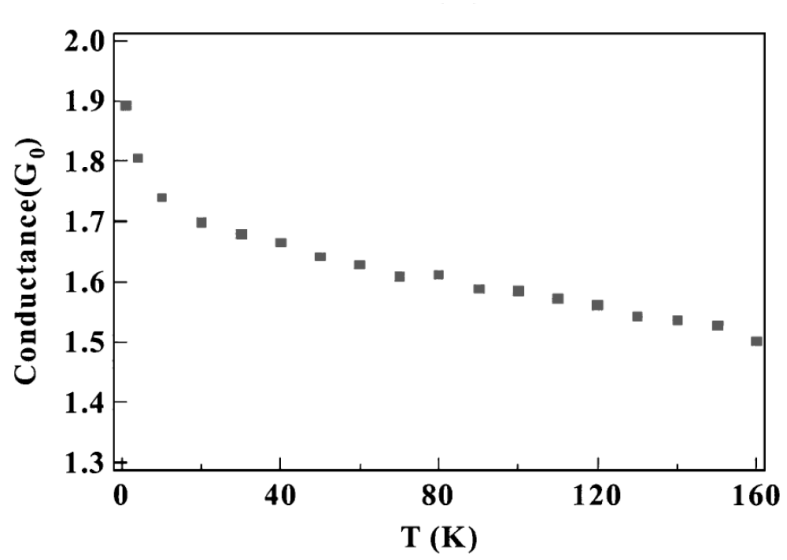

Figure 2.2. Conductance in a single carbon nanotube in terms of the conductance quantum (with $2G_0$ representing perfect conductance) as a function of temperature. Adapeted from Kong et al[58]

The conductance is then a constant $I / V = e^2/h = \frac{1}{2}G_q$ per channel, independent of other system parameters. This effect was measured in two-dimensional electron gas systems by vanWees et al[21] (Figure 2.1). For carbon nanotubes, band degeneracy and spin degeneracy supply only 4 channels per carbon nanotube, so their ideal quantized conductance per channel is

$$2G_0 \equiv \frac{4e^2}{h} \qquad \text{(Eq. 2.2)}$$

equivalent to a minimum contact resistance of 6.45 kΩ. Loosening the assumptions in this model, for example accounting for finite temperature, or including scattering, only restricts conductance per channel even further. Carbon nanotubes were observed to approach ideal quantum conductance by several groups, including Javey et al[59] and Kong et al[58], as shown in Figure 2.2

This phenomenon establishes a fundamental lower limit for the impedance of a single-tube CNT device at 6.45 kΩ. In comparison, typical microwave equipment is manufactured to an impedance of 50Ω, a compromise between peak power handling and loss in a coaxial air dielectric cable [60], and is closer to the impedance of free space, $Z_0 = 1/\varepsilon_0 c \approx 377\Omega$. Therefore there is a fundamental impedance mismatch between the macroscopic world and that of individual quantum channels: $G_0/Z_0 = 2e^2/\varepsilon_0 hc = 4\alpha$, where $\alpha \approx 1/137$ is the fine structure constant. At microwave frequencies, this mismatch results in very poor power transmission from any macroscopic systems into a 1D system.

Using the transmission line equations, the transmission coefficient T across an impedance mismatch is

$$T = 1 - \frac{Z_L - Z_0}{Z_L + Z_0} \qquad \text{(Eq. 2.3)}$$

where Z_0 and Z_L are the impedances of the transmission line and load, respectively. Using the values 50 Ω and 6.45 kΩ, we obtain a transmission coefficient of 1.5 % so that, even in the ideal situation with perfect contacts and ballistic conduction, 98.5 % of the incident voltage signal will be reflected at the macro-nano interface. In terms of power, a maximum of only $|T|^2 = 0.0225\%$ of the incident power enters the 1D channel. An impedance match of 50 Ω could theoretically be obtained using 130 parallel ideal nanotube channels (1 / 50Ω) = (130 / 6500 Ω). Experiments on single- and few-channel 1D devices are needed to develop and verify physical models for multi-channel 1D devices, and novel techniques are necessary to deal with the obstacles presented by these novel materials.

2.3 Quantum Capacitance

The electrostatic capacitance per unit length, C_{ES}, of a cylinder of diameter d separated from a ground plane by a dielectric of thickness h and dielectric constant ε is given by

$$C_{ES} = \frac{2\pi\varepsilon}{\ln\left(\frac{2h}{d}\right)} \qquad \text{(Eq. 2.4)}$$

Given $\varepsilon_r = 4$ and $h = 1.5$ nm (a very thin dielectric) we can estimate $C_{ES} = 100$ aF/μm for a CNT with diameter of 1.5 nm. However, the reduced dimensionality of CNTs exposes the inherently quantized energy levels available to electron states normally blurred out in larger systems. The quantization of the system's energy levels also leads to a quantized capacitance as the number of charge carriers in the system is noticeably discrete. Following Burke, [25] we take the 1D energy level spacing $\Delta E = h v_f \Delta k / 2\pi$ where $\Delta k = 2\pi / \lambda = \pi \ \ l^{-1}$ and equate it with the energy stored in a capacitor:

$$\delta E = \frac{h v_F}{2l} = \frac{e^2}{C_q} \qquad \text{(Eq. 2.4)}$$

where e is the electron charge, h is Plank's constant, v_F is the Fermi velocity and l is the length of the 1D system. We can then solve for C_q per channel and add a factor of four for band and spin degeneracies to obtain a capacitance-per length

$$\frac{C_q}{l} = \frac{8e^2}{h v_F} = 400 \frac{aF}{\mu m} \qquad \text{(Eq. 2.5)}$$

Alternatively, we can compute the additional charge added to the system by increasing its energy level from E to $(E + \mu)$ as

$$\delta Q = e\int D(E)[f(E+\mu) - f(E)]dE \qquad \text{(Eq. 2.6)}$$

Then, assuming the density of states $D(E)= 4 / \pi v_F$ is constant near the Fermi level, $\delta Q = e^2 D(\mu)\delta V$ and $C_q = \delta Q/\delta V = e^2 D(\mu) = 8e^2/hv_F$, same result as above. This value was confirmed experimentally by Ilani et al[61] and is comparable to the electrostatic capacitance for nanotubes in FET geometries.[24]

2.4 Kinetic Inductance

In bulk conductors, frequent scattering limits the drift velocity of charge carriers to relatively low values, and the large number of carriers is responsible for the magnitude of the current. In such a system, the potential energy stored in the inertia of charge carriers is negligible and the magnetic field created by the current dominates the inductance. In 1D conductors such as nanotubes, however, carriers are few and scattering is reduced (as discussed in the next section), enabling ballistic conduction over micron scales. With few carriers present and velocities near $8x10^5$ m/s, the kinetic energy of moving carriers is no longer negligible compared with the magnetic inductance. The issue of kinetic inductance was examined by Rutherglen and Burke [25] as follows:

$$I = (e^2/h)\,\Delta\mu$$

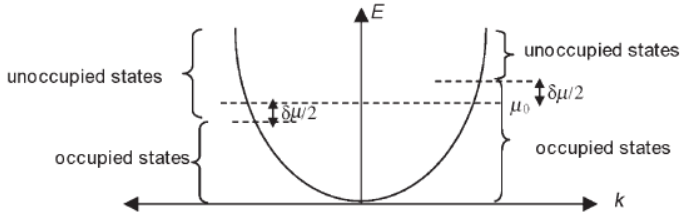

Figure 2.3. Diagram of the dispersion curve for a current-carrying system. Right-moving states are occupied up to $\mu_0+\delta\mu/2$ while left-moving states are occupied up to $\mu_0 - \delta\mu/2$. From Rutherglen. [25]

First, as in section 2.2, the current in any system can be examined quantum-mechanically as a higher population in forward-moving states than in backward-moving states. (Figure 2.3) The energy difference between the highest occupied forward-moving states and the highest occupied backward-moving states is then $\Delta\mu$. The total current is

$$I = \Delta\mu\left(\frac{e^2}{h}\right) \qquad \text{(Eq. 2.10)}$$

Second, for a 1D system with a linear dispersion relation, the single-particle energy level spacing is given by equation 2.4 reproduced here:

$$\delta E = \frac{dE}{dk}\delta k = \frac{hv_F}{l_{nt}} \quad , \qquad \text{(Eq. 2.11)}$$

Accounting for spin degeneracy, the excess number of electrons in forward-moving states due to a Δμ potential is then

$$N = \frac{e\Delta\mu}{2\delta E} = \frac{el_{nt}\Delta\mu}{2hv_F}, \qquad \text{(Eq. 2.12)}$$

and because each electron adds $\delta E = (e\Delta\mu / 2)$, the total energy added by the current is

$$E = \frac{e^2\Delta\mu^2 l_{nt}}{4hv_F} \qquad \text{(Eq. 2.13)}$$

Equating this energy to the energy stored in an inductance gives

$$E = \frac{e^2\Delta\mu^2 l_{nt}}{4hv_F} = \frac{1}{2}LI^2 = \frac{1}{2}L(\Delta\mu^2\frac{e^4}{h^2}) \qquad \text{(Eq. 2.14)}$$

and solving for the inductance per unit length using the Fermi velocity, we get

$$L_K = \frac{hl_{nt}}{2e^2v_F} \approx 4nH/\mu m \qquad \text{(Eq. 2.15)}$$

Further, the magnetic inductance per unit length, L_M, of a typical nanotube suspended above a conducting plane (gate electrode) is estimated at 1pH/μm [25] and thus the kinetic inductance dominates in 1D systems, $L_K \sim 10^4 L_M$.

2.5 Scattering and Phonon Coupling

As mentioned in the previous section, large kinetic inductance is a consequence of the small number of states and reduced carrier scattering. Charge carrier scattering in bulk materials relies on the availability of empty electron states with many different momentum vectors. Electron-phonon scattering often involves small energies and momentum transfers but occur very frequently in macroscopic or even mesoscopic systems and results in a short mean free path under 40 nm even for good conductors like copper and gold at room temperature. In low-dimensionality systems, the available electron states are more limited. In one-dimensional systems there are only forward moving states and backward moving states. The difference in momentum between these two states is large and therefore the majority of room temperature phonons lack the momentum to scatter such charge carriers.[14] The result is that the mean free path of charge carriers in carbon nanotubes can be unusually long, on the order of 1 μm at room temperature [62, 63] and possibly as long as 20 μm[64] at low bias. This value has been measured experimentally as a function of temperature (Figure 2.4) and as a function of gate bias in semiconducting CNTs (Figure 2.5). At high source-drain bias, electrons are accelerated to an energy equal to that of a CNT optical phonon (160 meV) and scatter by emitting this phonon, shortening the mean free path dramatically to about 10 nm. This results in a highly non-linear conductivity with respect to applied bias.

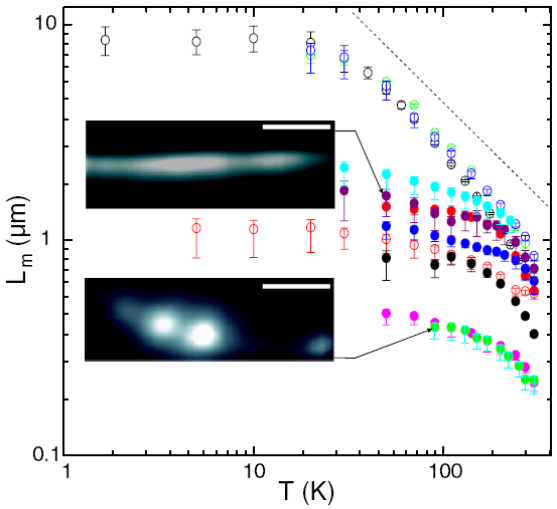

Figure 2.4. Mean free path of metallic (open circles) and semiconducting (filled circles) CNTs as a function of temperature. As shown in Purewal [62].

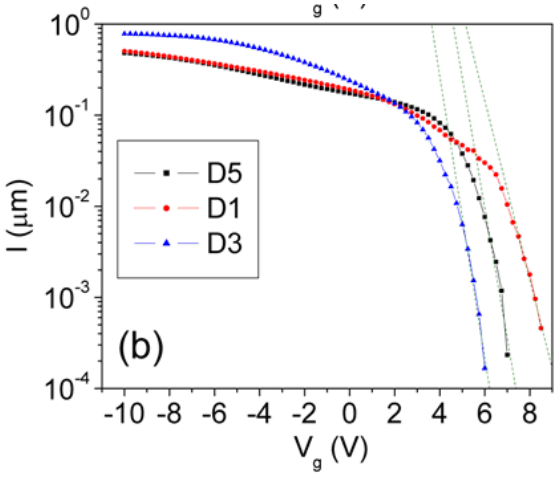

Figure 2.5. Mean free path of semiconducting CNTs as a function of gate potential. As measured by Ghanem. [63]

The limited number of momentum states in CNTs can also result in poor coupling with substrate phonons as recently investigated by Baloch et al[65]. With good thermal contact to palladium islands (thermal contact resistance R_c ~ 4 Km/W)

and poor coupling to the underlying SiN substrate (R_c > 250 Km/W) CNTs act as 'heat pipes,' transferring heat between a source and drain without necessarily dissipating heat efficiently in the intervening substrate. This poor coupling and unusual thermal transport behavior is yet another novel phenomena in one-dimensional materials that has implications for heat dissipation in one-dimensional electronics.

2.6 Electronic Screening

Electronic screening is quite different in one dimension instead of three. In bulk metal-semiconductor junctions for example, the interface between two three-dimensional materials is a two-dimensional surface and the two-dimensional dipole that forms across this interface is capable of shielding both sides of the junction from the charges at the interface. In contrast, interface to a one-dimensional material, such as a CNT, is necessarily zero-dimensional and incapable of effectively shielding the 1D channel from the dipole field at the interface. Therefore the electronic effects of the heterojunction affect transport in the channel for a much longer distance than would be expected in bulk heterojunctions.

The detailed arrangement of charge along the one-dimensional nanotube was studied theoretically by Leonard and Tersoff[66] in the case of an intra-nanotube *p*-*n* junction (equivalent to a *p*-type nanotube an its image charge in a perpendicular

metallic plane). At distances more than λ away from the junction, the charge density qualitatively follows the function

$$\sigma(z) = \sigma_0 \frac{\ln(W/\lambda)}{\ln(x/\lambda)} \qquad \text{(Eq. 2.6)}$$

Where W is the depletion width and λ is a constant of the order of the nanotube radius (~1 nm). The term σ_0 is a constant with value $ef\varepsilon_r^{-1}$ where ε_r is the relative dielectric constant of the medium, f is the doping fraction and e is the electron charge. As displayed in Figure 2.6, the charge density gradient is much more shallow for a CNT channel than would be expected for a planar heterojunction with over 50% of the charge density at 10 nm still present at 50 nm from the junction.

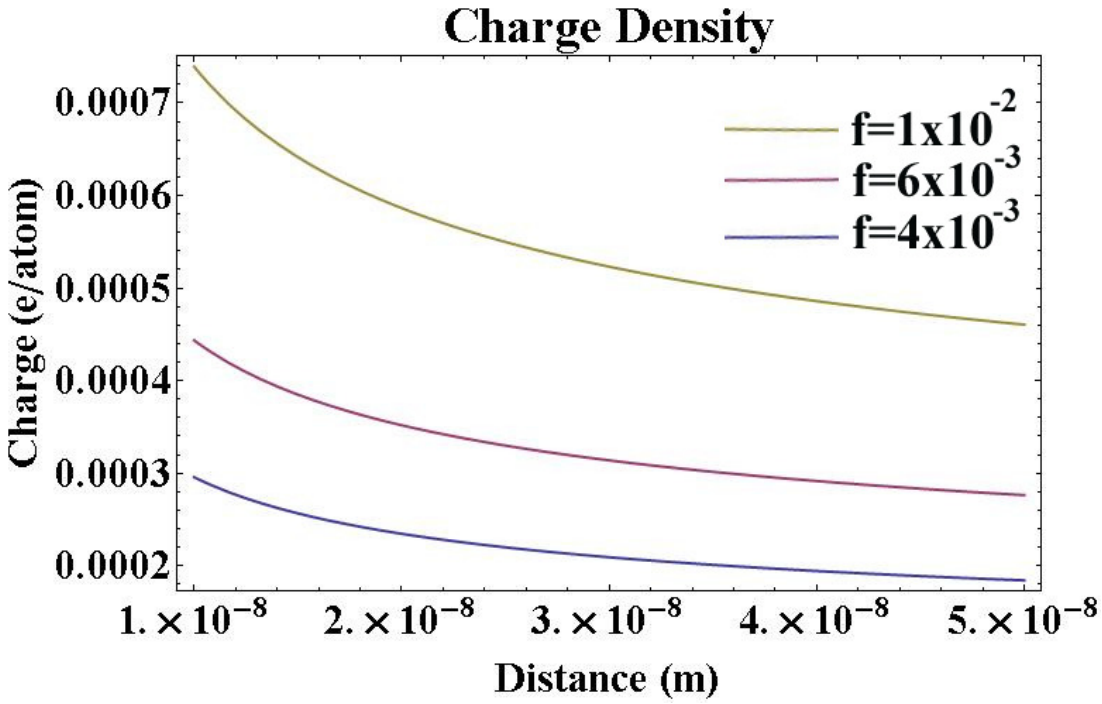

Figure 2.6. Variation of charge density (electrons per nanotube atom) in a carbon nanotube with a *p-n* junction as a function of distance from the junction for three

different doping fractions (f = $4x10^{-3}$, $6x10^{-3}$ and $10x10^{-3}$) calculated according to Leonard and Tersoff [66].

2.7 Tomonaga-Luttinger Liquids and the Plasmon Velocity

In the Fermi gas model, electron-electron interactions are limited to the Pauli exclusion principle and repulsive Coulomb interactions are rightfully neglected due to their improbability given realistic electron densities in a three-dimensional materials. As dimensions are reduced, correlated electron phenomena become significant and must be accounted for. In one dimension, repulsive Coulomb interactions are unavoidable and should dominate transport. A theoretical treatment of conduction in one dimension was done by Sin-itiro Tomonaga[27] and Joaquin Luttinger[28] and refined by others[67].

Although a full examination is too lengthy to incorporate here, intuitively, strong repulsive Coulomb interactions in a 1D channel give rise to transport via charge density wave-like excitations called plasmons, which are conceptually similar to phonons and also boson-like. Even the addition of charge carriers from the system can be considered an excitation of the bosonized Tomonaga-Luttinger Liquid state.

Tunneling conductance of a contact between a bulk metal and such a 1D system is expected to follow a power-law dependence on temperature and voltage,

$G(T) \propto T^{\alpha}$ and $dI/dV \propto V^{\alpha}$ respectively, where the value of the exponent α is different for tunneling into the end of the system or the middle of the system:

$$\alpha_{end} = (g^{-1} - 1)/4 \qquad \text{(Eq. 2.7)}$$

$$\alpha_{middle} = (g^{-1} + g - 2)/8 \qquad \text{(Eq. 2.8)}$$

$$g = \left[1 + \frac{2U}{\Delta}\right]^{-1/2} \qquad \text{(Eq. 2.9)}$$

where U is the charging energy of the system and Δ the single-particle energy spacing. The order parameter g is indicative of the strength and nature of electron-electron interactions, with $g < 1$ for repulsive interactions, $g = 1.0$ for the interactionless Fermi model and $g > 1$ for attractive interactions such as those in superconducting materials. Low-temperature tunneling experiments in CNTs have established the order parameter value to be about $g = 0.25$ [29, 61, 68] for metallic CNTs (and similar for heavily doped semiconducting CNTs). The charge-carrying excitations in these 1D systems are termed plasmons and ought to travel at $v_p = v_f/g$, such that in carbon nanotubes where $v_f = 8 \times 10^5$ m/s, the effective velocity of charge transport ought to be approximately $v_p = 3.2 \times 10^6$ m/s (and also different from the spin transport velocity).

The modification to the charge transport velocity can also be visualized from a transmission line approach using C_Q and L_K as demonstrated by Salahuddin, Lundstrom and Datta[69]: Given quantum capacitance $C_q = G_0\Sigma_m[v_m^{-1}]$, electronic capacitance C_E and kinetic inductance $L_k = G_0\Sigma_m [v_m]$ where v_m is the velocity of mode m and Σ_m is the sum over m modes, the corresponding values are $C_q \sim MG_0v_f^{-1}$ *and* $L_k^{-1} = MG_0v_f$. the velocity of signal propagation v_s in a transmission line is therefore

$$v_s^{\,2} = \frac{1}{LC} \approx \left(\frac{C_E}{C_E C_Q} + \frac{C_Q}{C_E C_Q} \right)\left(\frac{1}{L_k} \right) = v^2{}_f + \frac{MG_0 v_f}{C_E} \quad \text{(Eq. 2.10)}$$

For a system with M=2, this gives propagation velocity

$$v_s = \sqrt{v_f^{\,2} + \frac{8V_f e^2}{hC_E}} \quad \text{(Eq. 2.11)}$$

The time scales involved in measuring this velocity (1 μm / 3.2x10^6 m/s ~ 3.1x10^{-13} s for a 1-micron channel) make a direct experiment difficult. One such challenging experiment was performed by Zhong et al[64] and is very briefly summarized as follows:

A semiconducting CNT channel with source and drain contacts was fabricated on an oxidized Silicon wafer. A local top gate was then patterned on top of the channel, and the silicon wafer served as a global back gate. The back gate was used to

dope the CNT *p*-type while the local gate doped a short portion of the channel *n*-type, as shown in figure 2.7a. Pairs of picosecond current pulses were injected into the CNT channel from a nearby pulsed-laser excited Silicon junction. The delay between the first and second pulse was controlled. As hypothesized, certain delay times caused the arrival of the second left-moving current pulse at the rightmost *p*-*n* junction to coincide with the arrival of the right-moving reflected pulse. The combination resulted in slightly less current passing through the channel for pulse-delay times that resulted in this resonance (figure 2.7b). Unexpectedly, however, for each of three different channel lengths, the delay times which resulted in resonances in the current signal corresponded well to the unrenormalized Fermi velocity of 8×10^5 m/s. The expected resonances due to charge transport at the plasmon velocity were not observed. The secondary resonance peaks in figure 2.7b are indicative of ballistic conduction over a distance of four times the channel length, up to 20 μm for the longest device (l = 5 μm).

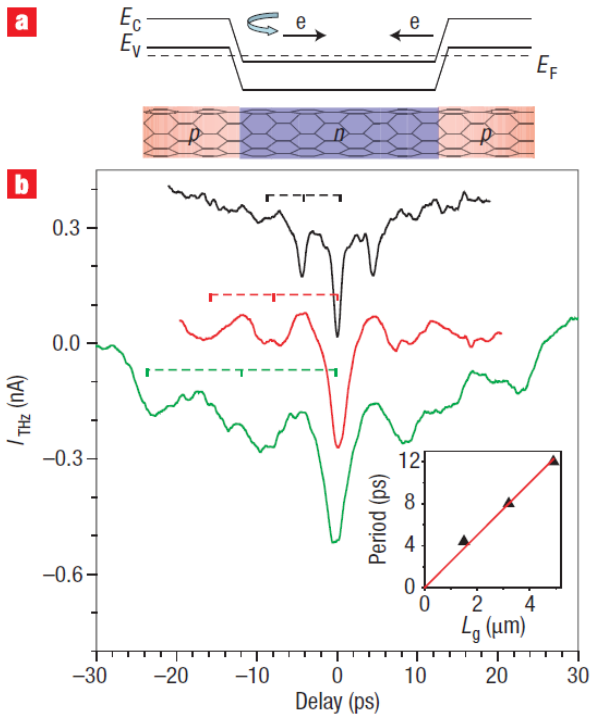

Figure 2.7. A Schematic of Zhong et al's time-domain resonance experiment. a) An *n*-type potential well is formed in the *p*-type CNT channel using local and global gates. b) Current resonances observed for various channel length devices (black, red, green) as a function of pulse delay time. Inset: observed first-resonance period for all three channel lengths. From Zhong et al.[64]

This is a limited review of the novel and unique features of 1D conductors relevant to this work. Some of these properties (e.g. long mean free paths, small electrostatic capacitances) are beneficial and present new opportunities both for experiments probing their behavior and for technological applications. Others, such as quantized conductance, present obstacles to measurement of their high-frequency transport properties. Chapter 3 will present a new technique to enable exploration of

high-frequency properties and phenomena of single and few-tube CNTs despite the high impedance which makes traditional high-frequency techniques difficult.

Chapter 3

Schottky Rectification

"You tell me of an invisible planetary system in which electrons gravitate around a nucleus. You explain this world to me with an image. I realize then that you have been reduced to poetry: I shall never know." – Albert Camus

3.1 Introduction

Given the difficulties of using standard microwave equipment and characterization techniques on inherently high-impedance individual nanostructures such as carbon nanotubes, new techniques are required to probe electrical transport in these systems. In this work I describe one such technique: the use of a Schottky diode formed from one-dimensional semiconductors as an embedded probe of microwave-frequency current in the nanostructure. This chapter will first discuss the nature of a rectifying metal-semiconductor junction, which is the basis of a Schottky diode, then various models governing the current-voltage relationship in such junctions in bulk as well as one-dimensional channels. I will also introduce the simple circuit model of such a system, which will be used repeatedly to analyze results in later chapters.

3.2 Rectifying Metal-Semiconductor Junctions

The rectifying properties of certain metal-semiconductor junctions have been known since the late 19th century and the models for their formation were first proposed by Shockley, Mott and Bardeen.[70] Qualitatively, whenever materials of different work functions come into contact, electrons in the lower-work function material flow into the high-work function material, generating an electric dipole which grows until equilibrium is reached. Although the total charge on either side of the interface is equal, the spatial extent of the dipole region depends on the charge carrier concentration, which is much higher in metals than semiconductors. Thus, on the metal side of a metal-semiconductor interface, the charge is highly localized at the interface, but in the semiconductor this dipole region can extend a significant distance. Certain combinations of semiconductor doping and metal work function can result in a barrier to conduction, called a *Schottky barrier*, because the dipole depletes the semiconductor of the dominant charge carriers. If the metal work function is higher than that of the semiconductor ($\chi_S > \chi_M$), the dipole created points towards the metal (i.e. the semiconductor is positively charged) and depletes the semiconductor surface of negative charge carriers, blocking conduction for an electron-doped semiconductor (Figure 3.1). The depth of carrier depletion into the semiconductor surface is referred to as the *depletion width* or *depletion length.*

The case of a low work function metal and a *p*-type semiconductor is symmetric and the Schottky barrier impedes hole transport (Figure 3.2). This is the

situation in my devices, where I used Chromium (χ_M = 4.5eV) and ambient-doped p-type CNTs [71] (χ_S = 4.8eV) [72-74]. Both *n*-type and *p*-type barriers are referred to as *Schottky Barriers* or *Schottky Junctions*. In the remaining two cases (high-work function metal with p-type semiconductor and low-work function metal with an n-type semiconductor), no barrier ought to form. I used Platinum (χ_M = 5.6 eV) as a high work function contact to *p*-type CNTs to avoid barrier formation on the second contact, thus creating a rectifying device with asymmetric contacts, termed a Schottky diode.

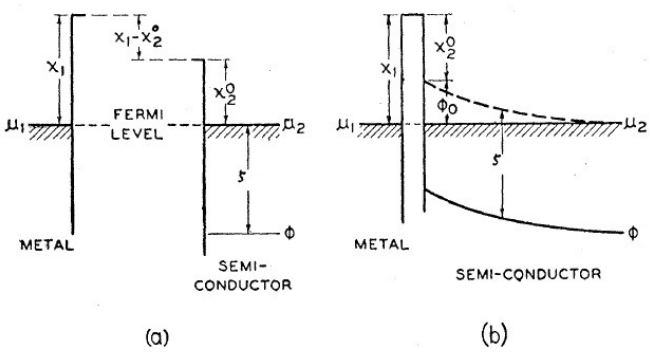

Figure 3.1. Band diagram of Schottky barrier formation at metal and *n*-type semiconductor interface, a) before the materials are brought into contact and b) after contact. χ_1 is the metal work function, χ^0_2 is the semiconductor work function, $\mu_1 = \mu_2$ is the Fermi level, ζ is the semiconductor band gap and ϕ is the valence band of the semiconductor. Adapted from Bardeen[70].

Quantitatively, the height of the Schottky Barrier ϕ_{b0} in the simple model ought to be simply the difference in work functions,

$$\phi_{b0} = \chi_m - \chi_s \qquad \text{(Eq. 3.1)}$$

where χ_m and χ_s are the metal and semiconductor work functions respectively (shown as $\phi_0 = \chi_1 - \chi_2$ in Figure 3.1). Experimentally this is not observed in bulk metal-semiconductor junctions[70] and the explanation for the observed Schottky barrier heights have been a subject of research late into the 20th century.[75-77] The discrepancy today is largely attributed to metal interface gap states (MIGS). These MIGS can be considered surface states in the semiconductor, dangling bonds or the extension of metal wavefunctions into the semiconductor side of the interface. They contain charge in an otherwise charge-depleted region of the semiconductor, effectively lowering the barrier height. However, in CNT devices, the one-dimensional nature of CNTs eliminates the concentration of MIGS at the interface, restoring the simple picture of Schottky barriers.[78]

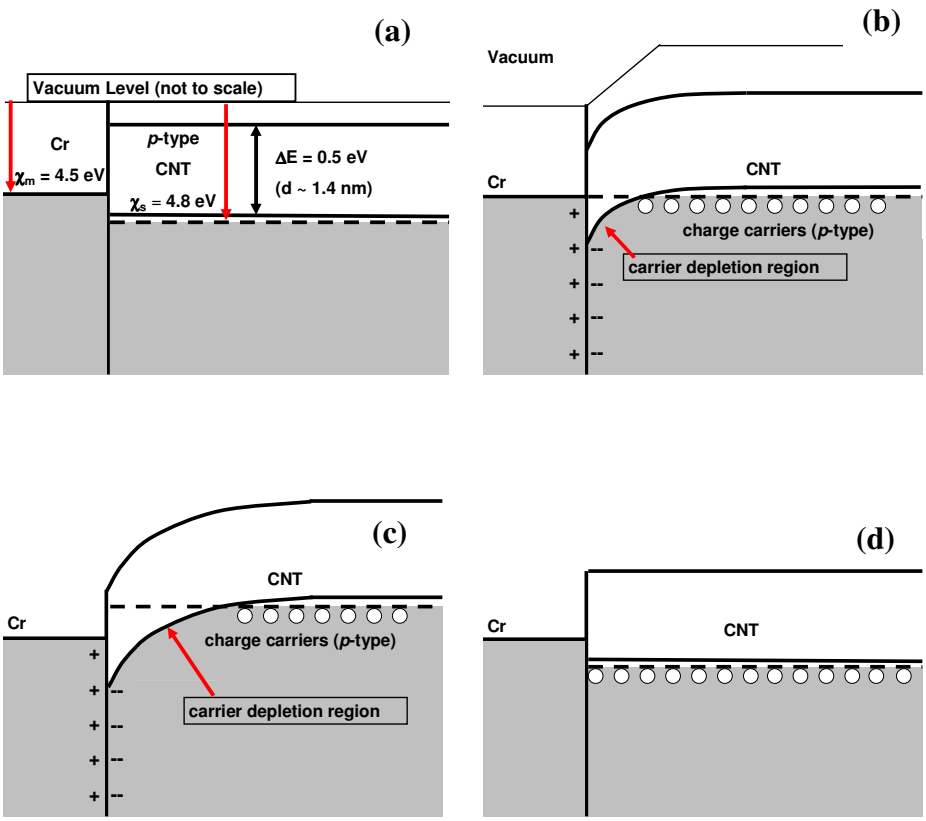

Figure 3.2. Band diagrams of a *p*-type Schottky junction a) before barrier formation, b) after formation, c), under reverse bias and d) forward bias.

The behavior of a Schottky barrier is asymmetrical with respect to applied bias. When the applied bias raises the Fermi level of a *p*-type nanotube, the depletion length and barrier height at the Cr interface grow, blocking electrical transport (Figure 3.2 c). This is termed reverse-bias. In the opposite case, forward bias, the CNT Fermi level is raised and the depletion region shrinks, enabling electrical

transport (Figure 3.2 d). This asymmetric behavior leads to rectification of AC signals.

Most metal contacts to CNTs, particularly low-work function Cr and Ti contacts, result in Schottky barriers[79-81]. The capacitance across these Schottky junctions, C_J, that is the capacitance between the channel and the metal contact, contributes to the time constant $\tau = 2\pi RC$ for CNT devices and thus their inherent maximum operating frequency.

3.3 Current Transport Across Schottky Barriers

The current flow through such Schottky junction is most often modeled by the empirical Shockley equation (Eq 3.2).

$$I = I_S(e^{qV_D/nkT} - 1) \qquad \text{(Eq 3.2)}$$

where I is the current, I_S is the reverse saturation current, q the charge carrier charge (assumed to be 1.609×10^{-19} C), V_D the source-drain voltage, n a unitless ideality factor, k Boltzmann's constant and T the temperature. The ideality factor n is nominally 1.0. For bulk junctions the parameter is usually under $n = 2.0$. However, there are processes which result in values of n much larger than 1, which I will discuss later. Calculated currents for theoretical diodes with idealities of $n = 1$, 1.5, 2, 5 and 10 are shown in Figure 3.3.

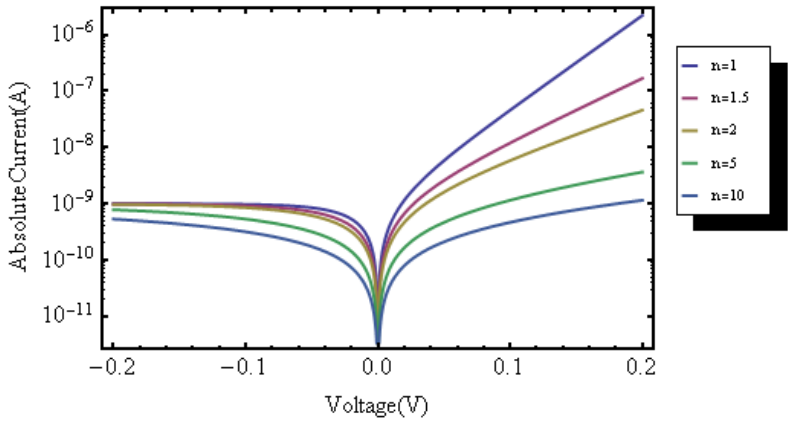

Figure 3.3. Calculated current-voltage characteristics for diodes with I_S=1nA and *n* values of 1,1.5,2,5 and 10 at room temperature (T = 300 K).

There are several theoretical models which can be used to explain the conduction mechanism across a Schottky junction, as described by Sze [82]. These include thermionic emission, diffusion, tunneling and combinations of those three. In broad terms, the thermionic emission expression is the result of calculating the number of states likely to possess energy E greater than the barrier height. This is done by convolving the density of states $D(E)$ in the semiconductor (the three-dimensional DOS, in Sze's derivation) and the Fermi distribution $F(E)$ for a given temperature, then integrating to find the number of states above the Schottky barrier eight, given barrier height ϕ_b and applied bias V_D. The result is shown below, and has the form of the empirical diode equation 3.2. The term (-1) comes from subtracting the metal-to-semiconductor current (from V=0) to obtain the net semiconductor-to-metal current:

$$J_{S\to M} = A^{*}T^{2}e^{\left(-\frac{q\phi_B}{kT}\right)}\left[\ e^{\left(\frac{qV}{kT}\right)} - 1\ \right] \qquad \text{(Eq 3.3)}$$

The diffusion approach also leads to an expression of the form 3.2 and 3.3, albeit with a different temperature dependence in the pre-factor. The third mechanism discussed by Sze is tunneling of charge carriers across the depletion region. However, no analytical solution is given. The effect of tunneling current is to raise the saturation current I_S and introduce the ideality factor n present in 3.2; effectively making the current less sensitive to voltage. In thin film diodes, the ideality factor n is near 1.0. However, as explained by Mohammed[83] the ideality factor for 1D rectifying contacts can approach values of 20. This is confirmed experimentally in Si nanowire and GaAs nanowire contacts.

3.4 Applied Voltage vs. Junction Voltage

Real devices have a finite resistance which limits the forward-bias current from being truly exponential at high forward bias as predicted by equation 3.2. Figure 3.4a shows an IV relationship I measured using a commercially available GaAs Schottky diode manufactured by Aeroflex. The linear fit shown corresponds to a 1.8 kΩ series resistance. Under reverse bias or low bias, the Schottky junction resistance limits current flow across the device, that is to say $R_J(V) >> R_S$, such that the bias

applied to the diode drops at the junction and the voltage drop at the R_S can be neglected. However, under increasing forward bias, $R_J(V) \sim R_S$, the voltage drop at R_S becomes an increasingly significant fraction of the applied bias until it dominates as $R_J(V)$ approaches zero at high bias. To calculate the junction voltage V_J as conceived in the Shockley equation, the voltage drop across R_S must be subtracted from the applied bias. Thus the junction voltage is

$$V_J = V - IR_S \qquad \text{(Eq. 3.4)}$$

where R_S is the series resistance as calculated from the constant current-voltage relationship at high forward bias. The effect of this correction is shown in Figure 3.4b. Although the applied bias is as high as 0.6 V, the figure of interest, the bias at the Schottky junction, never exceeds 0.47 V.

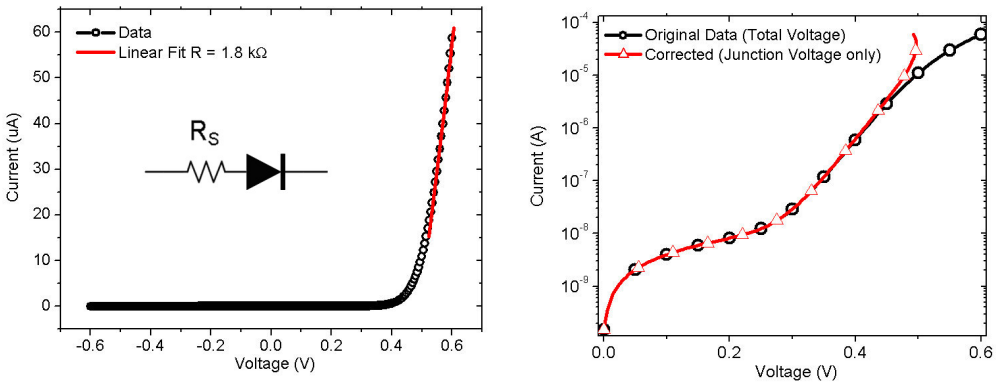

Figure 3.4**.** a) Measured current-voltage characteristic for a commercial GaAs Schottky diode obtained from Aeroflex. Data (black circles) are fitted to a line (red) corresponding to 1.8 kΩ resistance at high bias. Inset: simplified circuit model. b)

Log plot (black circles) of the device IV curve, plus a the corrected Schottky junction IV curve (red triangles) omitting the voltage drop in the device's series resistance.

3.5 Circuit Analysis

Figure 3.5 is a circuit model describing a diode where R_S is a constant series resistance, C_P is a constant parasitic source-drain capacitance, $R_J(V)$ is a non-linear resistance and C_J is the unknown drain-channel capacitance, the nature of which will be discussed shortly, and which determines the intrinsic RC time constant for high-frequency CNT devices.

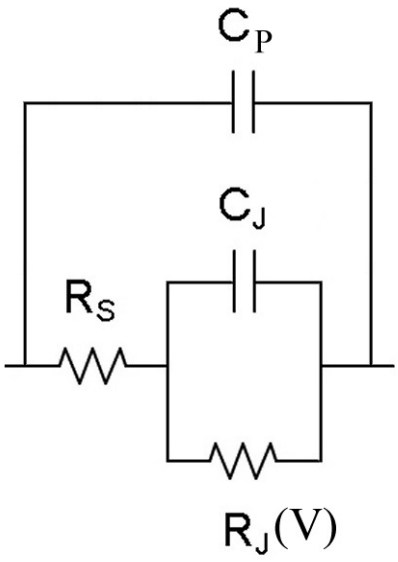

Figure 3.5 An overall circuit model of a Schottky diode, adapted from Sorensen.[84]

At dc, C_J and C_P can be neglected, leaving only the resistive circuit branch. Although a large ac current can flow through element C_P, this current neither

produces a dc current nor diminishes the amplitude of the voltage applied to the non-linear branch of the circuit. Thus, the parasitic capacitance C_P can be ignored in the analysis of the frequency dependence of the device and we can use the rectified current signal $I_{DC}(f)$ as a probe of device physics in the 1D channel.

3.6 Junction Capacitance Calculations and Experiments

The junction capacitance C_J of CNT rectifiers is important in determining their intrinsic maximum operating frequency. Measuring this value directly is challenging due to the much larger parasitic capacitance C_P which lies in parallel with it. Postma et al[68] posits a value of 0.3aF in a CNT single-electron transistor. Jarrillo-Herrero extracted a value of 1-3 aF[85] for source and drain capacitances on Chromium-Gold contacted CNTs. Tarkiainen[29] extracts values from 31aF to 111aF for tunnel junctions from metallic leads to metallic nanotubes. Yoneya[86] estimates 1aF.

The most detailed study of carbon nanotube Schottky junction capacitance to date was performed recently by Tseng and Bokor[13]. This group fabricated CNT-SD devices using dissimilar metal contacts on an oxidize silicon wafer with a back gate electrode. Using a very sensitive capacitance bridge, they used the back gate to turn the nanotube channel off and measure the parasitic capacitance between the leads, including source-gate and drain-gate capacitances, which they subtracted from the total on-state capacitance. Chromium, Titanium and Niobium were used as contact metals and the resulting values ranged from 5 aF to 27 aF. The tiny size of this

capacitance, if coupled with achievable device resistances of the order of 100kΩ, imply intrinsic cut-off frequencies near the THz range.

3.7 Previous High-Frequency CNT Transport Measurements

Since the discovery of extraordinarily high charge carrier mobility of $10^5 cm^2/Vs$ in CNTs by Durkop[87], there has been considerable interest in the microwave transport properties of CNTs for use in electronic devices and interconnects. However, the high impedance discussed in chapter 2 makes straightforward measurements difficult. Most of the work done to date has been on devices which are suspended over a ground plane, introducing significant source-gate and drain-gate capacitances that limit device performance. Others have required complex de-embedding techniques to extract the CNT device signal from a very large background. Table 3.1 summarizes the results in many notable CNT transport experiments as well as some key aspects of each work. Of these, Pesetski et al[88] fabricated top-gated CNT field effect transistors (FETs) on quartz substrates and measured current gain up to a frequency of 23 GHz by looking at intermodulation products. The work described in this dissertation enables study of transport measurements well beyond that limit, as demonstrated in chapter 6.

Author (et al)	Year	Tubes	L_{gate} (nm)	FET Geometry	f_{ce} *(extrinsic)*	f_{ci} *(intrinsic)*	Method
Li [90]	2004	1	100	Ground Plane	2.6 GHz	n/a	LC- resonance at 2.6GHz only
Frank [91]	2004	1	300	Ground Plane	n/a	> 0.3 GHz	Signal Mixer, dc output
Appenzeller [92]	2004	1	300	CNT over Ground Plane	n/a	0.6 GHz	Signal Mixer, dc output
Rosenblatt [93]	2005	1	2000	Ground Plane	6 GHz	50 GHz	Signal Mixer, 5nA dc output
Bethoux [89]	2006	~100	300	CNT mat over Ground Plane	2 GHz	8 GHz	Current Gain
Pesetski [88]	2006	n/a	1000	Top Gate on Quartz	>23 GHz	>23 GHz	Signal Mixer 10kHz Modulation
Yu[103]	2006	1	1000	Ground Plane	>1 GHz	n/a	VNA
Le Louarn	2007	100's	300	Ground Plane	11 GHz	30 GHz	Current gain, extrapolated
Plombon [94]	2007	1	2000	Ground Plane	n/a	>20 GHz	VNA, de-embedding
Gomez-Rojas [95]	2007	1-5	100	Quartz	0.1 GHz	n/a	VNA
Kocabas[100]	2008	1000's	750	Top Gate on Quartz	2.5 GHz	15 GHz	VNA, 0dB Current gain
Kocabas[101]	2009	100's	700	Top Gate on Quartz	9 GHz	30 GHz	VNA, 0dB Power gain
Nougaret[102]	2009	100's	300	Top Gate on Quartz	3 GHz	80 GHz	VNA, purified sc tubes in solution

Table 3.1 Summary of selected high-frequency CNT field-effect transistor (FET) transport experiments and relevant device parameters: number of nanotubes per device, gate length, device geometry, observed (extrinsic) device cut-off frequency f_{ce}, calculated (intrinsic) cut-off frequency f_{ci} and measurement technique used.

Chapter 4

Microwave Rectification by a Carbon Nanotube Schottky Diode

"Every honest researcher I know admits he's just a professional amateur. He's doing whatever he's doing for the first time. That makes him an amateur. He has sense enough to know that he's going to have a lot of trouble, so that makes him a professional." – Charles Kettering

4.1 Introduction

This chapter describes my fabrication of carbon nanotube Schottky diodes using in an all-photolithographic process using dissimilar contact metals on sapphire substrates. The dc electrical characteristics of the diodes show near-ideal behavior. I measure the rectification properties of these diodes at microwave frequencies using a horn antenna to irradiate the diodes. The diodes are shown to rectify currents of up to 100 nA and at frequencies up to 18 GHz. An independent measure of the frequency dependence was hampered by device design and equipment limitations. These shortcomings were addressed in the new experiment described in chapters 5 and 6. Nevertheless, the data obtained in this preliminary experiment was used to estimate a Schottky junction capacitance of ~10^{-18} F and the intrinsic device cut-off frequency of

~400 GHz. Most of the work described in this section was published in: Enrique Cobas and Michael S. Fuhrer, "Microwave rectification by a carbon nanotube Schottky diode," *Applied Physics Letters 93*, 043120, 2008. [105]

4.2 Diode Fabrication

RF-compatible CNT-SD devices were prepared on sapphire and quartz substrates through in the following manner. An array of alumina-supported $Mo_2(acac)_2$ and $Fe(NO_3)_3$ catalyst islands was pre-patterned on sapphire and quartz substrates using a polymethylmethacrylate (PMMA) – photoresist double layer photolithography[18]. Carbon nanotubes (work function 4.7-5.1eV) [19-21] were grown via chemical vapor deposition (CVD) at 900C in a tube furnace using methane, hydrogen and ethylene[22]. Contacts and leads for a 360-device array were created in close proximity to the catalyst islands by two steps of standard photolithography. Low-ohmic contacts were deposited via electron-beam evaporation of 200 Å of platinum (work function 5.6eV), followed by 2,000Å of gold and capped with 200 Å of platinum for surface hardness. Schottky contacts were deposited to either side of the central ohmic contacts via thermal evaporation of 50Å of chromium (work function 4.5eV) and 2,000 Å of gold. Thus two devices (referred to as Device 1 and Device 2) were fabricated for each electrode set. Figure 4.1 shows a completed set of electrodes within the array. The majority of the electrodes included no nanotubes or included metallic nanotubes which obscure the transport properties of the semiconducting nanotubes (e.g. Device 1 in Figure 4.2, which exhibits metallic behavior with

R~50kΩ). However some of the devices included single semiconducting nanotubes (e.g. Device 2 in Figure 4.2).

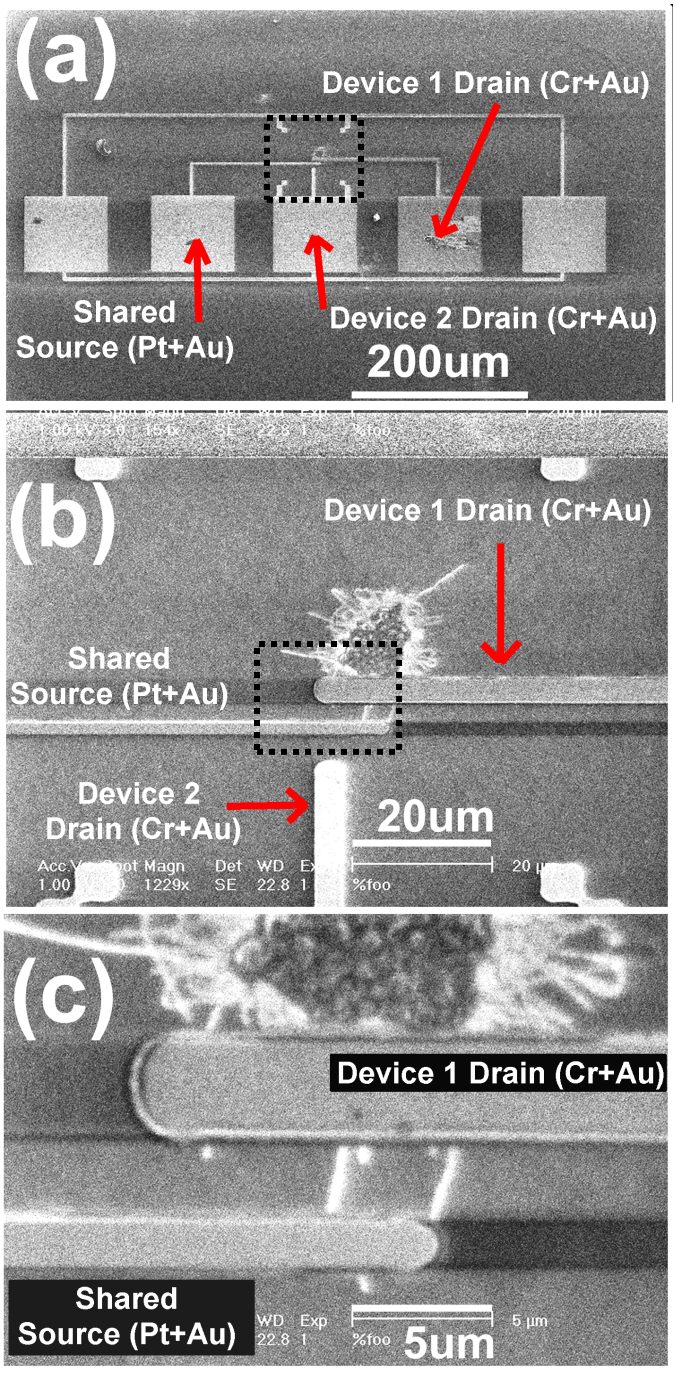

Figure 4.1. Scanning Electron Microscope (SEM) micrographs of an electrode set fabricated for this work. (a) Overview showing the ground-signal-ground contact

arrangement within a grounded shielding loop, (b) Close-up of the device area showing the catalyst island just above the source and drain leads for Device #1 and (c) Close-up of the 6um channel showing two nanotubes bridging Schottky source #1 (top) and the common Ohmic drain (bottom). No nanotubes are evident in contact with source #2, so device #2 in this electrode set is open. This electrode set was not used for electrical measurements.

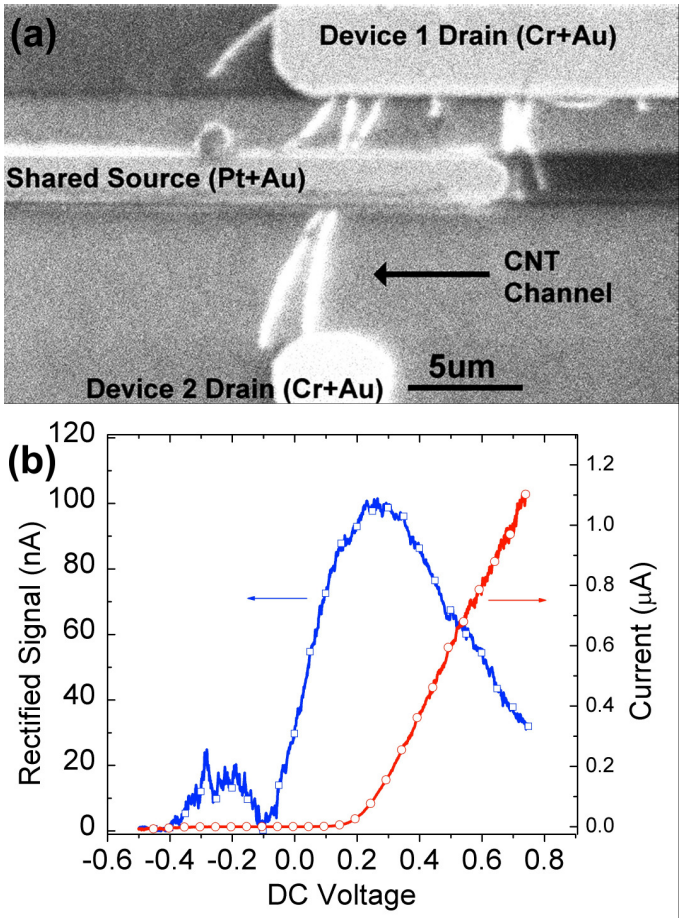

Figure 4.2. (a) Scanning Electron Microscope (SEM) image of the electrode set used for the electrical measurements discussed and (b) the current-voltage characteristics (red circles) and rectified current signal (blue squares) from Device 2 shown, due to a 7GHz microwave signal at +9dBm.

4.3 Measurement Setup

All electrical measurements were carried out in a Cascade Microtech Summit 1200 automated probe station using Keithley 2400 Sourcemeters under ambient conditions. A simple LabView application was created to automate dc characterization of all devices in the array, as described in further detail in Chapter 5. RF measurements were performed using a Hewlett Packard 83620B microwave signal generator, an X-Band horn antenna, an Ithaco 1211 current amplifier and a Stanford Research Systems SR 380 lock-in amplifier. The probe station's dc electrical probes doubled as receiver antennae, directing the microwave signal broadcast from the nearby horn antenna into the nanotube device. The microwave signal was amplitude modulated at 1 kHz to enable measurement of the rectified current signal with the lock-in amplifier as a function of microwave frequency, microwave power and dc bias. A photo of the measurement setup is shown in Figure 4.3.

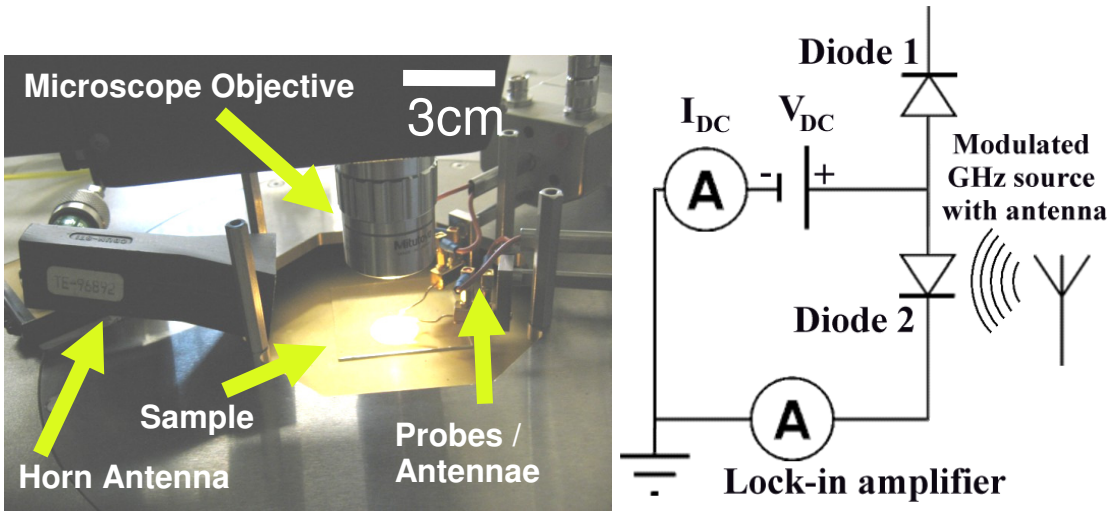

Figure 4.3. Photo (left) and circuit diagram (right) of the preliminary measurement setup and circuit. An X-band horn antenna driven by a modulated microwave source

provides the ac excitation while a lock-in amplifier measures the generated ac current. The dc probes function as receiving antennae to couple the microwave radiation into the circuit. Offset dc voltage and a measurement of dc current, are provided by a Keithley 2400 SourceMeter and Ithaco 1211 current pre-amplifier, respectively.

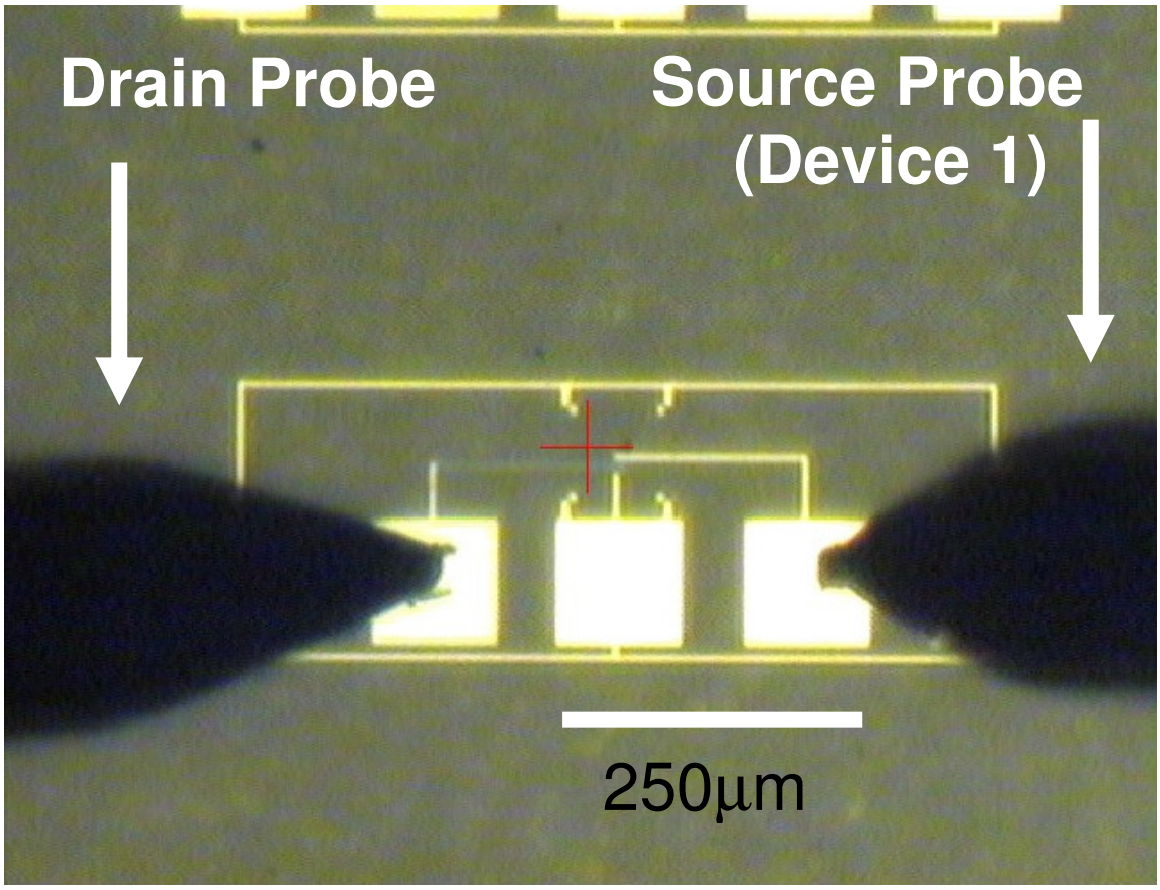

Figure 4.4 Optical image of an electrode set and source/drain probes during microwave measurement. The microwave horn antenna was positioned orthogonal to the probes axis (top, not shown) with the polarization oriented in-plane with the probes. Another electrode set can be seen at the top edge of the image.

4.3 DC Results

Figure 4.5 shows the dc current-voltage (*I-V*) curve for an individual CNT-SD. At low frequency, we model the CNT-SD as a diode in series with a resistor:

$$I = I_s \left[e^{(qV - IR_s)/nkT} - 1 \right], \qquad \text{(Eq 4.1)}$$

where I_s is the reverse saturation current, R_s is the series resistance, n is the ideality factor, k is Boltzmann's constant, q is the electronic charge, and T is the temperature. A fit to this equation (0mV to 400mV) gives n = 1.00 and a series resistance R_s = 420 kΩ.

The diode resistance and series resistance are approximately equal at $V_{dc} \approx$ 200mV, where a knee in the *I-V* curve is evident.

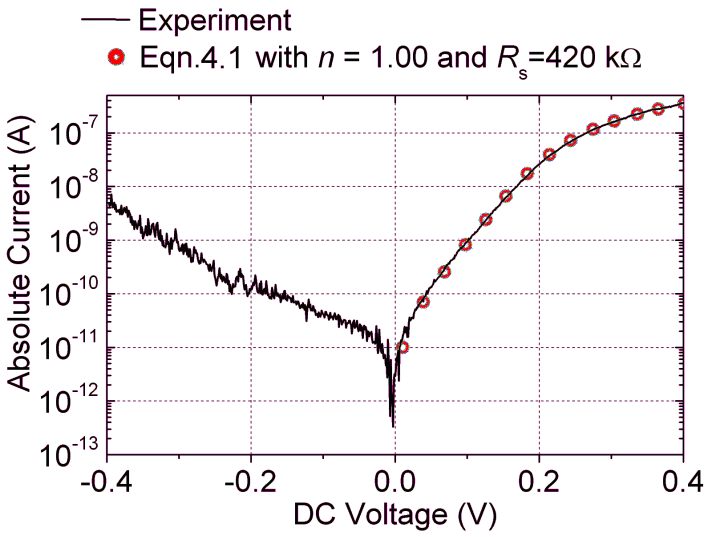

Figure 4.5. DC current-voltage characteristics of a CNT Schottky diode (black line) and corresponding fit to Eqn. 1 (red circles) with $n = 1.00$ and $R_s = 420\text{k}\Omega$. The data shown is from Device 2 pictured in Figure 4.2.

4.4 Microwave Rectification Results.

In general we found that the response of the device embedded in the measurement setup was strongly dependent on frequency, with the response as a function of frequency showing numerous peaks and valleys. We attribute this to strong dependence of the antenna efficiency on frequency resulting from resonances in our non-ideal setup (the measurement apparatus is complex on the order of the wavelength). Thus using the applied microwave power is a poor indicator of the power reaching the device. Although the complex frequency dependence of our measurement setup makes a simple, direct frequency dependence measurement impossible, a comparison of the bias voltage dependence of the data at various frequencies within the square-law power regime does lead us to useful conclusions. Figure 4.6 shows a comparison of rectified current ΔI at frequencies $f = 7$ GHz (red) and $f = 18$ GHz (blue) at various source powers P within the square-law regime.

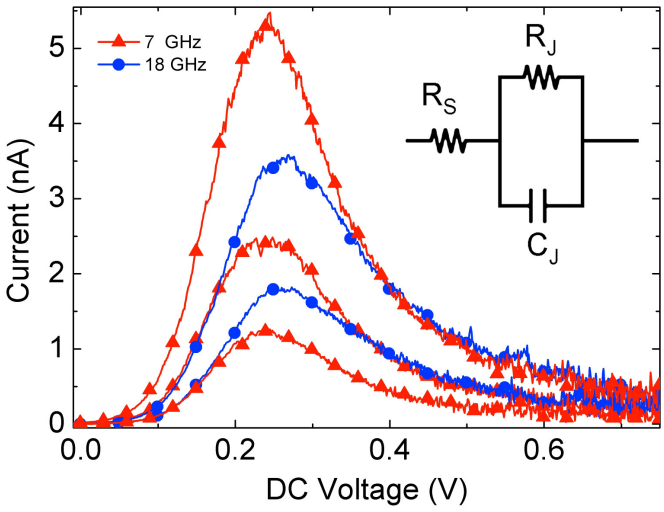

Figure 4.6. Rectified output signal from a CNT-SD as a function of dc bias under various powers of 7GHz (red squares) and 18GHz (blue triangles) microwave excitation. The corresponding microwave intensities are (top to bottom) -14dBm, -17dBm and -20dBm for the 7GHz data and -8dBm and -11dBm for the 18GHz data. Inset shows the model equivalent circuit, ignoring the stray capacitance which is bias-independent.

A systematic difference in the shape of the ΔI-V curve with frequency is evident. This may be understood qualitatively as follows. Consider the two curves corresponding to f = 7 GHz, P = -14 dBm and f = 18 GHz P = -8 dBm. At high V, when the diode resistance is low, these two curves produce similar response, indicating that the cutoff frequency is much larger than 18 GHz. As V is decreased, the diode resistance increases, and the cutoff frequency decreases below 18 GHz so the response becomes frequency-dependent, smaller at higher f. We explore this quantitatively below.

We express the power reaching the Schottky junction as

$$P_j = PE_{ant}E_{dev} \qquad \text{(Eq 4.2)}$$

where P is the emitted power, E_{ant} is the fraction of the emitted power absorbed by the device and E_{dev} is the fraction of power in the device dissipated at the Schottky junction. Then the additional current due to the power absorbed in the junction can be expressed as

$$\Delta I = \beta P_j \qquad \text{(Eq 4.3)}$$

where the responsivity β is determined solely by the variable junction resistance $R_{\text{j}}(\text{V})$.

Then, following Sorensen et al,[23] we model the device as R_{j} in parallel with a constant junction capacitance C_{j} and a constant series resistance R_{s}, as in Figure 4.6 (inset). This leads to expressions for the predicted cut-off frequency f_{c} in the square-law regime and the frequency-dependent device efficiency $E_{\text{dev}}(f)$:

$$f_c = \frac{[1 + R_s / R_j]^{\frac{1}{2}}}{2\pi C_j (R_s R_j)^{\frac{1}{2}}} \qquad \text{(Eq 4.4)}$$

$$E_{dev}(f) = \frac{P_j}{P_{dev}} = \frac{1}{[1+\frac{R_s}{R_j}][1+(f/f_c)^2]}. \qquad \text{(Eq 4.5)}$$

then from Eqn. 4.3 the ratio of the currents at two different frequencies is $\Delta I(f_1)/\Delta I(f_2)$ = $[E_{dev}(f_1)/E_{dev}(f_2)]x[E_{dev}(f_1)/E_{dev}(f_2)]$ = const. x $[E_{dev}(f_1)/E_{dev}(f_2)]$. The signal strength was verified to be proportional to the microwave power, indicating the device was operating in the square-law regime. The ratio of the device efficiencies at frequencies f_1 and f_2 approaches the values $E_{dev}(f_1)/E_{dev}(f_2)$ = 1.00 for (f_1,f_2 << f_c) and $E_{dev}(f_1)/E_{dev}(f_2) = (f_2/f_1)^2$ (which is a factor of 6.61 for the two frequencies used here) for (f_1,f_2 >> f_c). Since R_j and hence f_c are strong functions of bias voltage, in general there will be a transition from f_1,f_2 >> f_c to f_1,f_2 << f_c, and the ratio $\Delta I(f_1)/\Delta I(f_2)$ will be bias-voltage dependent.

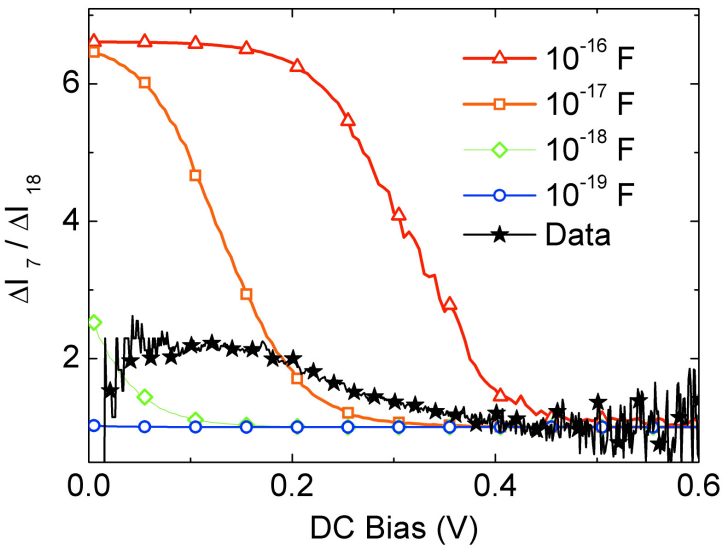

Figure 4.7. Rectified current ratio at 7GHz vs.18GHz as a function of dc bias. Solid lines are calculated from the measured junction resistance data $R_j(V)$ and the model

equivalent circuit in figure 3 for junction capacitances Cj = 10^{-19} F (blue circles), 10^{-18} F (green rhombi), 10^{-17} F (orange squares), 10^{-16} F (red triangles). The experimentally observed ratio (scaled to 1.0 at high bias) is shown as black stars.

Figure 4.7 shows a comparison of the efficiency ratio for various trial junction capacitances C_J and the ratio of the experimentally measured 7 GHz and 18 GHz signals, ΔI(7 GHz)/ΔI(18 GHz), which, as anticipated above, is voltage dependent. The experimental ratio varies more gradually with voltage than the theoretical curves. This is possibly due to R_s and C_j being distributed elements along the length of the CNT; as R_j becomes small (large V) and the resistance is dominated by the series resistance of the CNT, the capacitive coupling of portions of the CNT more distant from the junction becomes relatively more important, and the effective C_j increases. However, comparing the large V and small V limits we can conclude that the junction capacitance of the device is in the 10^{-18} F range, in accordance with previous estimates[89-916]. This value allows us to estimate the intrinsic nanotube diode cut-off frequency

$$f_c = \frac{1}{2\pi RC_j} = \frac{1}{2\pi(420\,\mathrm{k\Omega})(10^{-18}\ \mathrm{F})} \approx 400\ \mathrm{GHz}. \qquad \text{(Eq. 4.6)}$$

4.5 Conclusion

In this preliminary experiment, we demonstrated fabrication of carbon nanotube Schottky diodes via straightforward CNT synthesis and lithography

techniques on Sapphire substrates. The devices produced exhibit excellent Schottky diode characteristics in series with a high channel resistance and exhibit good rectification performance. This work demonstrated the feasibility of using Schottky diodes as probes of microwave frequency transport properties of carbon nanotubes and similar nanostructures. The intrinsic cut-off frequency set by the junction capacitance and series resistance of CNT-SDs is on order 400 GHz and could be pushed into the THz if the series resistance could be lowered, e.g. through shortening or doping the CNT. The shortcomings of this preliminary work (low device yield, unoptimized device geometry, resonance-less measurement setup and measurement of the power reaching the diode) are addressed in an improved version of this experiment, described in chapters 5 and 6.

Chapter 5

Fabrication of Coplanar Waveguide Carbon Nanotube Schottky Diodes

"*One must imagine Sisyphus happy.*" – Albert Camus

5.1 Carbon Nanotube Schottky Diodes Integrated in Co-planar Waveguides

The preliminary results discussed in Chapter 4 demonstrated our ability to fabricate carbon nanotube Schottky diodes on insulating substrates, and measure their rectification properties at dc and at high frequencies. In this chapter, I discuss the fabrication of carbon nanotube Schottky diodes integrated into a co-planar waveguide (CPW) electrode geometry which allowed me to measure their rectification properties across a broad frequency range from 10 MHz to 40 GHz using standard microwave test equipment coupled via ground-signal-ground probes. In addition to changing to the CPW geometry, I made several other important imrovements; specifically, I made changes to the nanotube catalyst, the substrate material and heat treatment, and the CVD synthesis process. Chapter 6 discusses the results of the microwave rectification measurements on these second-generation devices, along with analysis of the data and conclusions.

5.2 Synthesis of Horizontally Aligned Carbon Nanotubes on Quartz Substrates

Sample and device yield was improved dramatically by switching to a ferritin catalyst-based CVD process on ST-cut quartz substrates largely following the recipe of Kocabas et al[92]. In brief, high-temperature (900 ºC) annealing of single-crystal quartz wafers cut along the (01 $\overline{1}$ 1 1) direction, known as an ST-cut, results in improved surface crystallinity which preferentially aligns carbon nanotubes along the (100) direction during CVD[92-97]. A detailed study of the phenomenon and technique was more recently done by Rutkowska et al[96], concluding that annealing for 1-hour to 8-hours at temperatures between 875 and 950C results in the highest degree of CNT alignment.

In my experiment, quartz substrates (4" round, ST-cut, single-side polish, 500um thickness) were purchased from Hoffman Materials and diced into 14mm squares by John Abrahams at the Maryland FabLab. This was done to accommodate the 0.9" inner-diameter CVD tube furnace and the 14.5mm square wire bond chip carriers previously purchased from Glasseal. Due to the hardness of the quartz and mediocre adhesion to the backing material during wafer sawing, the best procedure was found to be grooving the wafer about 400μm deep and snapping the pieces off manually. The polished side was coated in photoresist prior to sawing to avoid surface contamination and the pieces were rinsed in acetone, methanol and isopropanol after sawing. Quartz substrates were annealed in air for 18 hours at 900 ºC in a Lindberg-Blue HTF55347C three-zone tube furnace controlled by Omega CN4431 temperature controllers. A small fraction of the substrates were observed to fracture during the annealing process. A two-hour temperature ramp was introduced

during warm-up and cool-down to allow more time for stress-relief, especially near the 600 ºC β–quartz phase transition.

Although annealed quartz substrates were imaged with AFM prior to further processing, no distinguishing surface features (e.g. grooves, step-edges) were evident, in agreement with Rutkowska et al's conclusion that quartz surface bond orientations, and not atomic step edges, cause CNT alignment on quartz.[96] It may be possible that microstructural features are only evident at high temperature in the β-quartz phase which occurs during annealing and CNT growth and are thus difficult to image at room temperature.

Iron nanoparticles derived from ferritin served as nanotube synthesis catalyst[98]. Ferritin is a relatively large, spherical organic molecule commonly found in the tissues of many mammals, including humans, and serves to store iron which it does in the form of a nanoparticle at its core.[99] The horse-derived aqueous ferritin solution used here was purchased from Atomate Inc. The as-received ferritin solution (kept refrigerated at 5 ºC for several months) was diluted to a concentration of 500 μg/mL using deionized water only (diluting the NaCl concentration). The annealed substrates were placed into this catalyst solution and left overnight at 5 ºC, then rinsed with DI water prior to nanotube growth.

The substrates were placed in a Lindberg-Blue HTF55122A (rated to 1200º C) tube furnace with a 1" OD / 0.9" ID diameter GE 214 quartz tube. The temperature was controlled by custom controllers with integrated Omega CN4431 temperature controllers. The flow rate was controlled manually using Omega FL-3805ST (argon, methane) FL-3802ST (hydrogen, ethylene) rotameters, with flow rates calibrated to account for the different density of each gas, at ambient pressure. The standard procedure for furnace use includes flushing the furnace with ~12 L argon to remove ambient oxygen and flushing the hoses with their respective gases (~4–5 L) to remove oxygen that may have permeated into the Tygon hoses over time prior to heating the furnace. The temperature ramp-up was programmed for consistency and repeatability, as follows:

- Ramp to 700 ºC in 10 minutes and hold temperature for 10 minutes.
- Ramp to 800 ºC in 5 minutes and hold temperature for 5 minutes.
- Ramp to 875 ºC in 5 minutes and hold temperature for 5 minutes.
- Ramp to 900 ºC in 5 minutes.

Samples X28 and X29 were exposed to ambient air (the tube connectors removed) and left to calcine in air at 900 ºC for 10 minutes to burn the organic parts of the ferritin catalyst particles. The furnace tube was then closed again and flushed with 12.9L of argon at 4300 sccm. The nanotube growth step consisted of a methane and hydrogen co-flow at 500 sccm each for 30 minutes at 900 ºC. After nanotube growth, the methane and hydrogen were replaced with 3400 sccm of argon and the furnace

was allowed to cool to 560 ºC. The argon flow was reduced to 250 sccm until the furnace cooled to 200 ºC and the samples could be removed.

For sample X36, the furnace was heated in ambient air (after flushing the hoses) with the sample inside. The sample was allowed to calcine in air for an extra 10 minutes at 900 ºC prior to closing the tube and flushing with 9 L of argon at a flow rate of 3,000 sccm. The nanotube growth step consisted of a co-flow of methane and hydrogen at 500 sccm each for 26 minutes at 900 ºC. The furnace was allowed to cool to room temperature under argon flow.

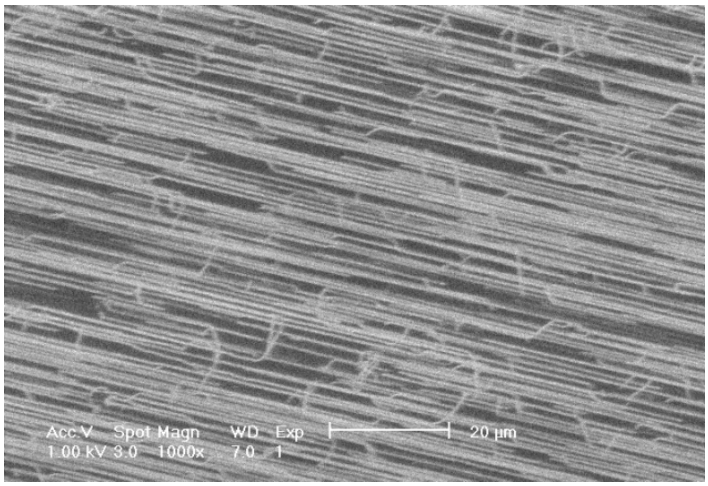

Figure 5.1. SEM micrograph of a horizontally aligned CNT film produced for this experiment at U. Maryland. The scale bar is 20µm, indicating a tube density of approximately 1 μm^{-1}.

The samples were imaged in SEM (Phillips XL-30) and AFM (Vecco Dimension 5000) to determine the average nanotube diameter, the density of nanotubes on the

surface and the degree of their alignment. The distribution of nanotube diameters (for ferritin catalyst procedure) was found to be 1.75 nm with a standard deviation of 0.79 nm (n = 22), as shown in Figure 5.2. We assume that the majority of these carbon nanotubes are therefore single-walled nanotubes.

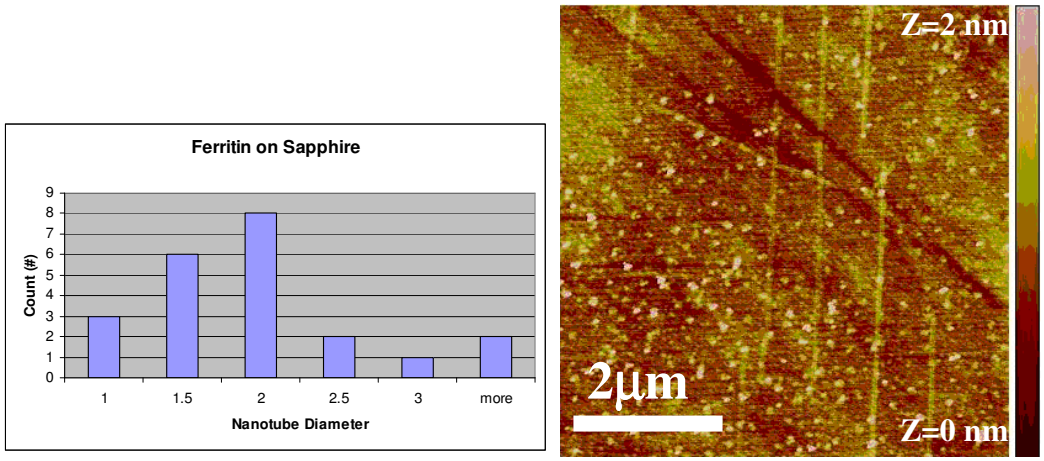

Figure 5.2. Left: Statistical distribution of CNT diameters resulting from a growth recipe using ferritin catalyst on an r-plane sapphire substrate, measured by AFM. Right: AFM image of aligned CNTs on quartz substrate, showing multiple tubes with diameters under 2 nm. All synthesis, imaging and measurements performed by myself, for this work, at University of Maryland.

5.3 Coplanar Waveguide Device Design and Fabrication

I used a coplanar waveguide (CPW) geometry which was originally designed by Dr. Alexander Manasson with guidance by Dr. Steven Anlage using IC Editor. The horizontal dimensions of the leads (lead thicknesses and gaps) are designed to match the pitch of standard microwave CPW probes and have a nominally 50Ω

impedance, minimizing any impedance mistmatch between the CPW probe and the leads. I altered the channel lengths and distribution of device types using Design CAD 2.0. The final version of the photomask can be seen in Figures 5.3 and 5.4. The Chrome-on-Soda Lime Quartz photomask was manufactured by Photo Sciences Inc (Product L625).

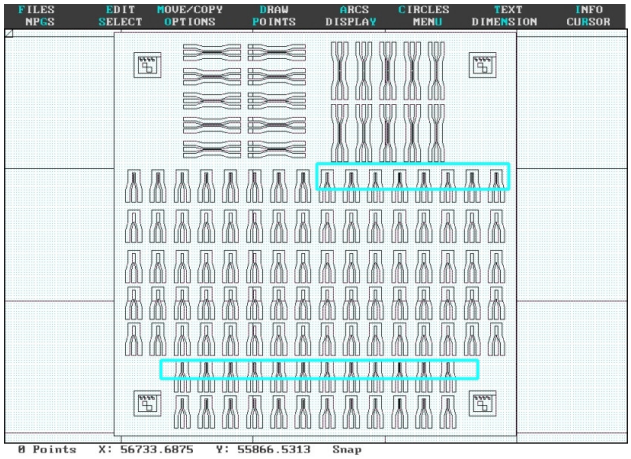

Figure 5.3. Design drawing of the CPW CNT-SD array including two-port diodes and transmission lines (top) and one-port devices (center and bottom). Highlighted devices (cyan outline) are the shortest channel lengths. The corner features are alignment markers. A thick transparent border (left and right edges) was created to aid mask alignment.

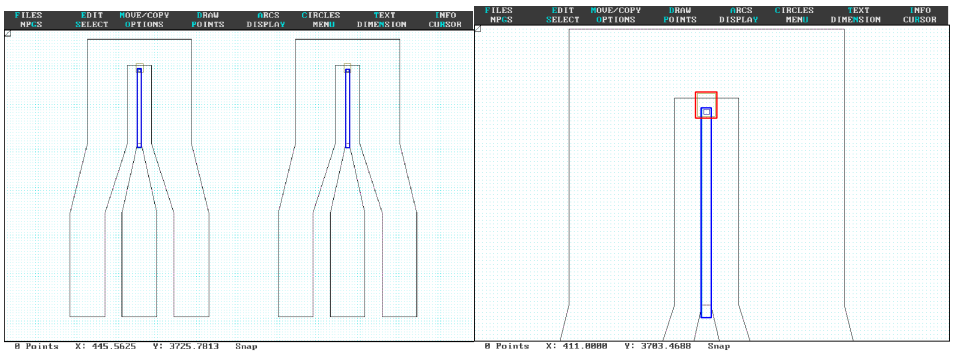

Figure 5.4. Left: Drawing of two one-port CNT-SD CPW devices. Contact pads are 100 µm wide, 150 µm in pitch (50 µm gap). The Schottky contact (black outline) is the inverse U-shaped contact comprising both outer pads. The Ohmic contact (blue) is the thinner center electrode. Right: Close-up view showing the active device area (highlighted by a red box) where nanotubes remain after patterned plasma etching.

Following nanotube growth, lead patterning was done with standard photolithography techniques, using a bilayer resist process to improve undercut and lift-off quality. The samples were baked for 5 minutes at 150 ºC to remove moisture. HMDS was spun onto the samples at 2,000 rpm for 45 seconds, followed by an undercut layer (Microchem LOR 3A) spun at 2,000 rpm for 45 seconds and baked at 150 ºC for 10 minutes. The photoresist (Shipley 1813) was spun onto the samples at 4,000rpm for 45 seconds and baked at 115 ºC for 60 seconds. UV Exposure was for 10 seconds at 12 mW/cm^2 using 405 nm light in a Karl-Suss MJB-3 contact mask aligner. The samples were developed in MF-CD-26 for approximately 40 seconds.

The original idea of using two lithography and metallization steps to alternately create the Schottky and ohmic metal contacts was made impractical by the poor adhesion of noble metals such as gold and platnium to the quartz surface. To promote adhesion of the high work function contact metal, an offset sticking layer of chromium (low work function) was necessary. The two lithography steps were therefore combined, and the asymmetric contacts were created using an angled evaporation procedure, described as follows. The chromium-gold Schottky contacts and sticking layer were fabricated via thermal evaporation. The chromium was deposited at an angle of 45 degrees to normal and the gold was deposited at 30 degrees to normal, ensuring that gold did not directly contact the nanotubes on the Schottky side of the device. The high-workfunction metal was then deposited using electron-beam evaporation normal to the sample surface and lift-off was done in Remover PG at 50 ºC. The resulting metal layer underlap profile was confirmed using AFM imaging and underlap length was measured to be approximately 400 nm, as seen in Figure 5.5.

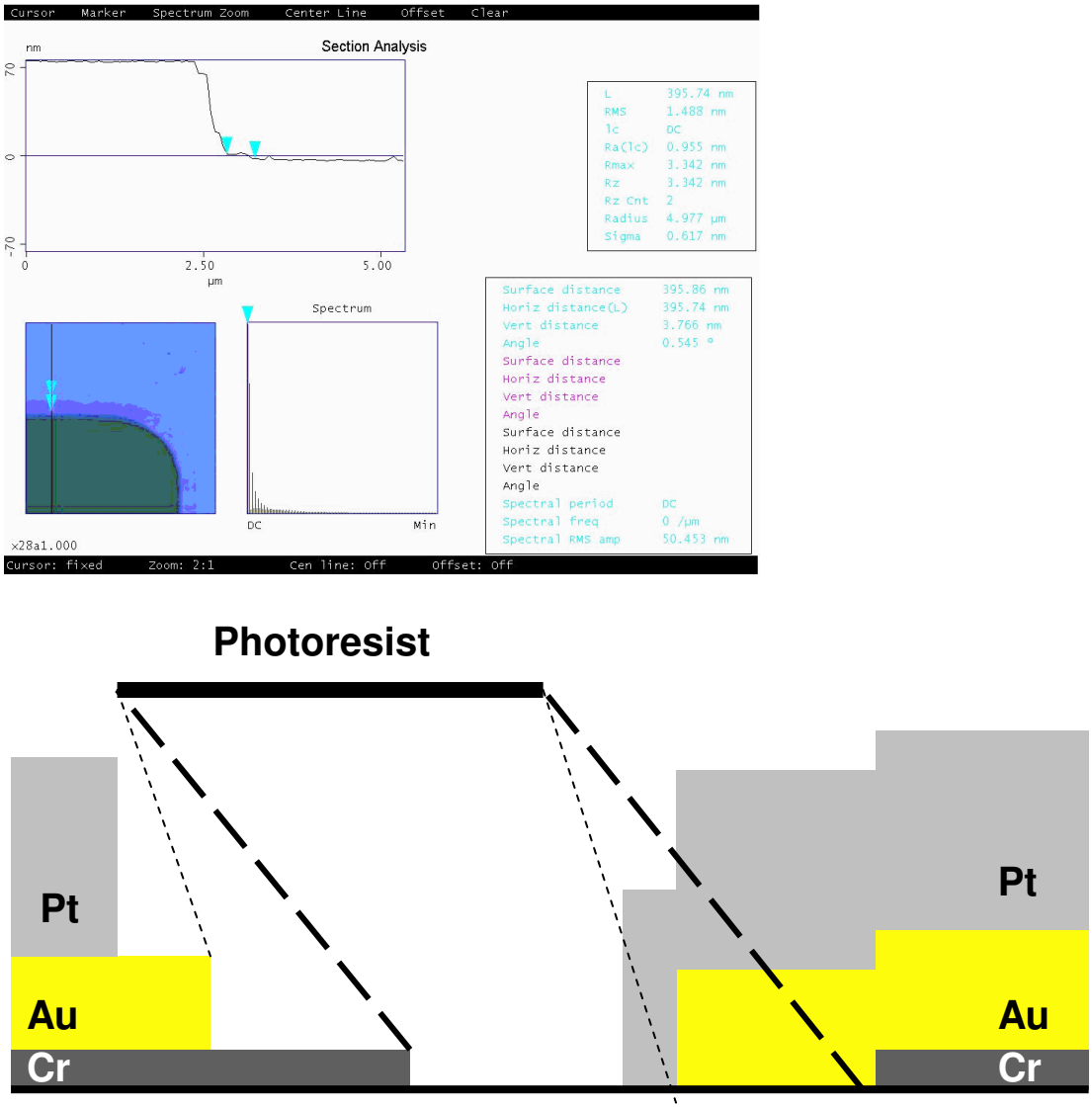

Figure 5.5. Top: AFM topography scan of the center lead in device A1, showing a 400 nm wide, 4 nm thick chromium layer offset from the 75 nm gold+platinum layer. Bottom: Schematic of the angle-evaporated contacts (distances not to scale).

The last fabrication step is the removal of all unwanted nanotubes, leaving only nanotubes in the active device area. Extraneous nanotubes, especially unaligned ones, can contact source and drain electrodes at angles that do not create Schottky

diodes, can connect adjacent devices and otherwise create complex and difficult to model conduction paths into the devices. Because one-third of CNTs are naturally metallic, increasing the number of tubes in a device decreases the probability that only semiconducting tubes will be incorporated into the diode as $(2/3)^N$ where N is the number of tubes involved. In the large-N limit, a large random mixture of as-grown CNT-SDs will have a forward-reverse ratio of 3:1. Thus, to obtain large rectification ratios, the channel width was limited to 10μm to include a small number of nanotubes, and excess nanotubes outside the device are were removed.

To remove unwanted nanotubes, a negative photoresist process was used. Photoresist NR9-1500PY was spun onto the samples at 3000 rpm for 60 seconds and baked for 1 minutes at 150 ºC. The samples were then exposed to 365 nm UV light for 10 seconds at an intensity of 9mW/cm^2 (90mW/cm^2 dose). The photoresist layer was allowed to polymerize for 10 minutes at room temperature, followed by a hard bake of 1 minute at 100 ºC. The samples were developed in Futurex RD6 developer and DI water solution (3:1) for 60 seconds and rinsed in DI water. The exposed nanotubes were then destroyed using an oxygen plasma reactive ion etch (RIE), using 250 mTorr of oxygen at a power of 300 W for 20 seconds. The photoresist was removed in Microchem Remover PG at 50 ºC. The resulting nanotube patterning can be seen in Figure 5.7.

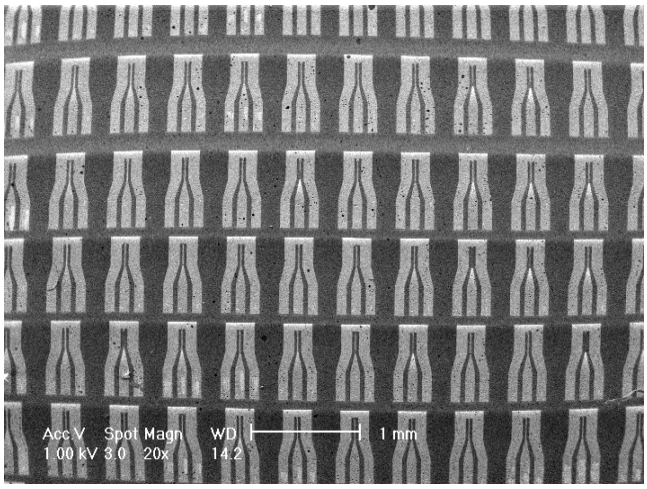

Figure 5.6. SEM micrograph of the CPW CNT device array. Only one-port devices are shown. Spherical distortion is due to SEM field-of-view limitations.

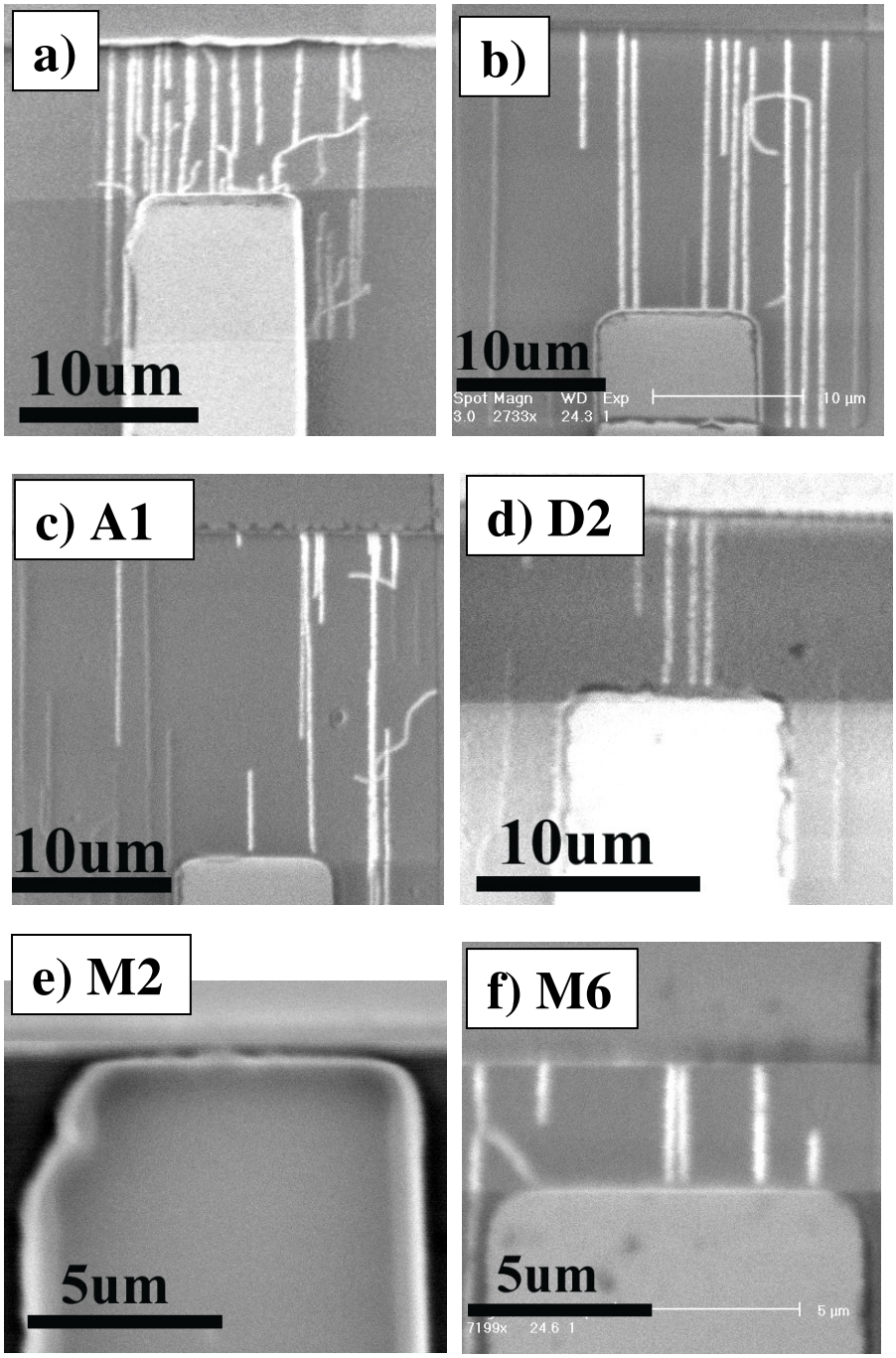

Figure 5.7. CNT devices after patterned etching. All tubes and portions of tubes outside the device area have been destroyed (images a and b). Images c through f correspond to CNT Schottky diodes measured in this work: c) Device A1, d) Device D2, e) Device M2, f) Device M6.

5.4 DC Measurements of Coplanar Waveguide Carbon Nanotube Schottky Diodes

As with the first-generation devices described in Chapter 4, the samples were loaded into a Cascade Microtech Summit 1200 automated probe station. The source probe was connected to a Keithley 2400 Sourcemeter while the drain probe was grounded. The Sourcemeter was controlled by the Cascade station's computer workstation via a GPIB interface, also used to download current measurement data. The stage's XY axes were software-aligned to the device array's rotation. A LabView program was written to automate DC characterization of the device array. In brief, the outermost two logical loops moved the Cascade Summit 1200 probe station stage through a programmable number of grid points with row and column spacing in microns. At each position, the software would ramp the Keithley Sourcemeter output voltage *V* from zero voltage to a minimum (e.g. -2 V) and ramp it up to a maximum (e.g. +2 V) while recording the current *I* at every step (e.g. every 100 mV). Some simple calculations (maximum absolute current and forward-reverse current ratio) were performed automatically for each device during characterization. With low yield rates, an array of 100 devices could be measured in approximately 30 minutes. However, if the current at a given array index was above threshold (e.g. 10 nA) and the current-voltage characteristic was asymmetric, indicating a good CNT-SD was present, the program would take a second *I-V* sweep at significantly higher resolution (eg. 10mV), thereby devoting more time to characterizing functioning diodes. Data for every device was saved separately to ASCII format files with the high-resolution data of successful diodes flagged for easy sorting. The yield rate for the fabrication

process (roughly defined as device forward-current greater than 50 nA and rectification greater than 5:1) was approximately 5-10%.

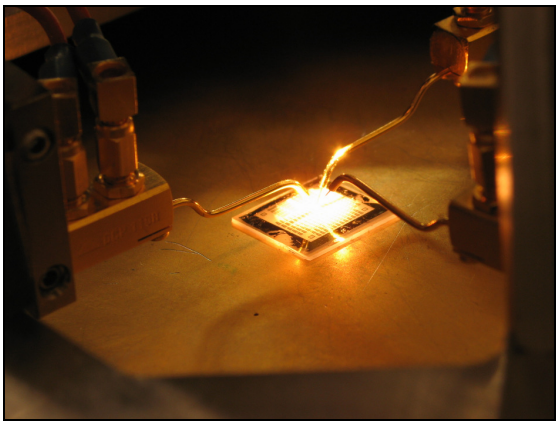

Figure 5.8. Optical photo of a CNT-SD array being probed by the automated Cascade Summit 1200 probe station for DC characterization.

5.5 DC Characteristics of Carbon Nanotube Schottky Diodes on Quartz

The selected diodes (labeled A1, D2, J3, M2 and M6) from three different samples (labeled X28, X29 and X36) were measured in detail in ambient and in vacuum in a Desert Cryogenics low-temperature probe station. Cascade ACP-50 GSG 150 BeCu microwave probes were used, connected to a Keithley 2400 SouceMeter controlled via GPIB by a custom LabView application.

To extract the intrinsic Schottky junction current-voltage characteristic (IV curve), a linear fit was performed in the high forward-bias region, with slope $1/R_s$

where R_s is the series resistance as described by the circuit diagram in Figure 5.9, inset. At low bias and under reverse bias, $R_J(V)$ is large and the voltage drop at the junction (V_J) is equal to the applied bias. As forward bias increases $R_J(V)$ decreases until it is comparable to R_S. Beyond this point the majority of the applied voltage is present across the channel resistance R_S and not at the junction. To determine the correct junction voltage V_J, the value of R_S is extracted from a linear fit in the linear forward-bias region. The junction voltage is then determined to be $V_J = V - IR_S$ where V is the applied voltage and I is the measured current. Additionally, a small global offset is added to the current values such that V = 0 at I = 0. In the case of diode A1, the offset is 14.7 nA. The reverse saturation current can then be extracted visually from the plot, seen in Figure 5.10.

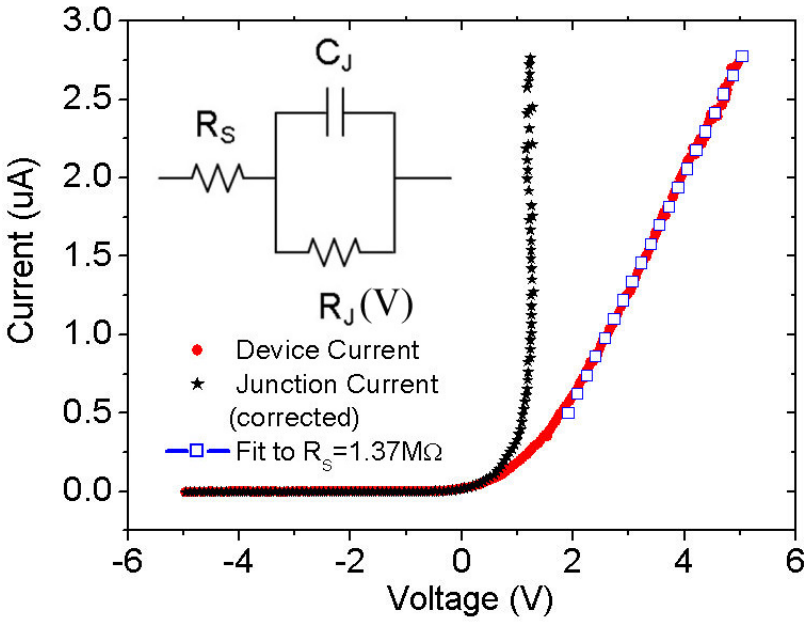

Figure 5.9 Current-voltage characteristic of a typical diode (A1). Current for the device (red circles) plotted against applied voltage and a linear fit (blue squares) to

R_S=1.37MΩ. The voltage drop at the series resistance is then accounted for, giving the current-voltage characteristic of the junction itself (black stars). Inset shows the circuit diagram following Cowley and Sorensen[84].

This corrected data was fit to the diode equation

$$I(V) = I_0 e^{\frac{eV}{nkT}} - I_0 \qquad \text{(Eq 5.1)}$$

where (kT / e) = 0.026eV with I_0 and n as fitting parameters. The ideality factors extracted in this way were in the range of n = 2.2 – 20. (Figures 5.10 and 5.11)

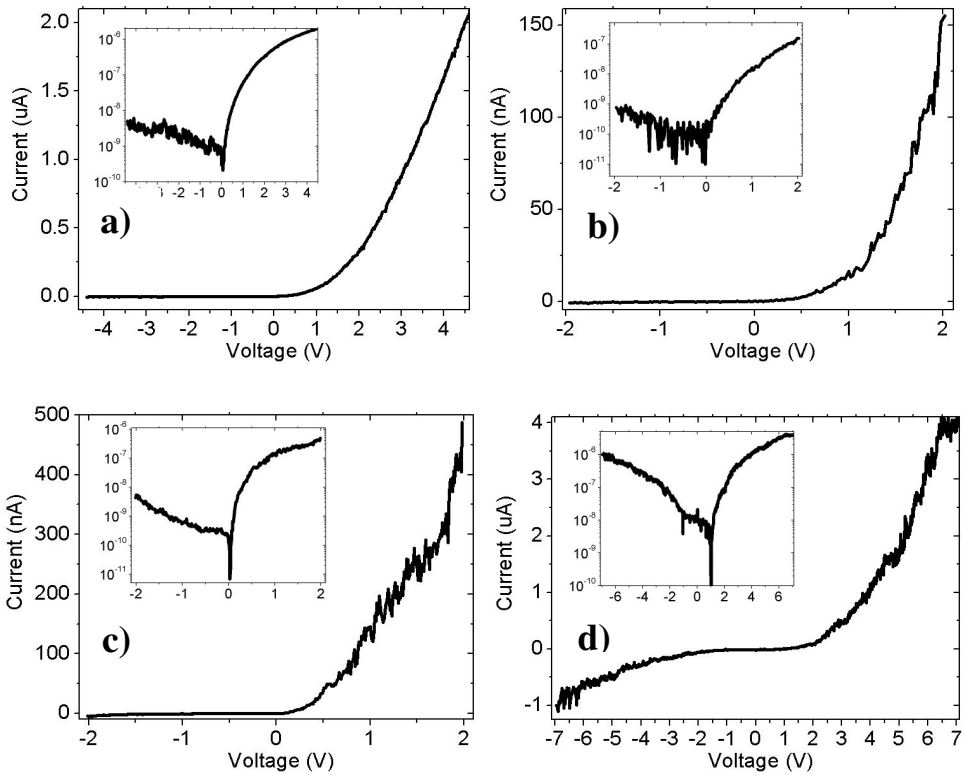

Figure 5.10 Current-voltage characteristics for four of the diodes studied in detail: a) A1, b) D2, c) M2 and d) M6.

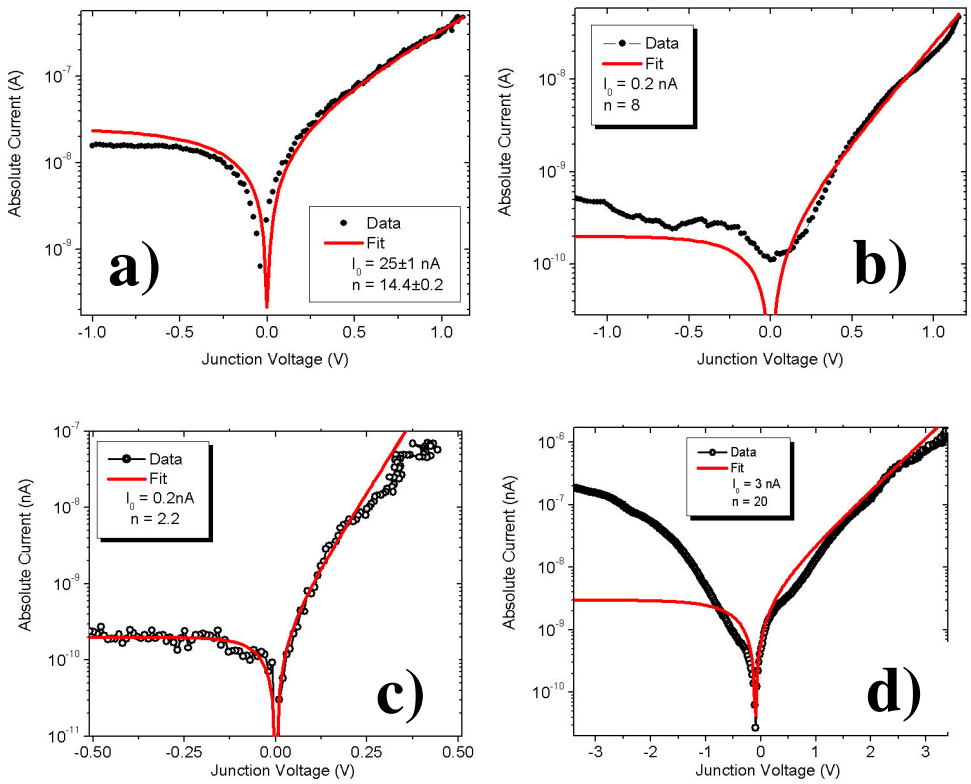

Figure 5.11 Smoothed absolute current-voltage characteristics of the other four diodes examined in Chapter 6: A1 (a, top left), D2 (b, top right), M2 (b, bottom left) and J3 (d, bottom right). Ideality factors extracted are n = 8, 2, 5 and 20, respectively.

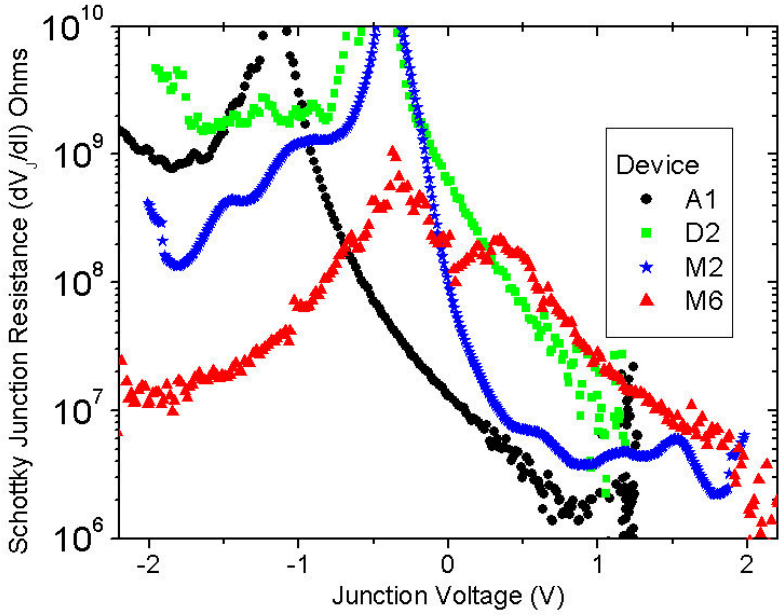

Figure 5.12. Junction resistance vs. junction voltage for the four devices studied in detail: A1 (black circles), D2 (green squares), M2 (blue stars) and M6 (red triangles).

Device Label	Rs	Ideality (fit)	Forward/Reverse Current Ratio
A1	1.38MΩ	14	210
D2	6.5MΩ	8	90
M2	4.3MΩ	2.2	270
M6	686kΩ	20	3

Table 5.1 Summary of series resistance, ideality factor fits and forward-reverse current ratios for the four devices studied in detail.

Ideality factors far different from 1 are uncommon in traditional thin film Schottky junctions but have been observed repeatedly in GaN nanowire Schottky junctions and Si nanowire Schottky Junctions. [83] As mentioned in Chapter 3, the small size and reduced dimensionality of nanowires and nanotube junctions may contribute to an unusually high magnitude of tunneling current, which may not follow the same bias dependence as the diffusion or thermionic emission models.

5.6 Scattering Parameter Characterization Coplanar Waveguide Carbon Nanotube Schottky Diodes

In this section, I describe a scattering parameter (S-parameter) measurement on one-port and two-port CNT-SDs. In general, these measurements were hindered by the large impedance of these individual and few-nanotube CNT-SD devices and the lack of a quartz-substrate calibration standard. Although the data obtained were ultimately not useful, the description and results are included here as an illustration of the difficulties in employing the usual microwave characterization techniques and equipment to nanostructures and thus the need for novel techniques such as Schottky diode rectification.

Scattering parameter (S-paramter) measurement is a standard frequency-dependent characterization technique for microwave systems. In one-port configuration, only one parameter, S_{11} is measured. S_{11} is the fraction the microwave signal which is reflected from the device under test (DUT), in units of dB. That is,

S_{11} = (Voltage received at Port 1 / Voltage output at Port 1)

In the case of a capacitor, for example, the impedance is

$$Z_c = (j\omega C)^{-1} \qquad \text{(Eq 5.2)}$$

and when put into the transmission line equation,

$$S_{11} = \frac{Z_{DUT} - Z_0}{Z_{DUT} + Z_0} = \frac{(j\omega C)^{-1} - 50\Omega}{(j\omega C)^{-1} + 50\Omega} \qquad \text{(Eq. 5.3)}$$

a frequency-dependent reflection coefficient is expected.

For two-port systems there are four parameters representing fractions of reflected and transmitted signal at each port as described in Equations 5.4 and Figure 5.13. The unit of an S-parameter is normally decibels (dB), with 0dB representing either perfect reflection (for S_{11} or S_{22}) or perfect transmission (for S_{21} and S_{12}).

$$S_{11} = b_1/a_1, \quad S_{21} = b_2/a_1, \quad S_{12} = b_1/a_2 \quad \text{and} \quad S_{22} = b_2/a_2 \qquad \text{(Eq. 5.4)}$$

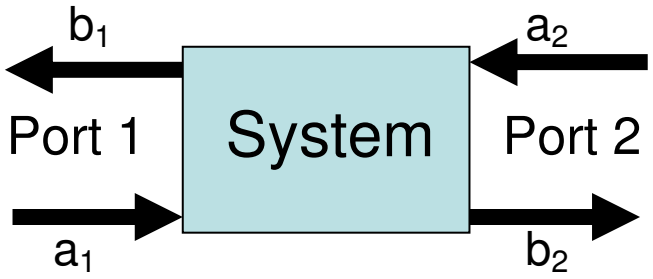

Figure 5.13. Schematic diagram of a scattering parameter measurement setup.

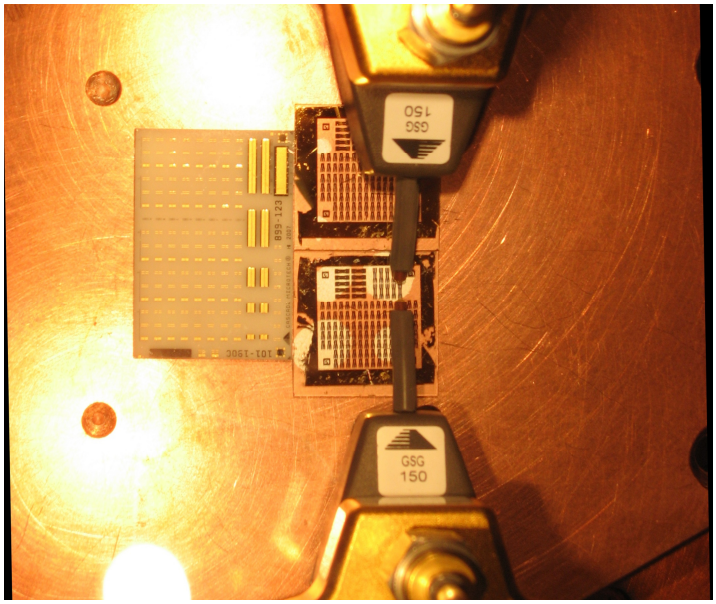

Figure 5.14. A top-view photograph of the measurement setup inside the Desert Cryogenics probe station. Pictured: Diode array samples X28 and X29, fused alumina calibration standard and ACP GSG probes.

A number of two-port devices were included in the photomask design for two-port scattering parameter and rectification measurements. The device studied here can be seen in Figure 5.15. Its dc current characteristic is shown in Figure 5.16. The impedance of the diode decreases from 1.8 GΩ to 3.4 MΩ as forward bias is increased, a factor of 529. In comparison with the standard 50 Ω equipment however, the signal transmission coefficients under forward and reverse bias are computed as

$$1 - [(3.4\ \text{M}\Omega - 50\ \Omega) / (3.4\ \text{M}\Omega + 50\ \Omega)] = 3\text{x}10^{-5} = 10^{(-45\ /\ 10)}$$

$$1 - [(1.8\ \text{G}\Omega - 50\ \Omega) / (1.8\ \text{G}\Omega + 50\ \Omega)] = 6\text{x}10^{-8} = 10^{(-72\ /\ 10)}$$

yielding expected transmission parameters (S_{12} and S_{21}) to be -45 dB and -72 dB for forward and reverse bias, respectively. This is within the specifications for the

Agilent E8364C PNA network analyzer used, which has a dynamic range of over 100 dB from 0.5 to 45 GHz.

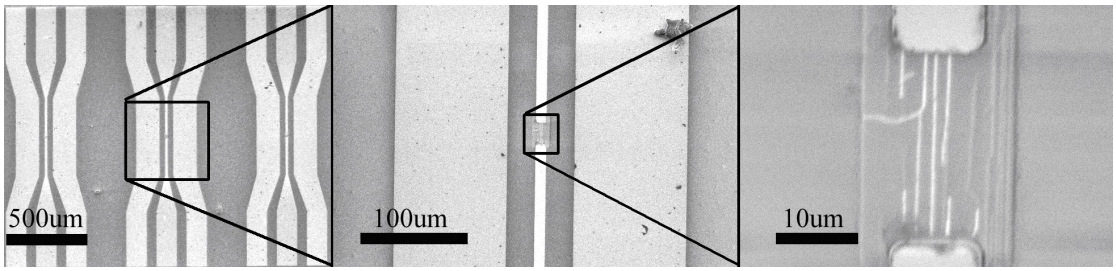

Figure 5.15. SEM micrographs of the two-port CNT-SD device U1.

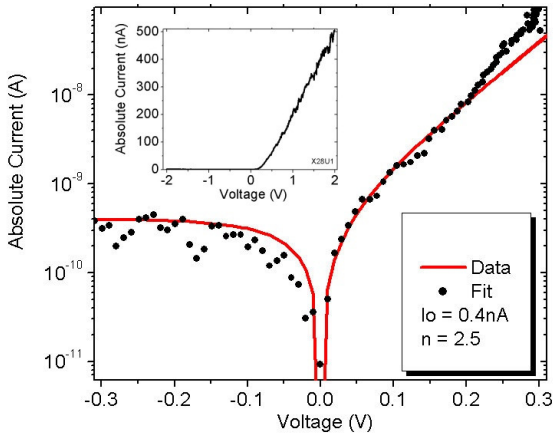

Figure 5.16 I-V curve for two-port diode U1. The device impedance varies between 3.4 MΩ and 1.8 GΩ under forward and reverse bias respectively.

Contact RF measurements were done at room temperature in ambient atmosphere in a Desert Cryogenics liquid helium probe station with dual Cascade ACP-50 GSG 150 BeCu microwave probes rated to 50 GHz (1.4dB insertion loss at 50 GHz) and all 2.4 mm microwave connectors (See Figure 5.9). Scattering parameter measurements (one-port for one-port devices, two-port for two-port

devices) from 10 MHz to 50 GHz were performed using an Agilent 8364B PNA and all 2.4 mm 50-GHz rated connectors. The network analyzer was calibrated using the network analyzer's Short-Open-Load-Thru (SOLT) procedure on the aforementioned calibration standard. Calibration was performed before each measurement run, with the scattering parameter data of the standard recorded before and after device measurements to detect calibration drift during measurement. Measurement was done by the network analyzer's own software. Rectification measurements (measurement of dc current) were attempted using the Agilent E8364C PNA, through the internal 50 GHz bias tees, but were found to be noisy without amplitude modulation (AM), which was not an installed option on the unit. Electrical contact to the CPW devices was found to be repeatable (the features in the scattering parameter spectrum were reproduced in subsequent trials for each device). In addition, the scattering parameters for the calibration structures were nearly identical when measured before and after device measurement, indicating the calibration did not drift appreciably during the measurement (Figure 5.17).

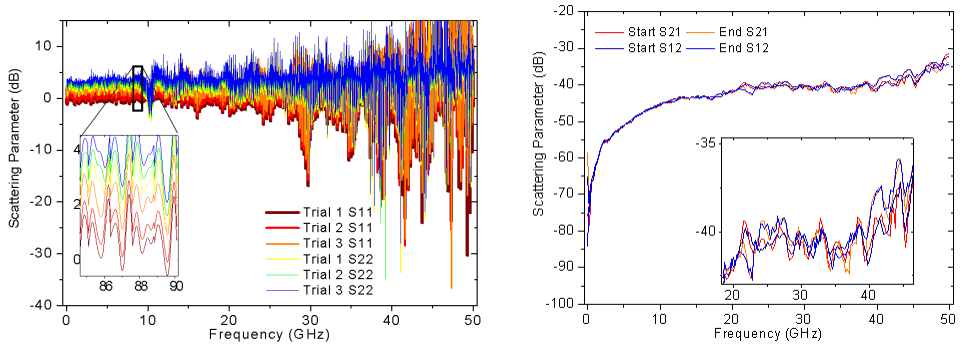

Figure 5.17. Scattering parameter checks of reproducibility (left) and calibration drift (right). The features in the spectrum are reproduced reliably on subsequent electrical

contact trials for each device. The scattering parameters for the calibration substrate are identical before and after the CPW CNT-SD measurements, indicating no calibration drift.

The measured S_{21} for a two-port diode is shown in Figure 5.18. Although differences are evident between the calibration standard open-circuit structure and the CNT-SD device, the transmission through the device is indistinguishable from signal transmission through an open-circuit CPW structure on the same sample, implying that this measurement is dominated by parasitic capacitance. Diode bias has no measureable effect on signal transmission. Additionally, the reflection coefficients for all structures on the sample array (diodes as well as open-circuit CPW structures) are all above 0 dB (reflection > 100%), indicating a calibration problem. The calibration standard used (Cascade Microtech Part #101-190) uses a fused alumina substrate with dielectric constant of 9.9, which is quite different than the CNT-SD quartz substrate's value (~ 4.5). While fabrication of short-circuit open-circuit and transmission line structures would not be difficult, creation of a calibrated 50Ω load would be less trivial.

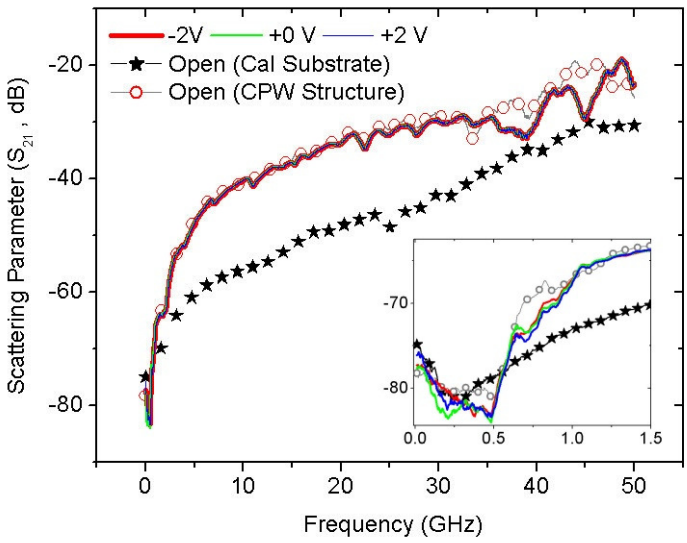

Figure 5.18. Transmission scattering parameter S_{21} for two-port CNT-SD. The (fused alumina) calibration substrate open-circuit struture's transmission is shown as black stars. Diode transmission under reverse bias (red line), zero bias (green line) and forward bias (blue line) conditions exhibit nearly identical impedances as an open circuit CPW structure on quartz (open circles). Inset shows minor deviations under 1 GHz.

In summary, this measurement highlights the obstacles presented by high-impedenace nanostructures to the usual high-frequency characterization techniques. Consequently, it demonstrates the need for the novel scheme of using Schottky diode rectification as a probe of CNT transport.

5.7 Microwave Rectification Measurement of Coplanar Waveguide Carbon Nanotube Schottky Diodes

Rectification measurements using the coplanar GSG probes were performed using a few different combinations of microwave hardware. Flexible 2.4 mm microwave cable 90 cm long rated to 50 GHz (Part #1401-240240-0360) and 2.4 mm-to-3.5 mm adapters were supplied by RF Depot Inc. Preliminary rectification measurements up to 12 GHz were performed using a 3.5mm Picosecond Pulse Labs bias tee model #5548 (10 MHz to 12.4 GHz) and an HP 83620B microwave signal generator.

After proof-of-concept, more extensive rectification measurements were performed using a Picosecond Pulse Labs #5543-206 bias tee. A Keithley 2400 Sourcemeter, connected to the dc port of the bias tee, was used to repeat the dc-properties measurement of each diode before the high frequency rectification measurement. An Agilent E8257C microwave source (250 kHz to 40 GHz) was used for frequencies above 3.2 GHz. It was found to produce a sharp and dramatic increase in the background modulated dc current below 3.202 GHz despite the bias tee. (This threshold at 3.200 GHz is evident in the instrument's data sheet as significant discontinuity in the power delivered and may signify a switch from one internal RF generator to another.) Thus the HP 83620B microwave source (10 MHz to 20 GHz) was used for frequencies below 10GHz, introducing a slight discontinuity in the dataset.

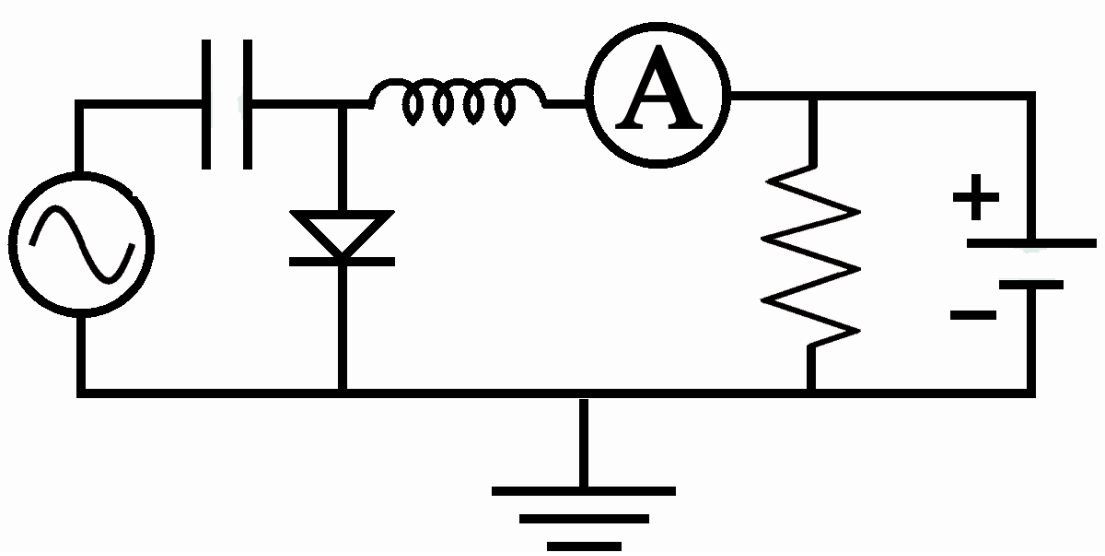

Figure 5.19. Circuit diagram of the rectification measurement setup. This circuit was used for all the final rectification experiment measurements. Note the lock-in amplifier (A) is floating, connected to ground by 10kΩ internal to lock-in.

Transmission line losses in the experimental setup prior to the CNT-SD were significant and reduced the available power reaching the diode. The manufacturer specification of delivered power vs frequency for both microwave sources used is shown in Figure 5.20. Although the maximum power is near +20dBm, the power-frequency relationship is highly non-linear at this setting, showing variations from +23dBm (200mW) to +17dBm (50mW) throughout the frequency range for the HP 83620B and 316mW to 63mW in the Agilent E8257C PSG.

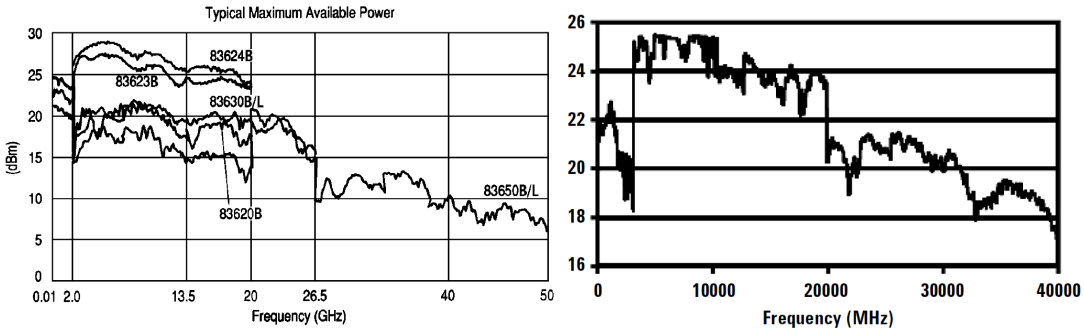

Figure 5.20. Manufacturer specified maximum power output (to 20 GHz) for the HP 83620B source (left) and for the Agilent 8257C (up to 40 GHz), also in units of dBm (right).

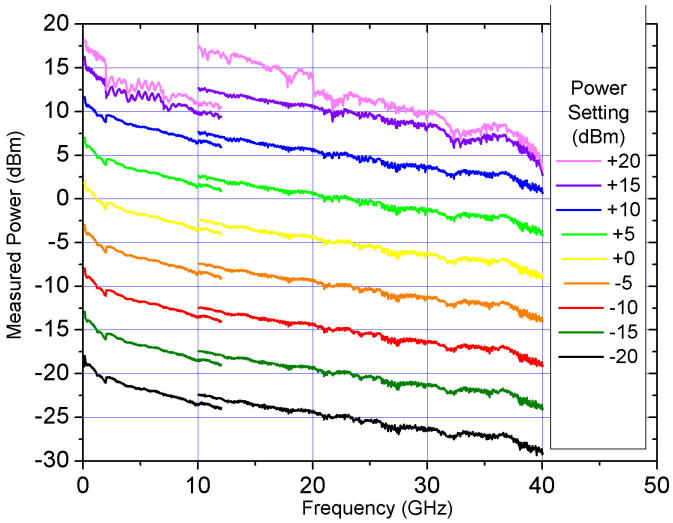

Figure 5.21. Measured power at the ACP probe connector for both sources (HP83620B below 12GHz and Agilent E8257C above 10GHz) as a function of frequency at various settings.

The power delivered by each source was measured using a 50GHz microwave power sensor (HP 8487A) connected to the cryostat internal probe connector in lieu of the ACP-50 GSG probe assembly, using a U-shaped adapter cable (RF Depot Part 8TS-241241-Y909). The sensor output was measured by a digital microwave power

meter (Agilent E4418B). A custom LabView program was used to turn off the RF power, zero the meter, turn on the RF power and sweep through the entire 3D parameter space (Frequency, Power, Bias) and record the measured power at each point. Meter averaging was set to 5 points. Figure 5.21 shows the measured delivered power by both microwave soruces as a function of frequency and power setting. To minimize the variation in power during frequency sweeps, the microwave sources were operated at power levels of +10, +5 and +0 dBm, well below their maximum outputs.

Because the ACP microwave probe was disconnected, this measurement replaces any losses incurred in the ACP probe assembly and the CPW leads with losses incurred in the adapter cable and sensor connector. The insertion loss of the Cascade Microtech ACP50-GSG-150 probe assembly is stated to be 1.4 dB at 50 GHz by the manufacturer. Its frequency dependence is shown in Figure 5.21 and is less than 0.5 dBm loss up to 40 GHz. There is also a noticeable ~3 GHz standing wave resonance evident in its reflection S-parameters S_{11} and S_{22} (see Figure 5.22), corresponding to a wavelength of (3 x 10^8 m/s) / 3 x 10^9 Hz = 10 cm or a half-wavelength path of 5 cm, which is approximately the distance between the connector and the ACP probe in the ACP probe assembly. Predictably, this resonance is present in the rectified current data as well.

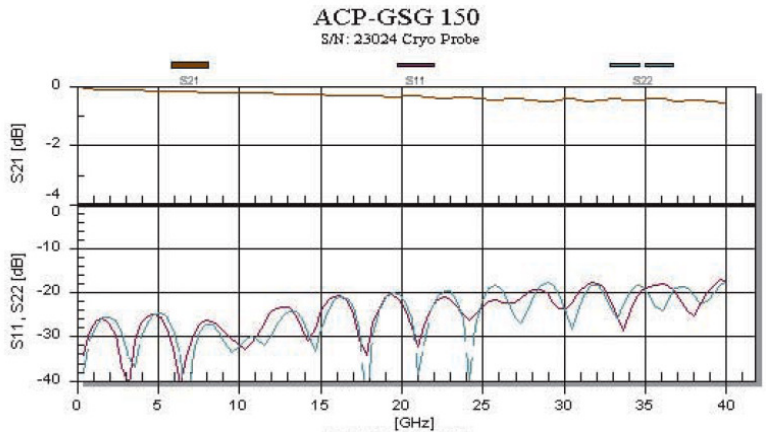

Figure 5.22. Manufacturer-specified transmission loss (S_{21}) and reflection parameters (S_{11}, S_{22}) for Cascade Microtech ACP50-GSG-150 cryogenic microwave probes.

5.8 Signal-to-Noise Ratio Optimization

The rectified current was measured by an SRS 830 lock-in amplifier at a modulation frequency f_{AM} of 200 Hz. Signal strength was found to have little dependence on f_{AM} except at multiples of the power line voltage (60 Hz), as shown in Figure 5.23 and 5.24. (The 60 Hz and 120 Hz filters were active, so the first sharp noise spike is at 180 Hz.)

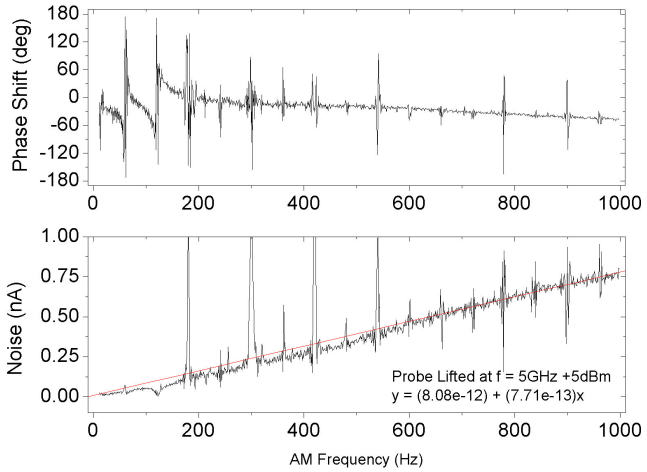

Figure 5.23. Background signal (from an open circuit) phase and magnitude vs. amplitude modulation frequency.

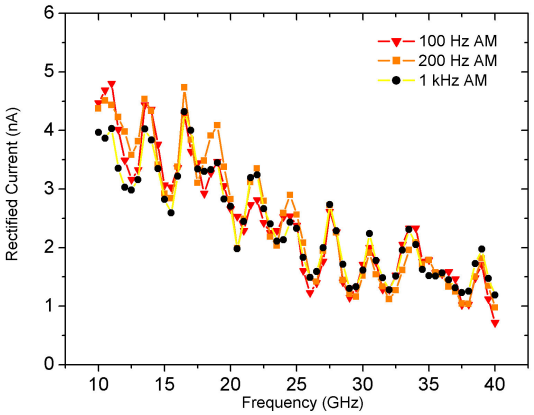

Figure 5.24. Raw rectified current data from device M6 from 10 GHz to 40 GHz at three different modulation frequencies: 100 Hz (triangles), 200 Hz (squares) and 1 kHz (circles).

Noise in the measurement was minimized with low modulation frequencies (~ 200Hz) and longer integration times (~300ms). To introduce the dc bias into the circuit, the SRS-830 lock-in amplifier was used in AC Float mode (internal 10kΩ

between LO input and ground) and a Keithley 220 Programmable Current Source in parallel with a custom resistor box functioned as a GPIB-controlled voltage source. A custom in-line ground bias box was built to apply the dc bias to the LO input on the lock-in amplifier.

A noise floor for the entire frequency range was established by contacting an open-circuit device (including CPW leads but exhibiting no detectable dc conductance). There was no observable effect from dc bias and minimal change in the noise floor based on the microwave source power setting. The noise floor is shown in Figure 5.25.

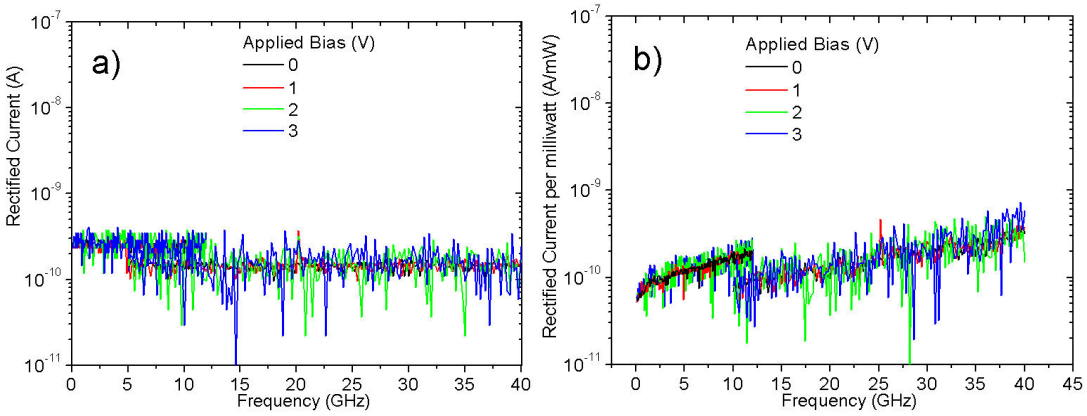

Figure 5.25. Rectified current (unmodified data) from an open-circuit CPW, (a). Current-per-milliwatt for the same open-circuit CPW, (b). Applied biases of 0V (black), 1V (red), 2V (green) and 3V (blue) are shown.

A second custom LabView application was created to automate RF measurement of each device. In brief, this software consisted of three nested loops which would cycle through all desired bias, power and frequency parameters and

obtain rectified current magnitude and phase information at each point. The resulting three-axis array was sliced into three two-dimensional arrays corresponding to constant-bias, constant-power and constant-frequency conditions. For data smoothing, an adjacent-average algorithm was used employing a third application coded in Python with the assistance of Daniel Lenski. This second application was also used to normalize the data by the measured source output power at each frequency and to scale the data to an arbitrary maximum value of 1.0 for comparison purposes. The code of this application is included in Appendix A.

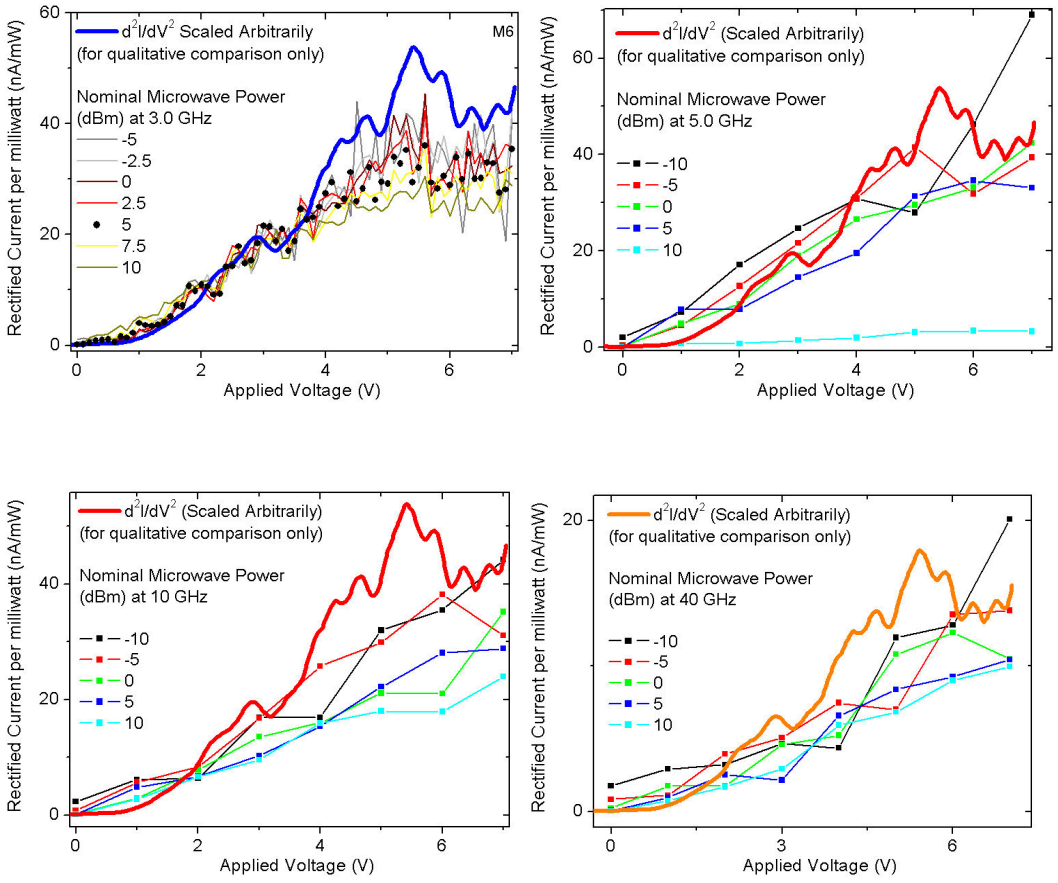

Figure 5.26. Rectified current for a CNT-SD (device M6) normalized to the applied power at various microwave frequencies: a) 3 GHz, b) 5 GHz, c) 10 GHz, d) 40 GHz.

Scaling the rectified current signal by the measured source output power yielded data in terms of Amps-per-Watt (nA per mW in Figure 5.26). The magnitude of this value was independent of power setting, indicating that the signal is proportional to the applied power as expected in the Square Law regime. Figure 5.26 shows this value plotted as a function of bias at four different frequencies in the measured range, for device M6. The IV-curve curvature d^2I/dV^2 is provided for qualitative comparison – the rectified current of a diode is also expected to be proportional to this function.

Chapter 6

Results, Analysis and Conclusion

"Lord, grant that my work increase knowledge and help other men. Failing that, Lord, grant that it will not lead to man's destruction. Failing that, Lord, grant that my article … be published before the destruction takes place."

-Walker Percy

6.1 Introduction

In this chapter I describe the results of microwave power rectification by the carbon nanotube Schottky diodes fabricated in coplanar waveguide (CPW) geometry as described in Chapter 5 as a function of bias and microwave frequency and power. The data are modeled using the lumped-element circuit introduced in Chapter 4 and the observed cut-off frequency is used to extract the junction capacitance C_J as a function of bias both in ambient and under vacuum (in the absence of ambient oxygen doping). The extracted values lie in the 10aF - 100 aF range for all five diodes studied in detail, both under ambient and vacuum conditions. Little dependence on applied bias is found, implying that the Schottky junction capacitance is dominated by stray capacitance between the bulk nanotube channel and the electrode. The results are compared to numerical electrostatic simulations which also show that device capacitance is dominated by channel length.

6.2 Extraction of Junction Capacitance from Rectified Current Signal

I measured five carbon nanotube Schottky diodes using the microwave rectification measurement setup discussed in Chapter 5 to obtain the rectified dc current output from the diode amplitude modulated at 200 Hz resulting from the amplitude modulated microwave excitation. This signal was used as a probe of the CNT-SDs transport properties at high frequency. Rectified current versus frequency for an example device (A1) is shown in figure 6.1. The current data was smoothed by a 20-point adjacent average as described in section 5.6. The signal exhibits early roll-off under low forward-bias values and this roll-off point moves to higher frequency with increasing forward bias (figure 6.1, top), as expected. In order to deconvolve the microwave source's varying power delivery, the data was normalized by the measured power output at every frequency value (figure 6.1, middle) as described in section 5.6. Lastly, the data for each bias was scaled to 1.0 (divided by its maximum) to ease visual comparison of the signal roll-offs (figure 6.1, bottom). The roll-off frequency, f_c, was defined as the frequency at which the signal power fell by half and the current amplitude fell 3dB:

$$(\frac{1}{2}P) = (\frac{1}{\sqrt{2}}I)^2 R = (0.707I)^2 R \qquad \text{(Eq. } \mathbf{6.1}\text{)}$$

I analyzed the bias-dependence of the roll-off frequency within the lumped-element model developed in chapter 4. The extracted roll-off frequency as a function of junction voltage $f_c(V_J)$ was compared with the results of the circuit model calculations using the measured R_s and $R_J(V_J)$ obtained from dc characterization and

various constant trial values of the junction capacitance C_J according to the cut-off frequency expression:[84]

$$f_c(V) = \frac{(1+\frac{R_S}{R_J(V)})^{0.5}}{2\pi C_J (R_S R_J(V))^{0.5}} \qquad \text{(Eq. 6.2)}$$

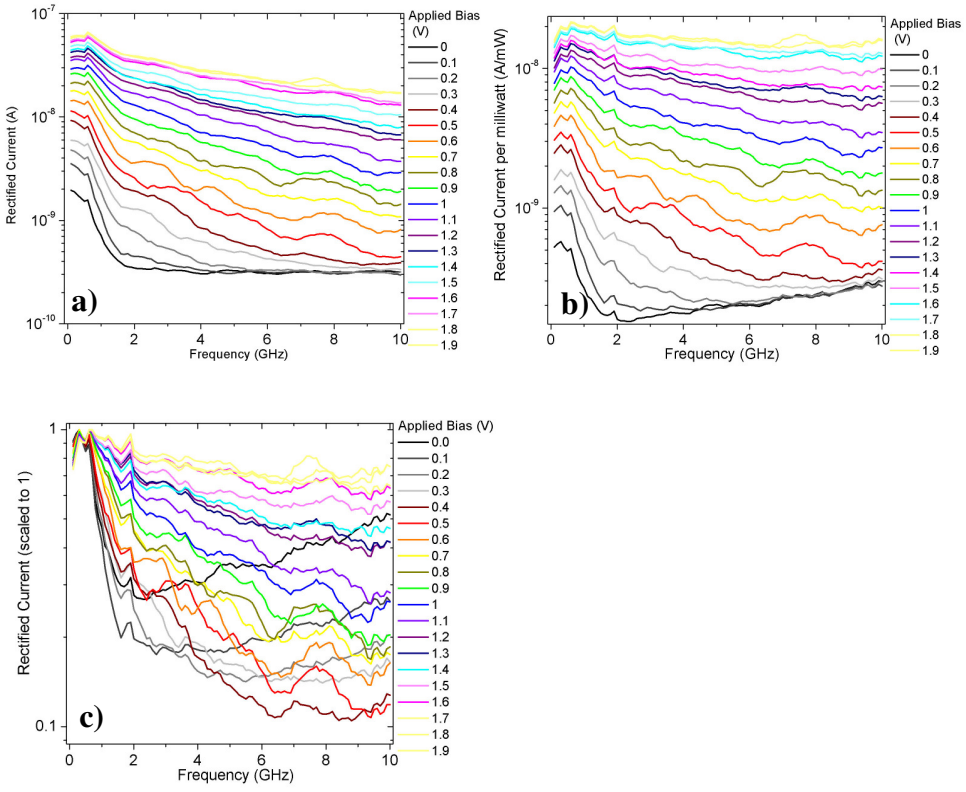

Figure 6.1. Rectification data vs frequency for device A1 under vacuum for bias conditions ranging from 0V to +1.9V in 0.1V increments. a) Smoothed rectified current. b) Rectified current per milliwatt. c) Rectified current was scaled arbitrarily to a maximum of 1.0 for visual roll-off comparison.

Similar analysis was performed for four other CNT-SDs that exhibit clear cut-off behavior within the parameter space explored. Equation 2 above was rearranged to solve for C_J, which I now assume could vary with V_J:

$$C_J(V_J) = \frac{(1+\frac{R_S}{R_J(V)})^{0.5}}{2\pi f_c(V)(R_S R_J(V))^{0.5}} \qquad \text{(Eq. 6.3)}$$

Using R_S and $R_J(V)$ from the dc *I-V* curve and f_c from the high-frequency roll-off, as seen in figure 6.1

6.2 Junction Capacitance in Ambient

Figure 6.2 shows the extracted capacitance $C_J(V_J)$ for diode A1. The junction capacitance is fairly constant, indicating that the simple Schottky circuit model using a mean junction capacitance of C_J = 108 aF is sufficient to explain the frequency dependence of the rectification data in the bias range 0 V to +1.2 V. The error bars correspond to the standard deviation of the data, which is 25 aF. Similar constant-capacitance behavior is observed in diode D2, as shown in figure 6.3, with a corresponding mean junction capacitance of 15 ± 7 aF). Table 1 below summarizes the mean junction capacitances observed in four out of five devices studied, along with channel length and the number of CNTs involved.

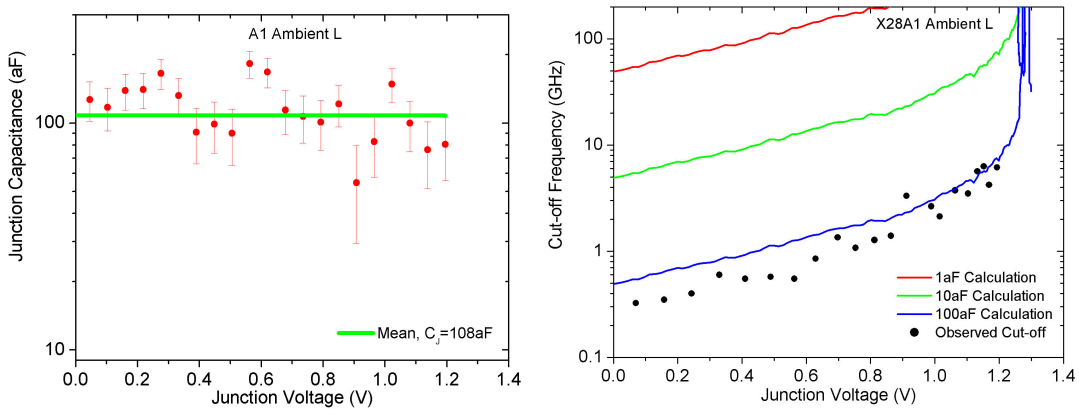

Figure 6.2. Microwave rectification parameters for device A1 under ambient conditions. (left) Observed cut-off frequency (black circles) as a function of junction voltage (V_J) compared to simulated results of equation 6.2 using the observed R_S and $R_J(V_J)$ values and junction capactances of 1 aF (red line), 10 aF (green line) and 100 aF (blue line). (right) Junction capacitance as a function of junction voltage (V_J) clculated from equation 6.3.

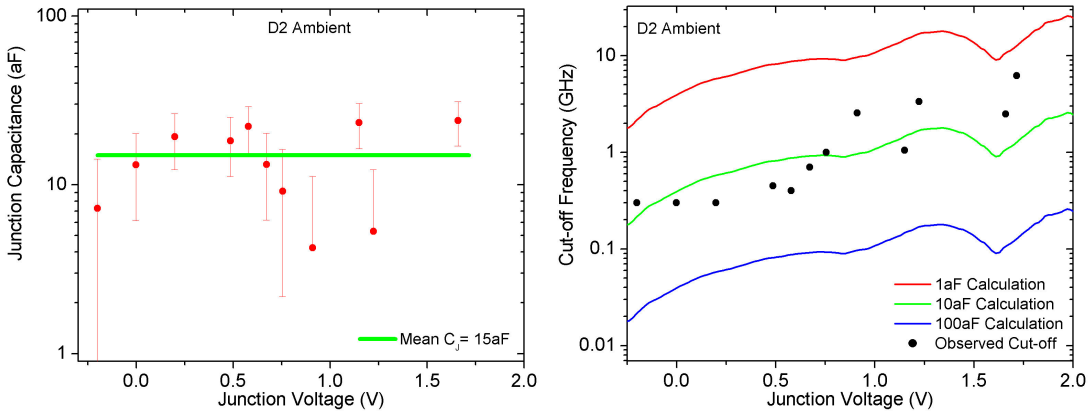

Figure 6.3. Microwave rectification parameters for device D2 under ambient conditions. Left: Observed cut-off frequency (black circles) as a function of junction voltage (V_J) compared to simulated results of equation **6.2** using the observed R_S and $R_J(V_J)$ values and junction capacitances of 1 aF (red line), 10 aF (green line) and 100

aF (blue line). Right: Junction capacitance as a function of junction voltage (V_J) calculated from equation 6.3.

Capacitance values extracted for the shorter devices (1-7 μm) lie in the 10-20 aF range despite each device including several nanotubes. In contrast, the longer single-tube device A1 exhibits a much larger junction capacitance of approximately 100 aF. The observation of a larger junction capacitance for a longer device supports the hypothesis that CNT-SD capacitance is dominated by stray capacitance due to the lack of shielding in a 1D structure. This hypothesis is explored further using electrostatic simulations in section 6.4.

Device	$C_j \pm \sigma$	l **(μm)**	**# tubes**
A1	**108**±25	**20**	**1**
D2	**15**±7	**7**	**3**
M2	**8**±6	**1**	**n/a**
M6	**20**±9	**3**	**3**

Table 6.1. Mean junction capacitances, standard deviation, channel length and number of nanotubes for four of the diodes studied in ambient. The number of nanotubes in diode M2 is difficult to determine due to its very short channel length.

6.3 Junction Capacitance in Vacuum

CNTs are *p*-doped under ambient conditions by atmospheric moisture and oxygen[71]. To enlighten the effect of doping on high-frequency transport properties, the diodes were measured in high vacuum (10^{-6} Torr), which is expected to reduce the *p*-doping. In the extreme case, an intrinsic CNT channel should produce high series resistance and symmetrical Schottky contacts with ambipolar transport, eliminating the rectification that results in the doped case. In the more realistic intermediate case, the p-doping and therefore charge carrier concentration *n* would be reduced. The observable result would be *increased channel resistances* and *decreased junction capacitances* due to the longer depletion lengths that result from lower *n*. However, the change in junction capacitance would only be evident in cases where the stray capacitance does not dominate.

Figure 6.4 shows the junction capacitances extracted for diodes A1 and D2 under high vacuum conditions. Table 2 shows a summary of the extracted capacitances under high vacuum conditions. Diode J3 was not measured in vacuum. The values of the junction capacitances under high vacuum are comparable to those under ambient conditions. A weak correlation between junction capacitance and junction voltage is evident in the data from the shorter diodes: D2, M2 and M6. The data was fitted to an exponential dependence as per equation 6.4. The correlations

were 0.78, 0.65 and 0.59 for diodes D2, M2 and M6 respectively. The exponents were 0.4, 0.5 and 0.7 respectively.

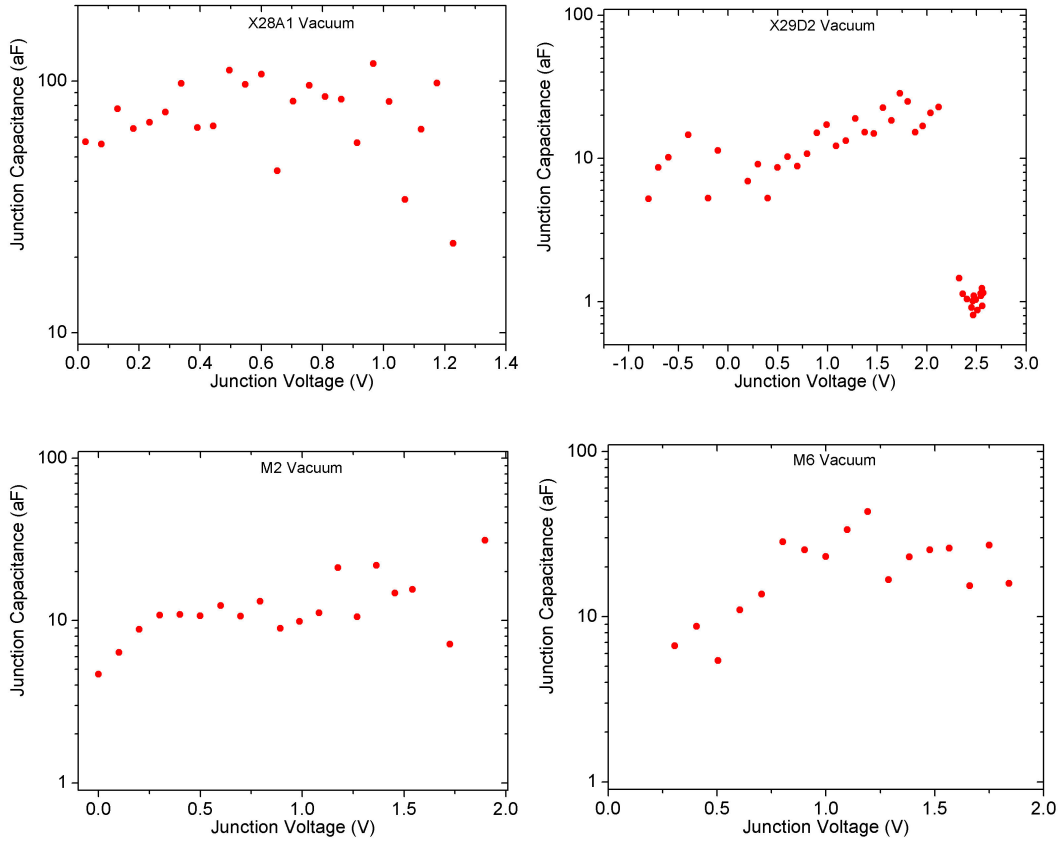

Figure 6.4. Junction capacitance corresponding to observed cut-off frequency values, according to equation 6.3, for diode A1 (top left), D2 (top right) , M2 (bottom left) and M6 (bottom right), measured under high vacuum to reduce doping. A weak positive trend is evident in the shorter, small-capacitance diodes (D2, M2 and M6). Diode A1 is 20 µm long, and appears dominated by stray capacitance of about 100 aF.

Device	Mean $C_J \pm \sigma$ (aF)	l (μm)	# nanotubes
A1 (ambient)	**108** ± 25	**20**	**1**
A1 (vacuum)	**71** ± 21		
D2 (ambient)	**15** ± 7	**7**	**3**
D2 (vacuum)	**8** ± 7		
M2 (ambient)	**8.3** ± 6	**1**	**n/a**
M2 (vacuum)	**12** ± 5		
M6 (ambient)	**20** ± 9	**3**	**3**
M6 (vacuum)	**21** ± 10		

Table 6.2**.** Junction capacitances, channel length and number of nanotubes for each of the CNT-SDs studied in detail under ambient and vacuum conditions.

The Schottky junction capacitance is expected to be a function of the depletion region width, which in turn depends on junction voltage. However, the observed dependence of the junction capacitance on junction bias is weak, leading to the conclusion that junction capacitance is dominated by stray capacitance between

the CNT channel and the metal electrode. To further validate this hypothesis, electrostatic simulations were performed as described in 6.4

6.4 Electrostatic Simulation Setup

In order to understand the apparent dependence of the capacitance of the CNT Schottky diodes on CNT length as seen in Tables 1 and 2, I performed electrostatic simulations to estimate the stray capacitance between CNT and electrode and its dependence on various geometrical parameters. The simulations were performed on Ansoft's Maxwell 3D v12 electrostatic simulation software. Various simplified models of the CNTSDs were used, an example of which ("Simulation 1") is shown in figure 6.5. Here the nanotube of interest lies on a quartz substrate and is co-planar with a metal electrode. The nanotube is separated from the electrode by a distance *D*, representing the depletion length. To examine the case where multiple nanotubes lie near the nanotube of interest, the model includes a second nanotube, parallel to the first one but electrically connected to the electrode.

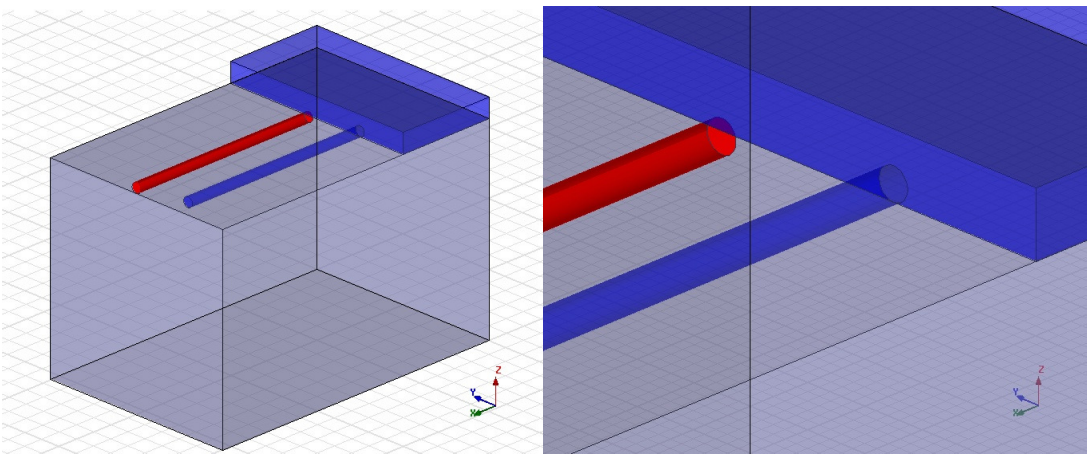

Figure 6.5. A three-dimensional rendering (left) of the first simulation geometry: a nanotube, modeled as a perfectly conducting cylinder (red), is placed on top of a quartz substrate (green). The electrode (blue) is modeled as a 100 nm thick rectangular conductor with an attached 50 nm nanotube parallel to the channel nanotube, modeling the situation in device A1. The separation, *D*, between channel and electrode is better seen in the close-up image of the contact area (right).

When using any finite-difference simulation such as this, two frequent concerns are the mesh size, which determines the spatial resolution of the simulation, and the boundary conditions. Mesh size is particularly problematic for devices involving nanostructures because the fine meshes necessary to resolve nano-scale objects and phenomena are memory-intensive at large scales. Ansoft's Maxwell 3D v12 application uses an adaptive mesh procedure which uses different mesh sizes for different spatial regions of the model. To check the effectiveness of this adaptive meshing, the mesh size was reduced manually to 2 nm in the region with fine detail

near the depletion region. The manual meshing was found to make no difference in the simulation results, indicating that the automatic adaptive mesh size determination was working adequately. As a boundary condition, the software assumes the electric field normal to the edges of the region of interest is zero, therefore tight boundaries would artificially constrain the electric field to the simulation region, which may be unrealistic. The positions of the boundaries (termed *padding* and represented as a percentage of the size of the objects in the model) was varied between 25% and 125% for all three dimensions. The results of the capacitance calculation, shown in figure 6.6, clearly show that even tight boundaries (25% padding) do not affect the calculated capacitance.

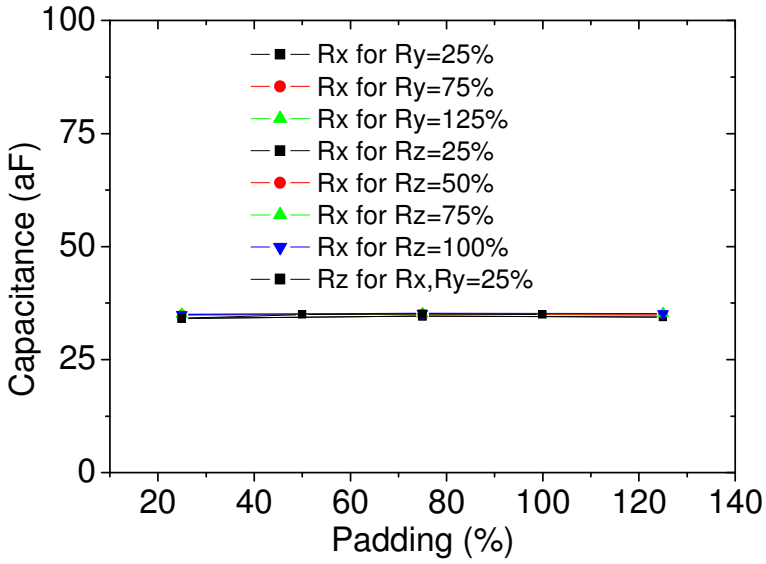

Figure 6.6. Capacitance for the model shown in figure 6.7 as a function of size of the simulated region (boundary position) in units of percentage of the size of simulated objects along each dimension. For a 2µm x 1µm x 1µm simulated device, setting X and Y padding to 100% increased the simulated region to 6 µm x 6 µm x 1 µm. All

boundary conditions explored (including 125% Z-padding) had a negligible effect on capacitance.

Simulation Parameter	**Nominal Value for Simulation 1 (μm)**	**Nominal Value for Simulation 2 (μm)**	**Realistic Value (μm)**
Substrate Thickness	1	1	500
Device Width	1 (varied)	1 (varied)	1000
Electrode Length	1	1	10
Electrode Thickness	0.1	0.1	0.1
Nanotube Length	1 (varied)	1 (varied)	20
Depletion Length	0.05 (varied)	0.05 (varied)	0.05
Nanotube Radius	0.025 (varied)	0.025 (varied)	.001
Parallel Tube Length	1	n/a	10 (A1)
Parallel Tube Separation	0.25	n/a	1 (A1)

Table 6.3. Geometrical parameters for the electrostatic simulations, along with nominal simulated values for Phase 1 simulation and realistic values.

The nominal values of various geometrical parameters are summarized in table 6.3. While the capacitance values calculated from this first simulation were in general agreement with the experimental results, the geometry resulted in high field concentrations at the CNT – substrate interface. Although there is a high curvature at

that interface, representing the CNT as a perfect cylinder and the substrate as a perfect plane is unrealistic, so the extremely high field concentrations observed in the results (figures 6.7 and 6.8) were suspect.

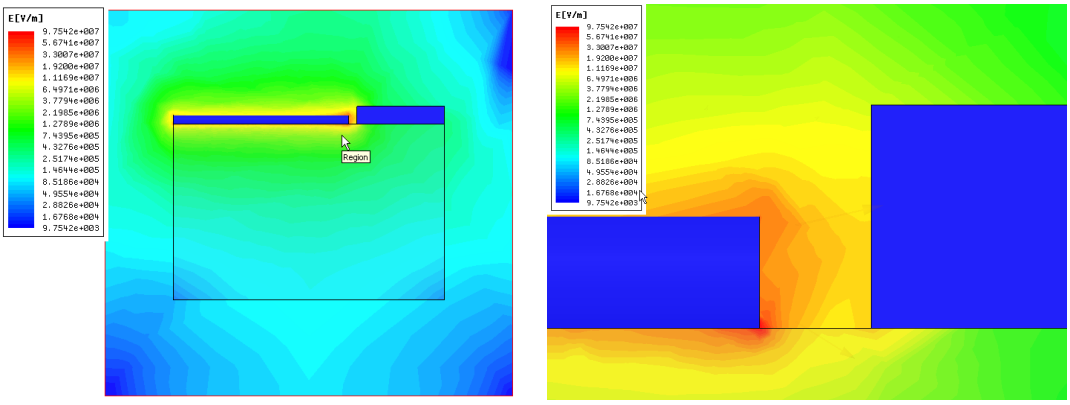

Figure 6.7. Cross-section of the electric field magnitude (left) and a close-up of the field intensity near the depletion zone (right).

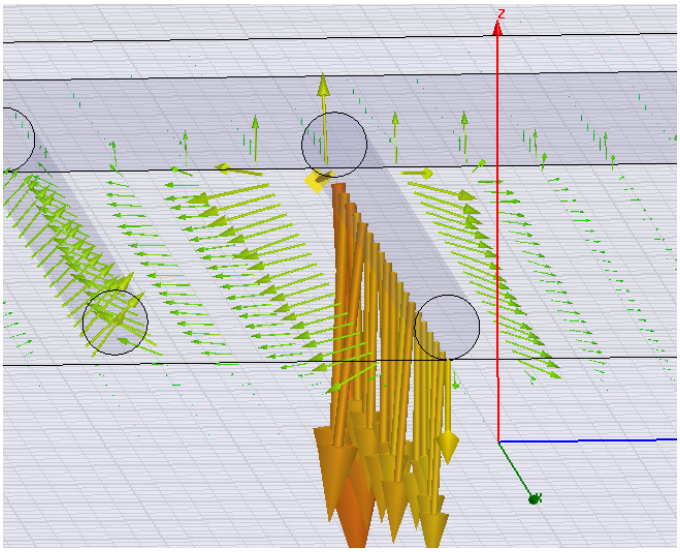

Figure 6.8. A 3D vector plot of the electric field intensity and direction in the model shown in figure 6.7. The infinitely sharp boundary between the cylindrical nanotube and the planar substrate surface leads to very high localized electric fields.

To avoid these high field concentrations, a second geometry ("Simulation 2") was simulated, shown in figure 6.9. Here the nanotube is embedded in the dielectric at a depth of about 50nm. The lack of a three-material boundary (e.g. quartz-air-nanotube) minimized the field concentration effects seen in the first simulation.

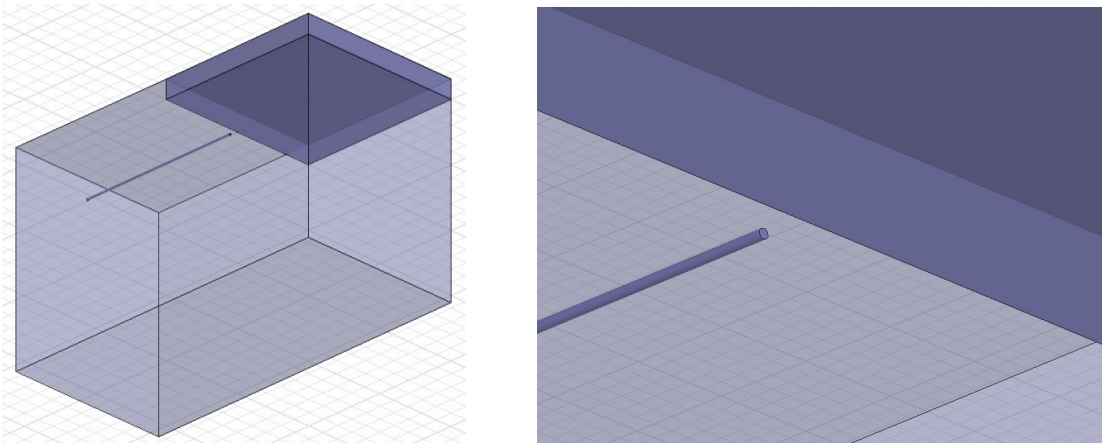

Figure 6.9 A three-dimensional rendering (left) of the overall simulation geometry, and a close-up of the simulated junction (a gap between a conducting cylinder and an electrode). Unlike in the first simulation, here the nanotube is embedded in quartz, avoiding the sharp boundaries of a perfect cylinder meeting an ideal plane. The nanotube diameter is 5nm.

6.5 Electrostatic Simulation Results

The capacitance calculations for both geometries (figures 6.7 and 6.11) showed qualitatively similar relationships to depletion length and channel length. The

size of the gap representing the depletion region was systematically varied between 1nm and 250nm and the capacitance calculated for each simulation solution. The dependencies of the capacitance on the depletion length and nanotube radius are shown in figure 6.10. The depletion length had a small effect on the junction capacitance. In contrast, varying the nanotube channel length while holding the depletion length constant resulted in a dramatic change in junction capacitance, shown in figure 6.11. The saturation observed with channel length was found to vary based on the simulated electrode width (figure 6.11 b). The simulation results are consistent with the experimental results in showing that the CNTSD junction capacitance is dominated by stray capacitance between the CNT bulk and the electrode, and thus largely constant with bias, and not by the length of the Schottky barrier, which is expected to be bias-dependent.

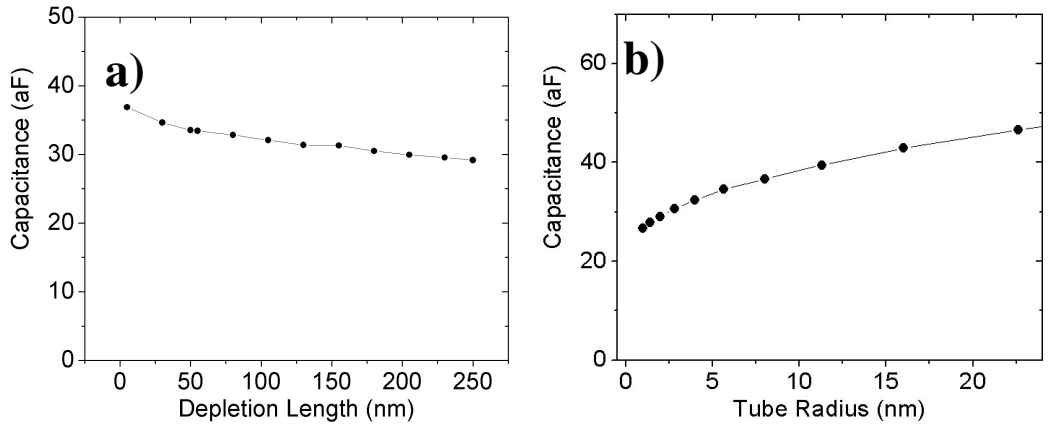

Figure 6.10. Capacitance as a function of simulation parameters a) depletion length, represented by the gap between the conducting cylinder and the electrode, and b) nanotube radius, for the geometry shown in figure 6.9.

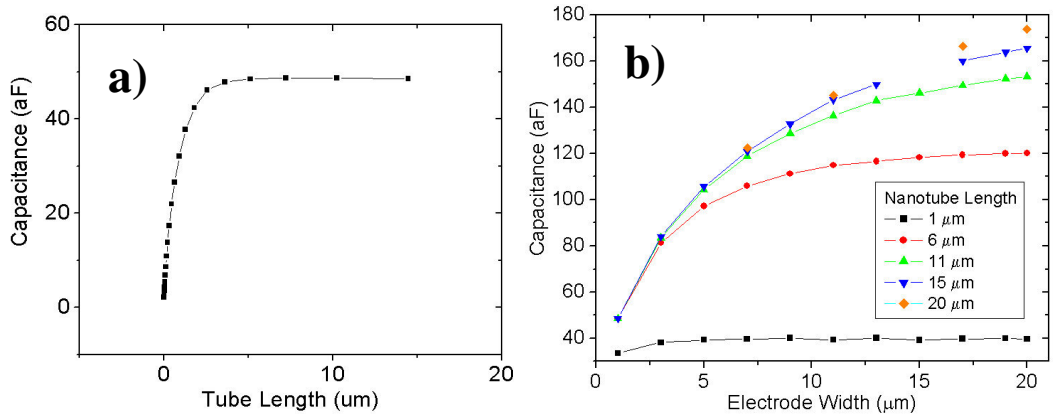

Figure 6.11. Calculated capacitance as a function of a) nanotube channel length and b) electrode width for nanotubes of length 1μm (black squares), 6μm (red circles) and 11μm (green triangles).

6.6 Transmission Resonances

The mean free path of CNTs at room temperature is approximately 1 μm[62, 63] as discussed in chapter 2. Given charge carrier velocities between $8x10^5$ m/s and $3x10^6$ m/s (the fermi velocity and Luttinger liquid plasmon velocity, respectively) the corresponding resonance frequency range is $f_0 = (8x10^5 / 10^{-6}) \rightarrow (3x10^6 / 10^{-6}) =$ 800GHz → 3 THz. Using a capacitance value of 10 aF, in accordance with the results in sections 6.3 and 6.4, the necessary device impedance is below 20 kΩ. This value is achievable in ohmically contacted CNTs, but unlikely when including a rectifying Schottky contact. Thus one would not expect to observe transmission resonances at room temperature. However, mean free paths as long as 20 μm have been demonstrated[64] at temperatures of 150K. Transport resonances in at this temperature would be observable in devices with l = 10 μm, at frequencies of 40GHz → 150

GHz. For a capacitance of 10 aF, this corresponds to an achievable device impedance of 398 kΩ → 106 kΩ for Fermi and the Luttinger liquid models, respectively. However, a study of temperature-dependent high-frequency rectification by carbon nanotube Schottky diodes has been relegated to the realm of future work. The rectification signal up to 40GHz at room temperature can be seen in figure 6.14. The oscillations with period ~3GHz match the transmission resonance shown in the ACP probe data sheet, figure 5.21. A better (temperature-dependent) calibration of the power reaching the CNT-SD is needed to eliminate these signal oscillations.

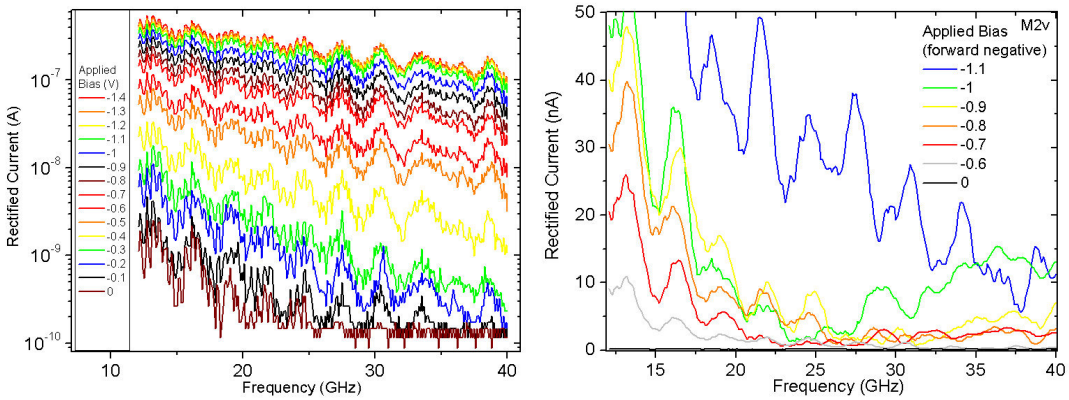

Figure 6.12. Rectified current data (unprocessed) from device M2 a) in ambient, Log scale, showing rectified current of 100nA at 40GHz under 1.4 V of forward bias, and b) in vacuum, linear scale. Plot b shows a decrease in rectified current near 25GHz for bias values between 0.7 V and 1.0 V, followed by a recovery at higher frequencies.

6.6 Discussion and Conclusion

In the work described here, I synthesized small-diameter carbon nanotubes on high-frequency compatible sapphire and quartz substrates, and fabricated few and single-tube CNT Schottky didoes using dissimilar metal contacts in a 50Ω CPW geometry. By applying microwave signals of up to 40 GHz to these novel CPW CNT-SD devices and measuring the rectified current output I was able to observe the behavior of the cut-off frequency $f_c(V)$ as a function of bias despite the large impedance mismatch inherent between nanostructures and equipment. I then extracted the junction capacitance $C_J(V)$ for devices of different channel lengths and number of nanotubes under many bias conditions using a simple circuit model. Further, I repeated the experiment in vacuum in order to observe the effect of ambient oxygen doping on the junction capacitance value.

The junction capacitance extracted indicate $C_J(V)$ is slightly larger than predicted by theory (10 - 100 aF) but in agreement with other experimental observations[13]. A circuit model incorporating a constant junction capacitance was sufficient to explain the high-frequency rectification results, indicating that junction capacitance varies only very weakly with junction bias. Instead, by studying devices with a range of carbon nanotube channel lengths from 1 μm to 25 μm, I observed a positive relationship between channel length and junction capacitance, indicating that junction capacitance is dominated by stray capacitance between the electrode and the bulk of the nanotube channel. I used numerical electrostatic simulations to compute

the stray capacitance as a function of various geometrical parameters. Simulation results are in broad agreement with the value of C_J extracted from experimental data. Analysis of the simulated geometry indicates that junction capacitance is sharply dependent on device geometry parameters such as channel length and electrode width, and largely independent of Schottky barrier width.

The main implication of these results for high-frequency one-dimensional nano devices is that device capacitances will be dominated by stray capacitances. Therefore, there is indeed little disadvantage to using multiple short, parallel channels to achieve higher conductance (e.g. impedance matching to 50 Ω), as recently attempted by Ho et al[104]. In addition, in this instance, contact resistance and not channel resistivity dominates the dc performance (and by extension the *RC* time constant and cut-off frequency) of CNT-SD devices.

Schottky diode rectification has been demonstrated here to probe CNT transport at frequencies up to 40GHz with little extrinsic limitation. As indicated by the experimental and simulation results, by shortening the channel length and reducing electrode width, junction capacitances of 10 aF or less are realistic. If combined with lower-resistance contacts (e.g. 100 kΩ), diode cut-off frequencies beyond 100 GHz are feasible. Combined with lower temperatures (~ 150 K) which would lengthen the CNT mean free path towards 20 μm, this technique could detect resonances characteristic of novel one-dimensional transport phenomena.

Appendices

Appendix A

This is the Python code used to smooth the CNT-SD rectified current data, normalize to the measured power output and arbitrarily scale the resulting data to 1. The adjacent-averaging routine was developed by Dan Lenski.

```
#!/usr/bin/python
import sys
import numpy as np

n = int(sys.argv[1])
error = 0
reason = "Empty"
#cname = sys.argv[2]
fname = sys.argv[2]

def intro(n):
    # Prints some relatively useless information on the screen
    print "----------------Intro-------------"
    print "Usage: :\Command n DataFile"
    print "Adjacent Average:", n
    #print "CalFile:", sys.argv[2]
    print "DataFile:", sys.argv[2]
    print "Output Files: Adjacent-Average Smoothed Data:","a"+sys.argv[2]+".a"
    print "Output Files: Tranposed Original Data:", "t-"+sys.argv[2]+".tp"
    print "Output Files: Normalized Data:", "n-"+sys.argv[2]+".n"
    print "---------------------------------"

def printstuff(raw,cal,freq,bias,data):
    #State some important things like the size of arrays and
    #a sample of each one for diagnostic purposes
    #print "---------Printstuff-------------------"
    print "    Spreadsheet Dimensions:", raw.shape
    #print "File Sample:"
    #print raw[0:5,0:4]
    print "    Cal Dimensions", cal.shape
    #print "Cal Sample:"
    #print cal[0:8,0:2]
    print "    Transpose Dimensions:", tp.shape
    #print "Transpose Sample:"
```

```
    #print tp[0:5,0:3]
    print "   Data Dimensions:", data.shape
    #print "Data Sample:"
    #print data[0:4,0:3]
    #print "----------------------------------------"

def loadarrays(fname):
    #Load the raw data, the calibration array from the files.
    #Create a vector rows,cols for later and save raw transpose to file.
    #Strip the frequency and bias labels and save them for later.
    #Save the transpose to file for comparison
    #print "-------------LoadArrays-------------"
    raw = np.loadtxt(fname)
    #cal = np.loadtxt(cname)
    tp = np.transpose(raw,axes=None)
    np.savetxt("t-"+fname+".tp", tp, fmt='%.8g')
    freq=tp[0]
    bias=tp[:,0]
    range, step = pickrange(bias)
    print "Using calibration file:", range+step
    cal = np.loadtxt(range+step)
    data=tp[1:,1:]
    print "Arrays Loaded OK"
    print "Tranpose Saved OK"
    #print "----------------------------------------"

    return raw,cal,freq,bias,data, tp

def pickrange(bias):
    step = bias[3]-bias[2]
    if step==25:
        print "Step is 25MHz"
        step = str("25.dat")
    elif step==50:
        print "Step is 50MHz"
        step = str("50.dat")
    elif step==100:
        print "Step is 100MHz"
        step = str("100.dat")
    else:
        print "****Frequency Step does not match any Calibration File*****"
    if bias[2]>2000:
        print "Frequency Range is HIGH"
        print "Using Agilent Power Data"
        range="Ag5L"
    else:
```

```
        print "Frequency Range is LOW"
        print "Using HP Power Data"
        range="HP5L"
    return range, step

def normalize(cal,averages):
        #print "---------Normalize----------"
        #raw_input("Press ENTER to Continue")
        cal=cal[:,1]
        print "Averages Shape", averages.shape
        #print "Averaged Array Sample:"
        #print averages[0:5,0:3]
        cal=cal[:,None]
        print "Cal Shape", cal.shape
        #print "Sample Cal:", cal[:5]
        norm = averages/cal
        #print "Normalized Sample:"
        #print norm[0:5,0:3]
        print "Data Normalized using Calibration OK"
        print "Normalized Shape:", norm.shape
        #print "--------------------------------------"
        return norm

def average (n,data,rows,cols):
    #Create an array where each value is the cumulative sum of the previous values in
that column
    #Then add a row of zeroes to the end
    print "--------------Averages------------"
    nhalf=(n-1)/2
    cumsum=data.cumsum(axis=0)
    cumsum=np.row_stack((np.zeros(cols),cumsum))
    #determine length of array, then subtract nhalf.
    #create an ascending 1D  integer array with the same number of columns as the
data
    #1,2,3,4,5,6,7,8,9,10,11,12,13,14,15....
    #then, subtract the (n-1)/2 value.
    #use that to create two arrarys: start (1D array - nhalf) and end (1D array +nhalf+1)
    # the difference between those arrays is the width
    start = np.clip(np.arange(data.shape[0])-nhalf, 0, data.shape[0])
    end = np.clip(np.arange(data.shape[0])+nhalf+1, 0, data.shape[0])
    width = (end-start)[:,None]
    #print "Start, End, Width", start, end, width
    #calculate averages
    averages=(cumsum[end]-cumsum[start])/width
    print "Data Smoothed by Adjacent Average ", n
    print "     Averages Shape:",averages.shape
```

```
    #print "---------------------------------------"
    return averages

def save(averages, freq, bias, norm, scaled):
    #SECTION 5 : REATTACH LABELS AND SAVE
    # Attach Freq and Bias arrays to average array
    # Print a sample of the averaged array, its shape
    # Save the averaged array to a file
    print "--------------Save-------------"
    #print "Averages Shape:", averages.shape
    #print "Normalized Shape:", norm.shape
    #print "Freq Labels Shape:", freq[1:].shape
    #print "Bias Labels Shape:", bias.shape
    averages=np.row_stack((freq[1:],averages))
    averages=np.column_stack((bias,averages))
    np.savetxt("a"+sys.argv[2]+".a", averages, fmt='%.8g')
    print "Averages Saved OK"
    norm=np.row_stack((freq[1:],norm))
    norm=np.column_stack((bias,norm))
    np.savetxt("n"+sys.argv[2]+".n", norm, fmt='%.8g')
    print "Normalized Saved OK"
    scaled=np.row_stack((freq[1:],scaled))
    scaled=np.column_stack((bias,scaled))
    np.savetxt("s"+sys.argv[2]+".s", scaled, fmt='%.8g')
    print "Scaled Saved OK"
    print "Output Files: Adjacent-Average Smoothed Data:","a"+sys.argv[2]+".a"
    print "Output Files: Tranposed Original Data:", "t-"+sys.argv[2]+".tp"
    print "Output Files: Normalized Data:", "n"+sys.argv[2]+".n"
    print "Output Files: Scaled Data:", "s"+sys.argv[2]+".s"
    print "----------------------------------------"
    return 0

def scale(norm):
    #print np.amax(norm, axis=1)
    scaled=norm/np.amax(norm,axis=0)[None,:]
    print scaled[0:5,0:5]
    return scaled

intro(n)
raw,cal,freq,bias,data, tp=loadarrays(fname)
printstuff(raw,cal,freq,bias,data)
rows,cols=(data.shape)
averages=average(n,data,rows,cols)
norm=normalize(cal,averages)
scaled=scale(norm)
save(averages,freq,bias, norm, scaled)
```

Appendix B

Diode J3

The channel in diode J3 is buried in photoresist and exhibits different junction capacitance behavior from the devices discussed in chapter 6, as seen in Figure B.1. A constant-capacitance model is not sufficient to explain the observed change in cut-off frequency with junction bias. The data show good agreement with an exponential dependence on the junction voltage, equation B.1 below:

$$C_J(V_J) = A_0 e^{(\beta V_J)} \qquad \text{(Eq. B.1)}$$

using an exponent β of 4.4 V^{-1} and a pre-factor A_0 of 3.5×10^{-17} F.

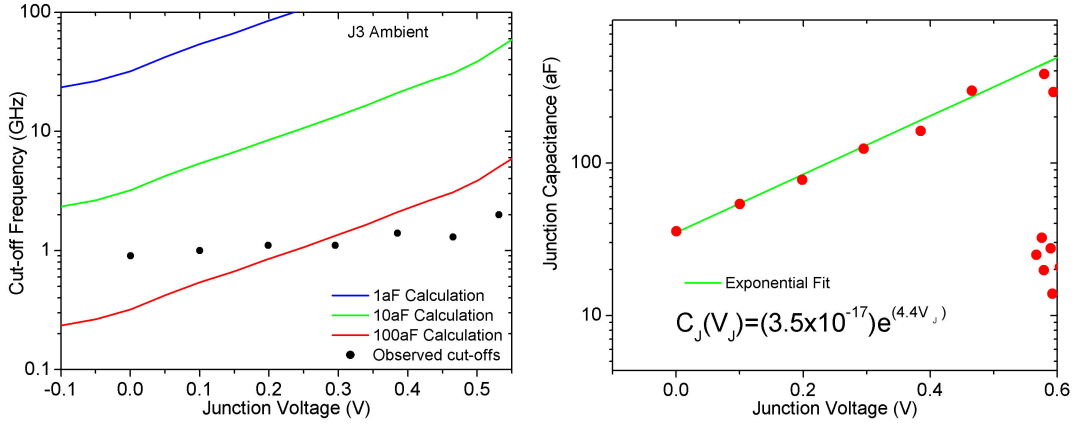

Figure B.1. Microwave rectification parameters for device J3 under ambient conditions. (left) Observed cut-off frequency (black circles) as a function of junction voltage (V_J) compared to simulated results of equation 6.2 using the observed R_S and

$R_J(V_J)$ values and junction capactances of 1 aF (red line), 10 aF (green line) and 100 aF (blue line). (right) Junction capacitance as a function of junction voltage (V_J) calculated from equation 6.3, fitted to an exponential dependence on junction voltage using Equation B.1.

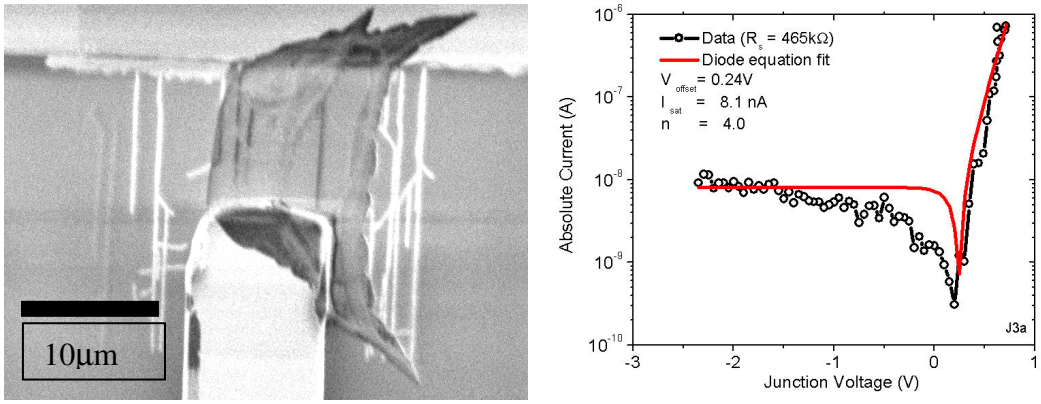

Figure B.2. Left: SEM image of diode J3, comprised of a small but unknown number of nanotubes buried under photoresist residue. Right: Schottky junction IV curve for device J3 in terms of junction bias (black circles) with a fit to the diode equation (red line).

However, the photoresist residue shown in figure B.2 remained in place despite increasingly harsher attempts to remove it (including a long soak in 50C Remover PG). This residue complicates the model of junction capacitance by changing the dielectric constant of the tube's environment or by altering the doping of the nanotube.

Bibliography

1. Iijima, S., Helical microtubules of graphitic carbon. *Nature* **1991,** *354* (6348), 56-58.

2. Wang, X.; Li, Q.; Xie, J.; Jin, Z.; Wang, J.; Li, Y.; Jiang, K.; Fan, S., Fabrication of Ultralong and Electrically Uniform Single-Walled Carbon Nanotubes on Clean Substrates. *Nano Letters* **2009**, 3137-3141.

3. Kong, J.; Cassell, A. M.; Dai, H. J., Chemical vapor deposition of methane for single-walled carbon nanotubes. *Chemical Physics Letters* **1998,** *292* (4-6), 567-574.

4. Cassell, A. M.; Raymakers, J. A.; Kong, J.; Dai, H. J., Large scale CVD synthesis of single-walled carbon nanotubes. *Journal of Physical Chemistry B* **1999,** *103* (31), 6484-6492.

5. Che, G.; Lakshmi, B. B.; Martin, C. R.; Fisher, E. R.; Ruoff, R. S., Chemical vapor deposition based synthesis of carbon nanotubes and nanofibers using a template method. *Chemistry of Materials* **1998,** *10* (1), 260-267.

6. Ebbesen, T. W.; Ajayan, P. M., Large-scale synthesis of carbon nanotubes. *Nature* **1992,** *358* (6383), 220-222.

7. Yudasaka, M.; Komatsu, T.; Ichihashi, T.; Iijima, S., Single-wall carbon nanotube formation by laser ablation using double-targets of carbon and metal. *Chemical Physics Letters* **1997,** *278* (1-3), 102-106.

8. Binning, G.; Rohrer, H.; Gerber, C.; Weibel, E., Surface studies by scanning tunneling microscopy. *Physical Review Letters* **1982,** *49* (1), 57-61.

9. Binnig, G.; Quate, C. F.; Gerber, C., Atomic force microscope. *Physical Review Letters* **1986,** *56* (9), 930-933.

10. Semiconductors, I. T. R. f., International Technology Roadmap for Semiconductors 2009.

11. Guo, J.; Hasan, S.; Javey, A.; Bosman, G.; Lundstrom, M., Assessment of high-frequency performance potential of carbon nanotube transistors. *Ieee Transactions on Nanotechnology* **2005,** *4* (6), 715-721.

12. Zhang, M.; Huo, X.; Chan, P. C. H.; Liang, Q.; Tang, Z. K., Radio-frequency transmission properties of carbon nanotubes in a field-effect transistor configuration. *Ieee Electron Device Letters* **2006,** *27* (8), 668-670.

13. Tseng, Y. C.; Bokor, J., Characterization of the junction capacitance of metal-semiconductor carbon nanotube Schottky contacts. *Applied Physics Letters* **2010,** *96* (1).

14. McEuen, P.; Fuhrer, M.; Park, H., Single-walled carbon nanotube electronics. *Ieee Transactions on Nanotechnology* **2002**, 78-85.

15. Dragoman, D.; Dragoman, M., Terahertz oscillations in semiconducting carbon nanotube resonant-tunneling diodes. *Physica E-Low-Dimensional Systems & Nanostructures* **2004,** *24* (3-4), 282-289.

16. Dragoman, D.; Dragoman, M., Terahertz continuous wave amplification in semiconductor carbon nanotubes. *Physica E-Low-Dimensional Systems & Nanostructures* **2005,** *25* (4), 492-496.

17. Hagmann, M. J., Isolated carbon nanotube's as high-impedance transmission lines for microwave through terahertz frequencies. *Ieee Transactions on Nanotechnology* **2005,** *4* (2), 289-296.

18. Manohara, H. M.; Wong, E. W.; Schlecht, E.; Hunt, B. D.; Siegel, P. H., Carbon nanotube Schottky diodes using Ti-Schottky and Pt-Ohmic contacts for high frequency applications. *Nano Letters* **2005,** *5* (7), 1469-1474.

19. Akturk, A.; Goldsman, N.; Pennington, G.; Wickenden, A., Terahertz current oscillations in single-walled zigzag carbon nanotubes. *Physical Review Letters* **2007,** *98* (16).

20. Portnoi, M. E.; Kibis, O. V.; da Costa, M. R., Terahertz applications of carbon nanotubes. *Superlattices and Microstructures* **2008,** *43* (5-6), 399-407.

21. Vanwees, B. J.; Vanhouten, H.; Beenakker, C. W. J.; Williamson, J. G.; Kouwenhoven, L. P.; Vandermarel, D.; Foxon, C. T., Quantized conductance of point contacts in a two-dimensional electron-gas. *Physical Review Letters* **1988,** *60* (9), 848-850.

22. Bockrath, M.; Cobden, D.; McEuen, P.; Chopra, N.; Zettl, A.; Thess, A.; Smalley, R., Single-electron transport in ropes of carbon nanotubes. *Science* **1997**, 1922-1925.

23. Frank, S.; Poncharal, P.; Wang, Z. L.; de Heer, W. A., Carbon nanotube quantum resistors. *Science* **1998,** *280* (5370), 1744-1746.

24. Burke, P. J., AC performance of nanoelectronics: towards a ballistic THz nanotube transistor. *Solid-State Electronics* **2004,** *48* (10-11), 1981-1986.

25. Rutherglen, C.; Burke, P., Nanoelectromagnetics: Circuit and Electromagnetic Properties of Carbon Nanotubes. *Small* **2009**, 884-906.

26. Averin, D. V.; Likharev, K. K., Coulomb blockade of single-electron tunneling, and coherent oscillations in small tunnel-junctions. *Journal of Low Temperature Physics* **1986,** *62* (3-4), 345-373.

27. Tomonaga, S., Remarks on Bloch's method of sound waves applied to many-fermion problems. *Progress of Theoretical Physics* **1950,** *5* (4), 544-569.

28. Luttinger, J. M., An exactly soluble model of a many-fermion system. *Journal of Mathematical Physics* **1963,** *4* (9), 1154-&.

29. Tarkiainen, R.; Ahlskog, M.; Penttila, J.; Roschier, L.; Hakonen, P.; Paalanen, M.; Sonin, E., Multiwalled carbon nanotube: Luttinger versus Fermi liquid. *Physical Review B* **2001,** *64* (19).

30. Burke, P. J., Luttinger liquid theory as a model of the gigahertz electrical properties of carbon nanotubes. *Ieee Transactions on Nanotechnology* **2002,** *1* (3), 129-144.

31. Bykov, V. T.; Lukyanovich, V. M.; Radushkevich, L. V., *PRIRODNYE SORBENTY DALNEGO VOSTOKA .1. ELEKTRONNO-MIKROSKOPICHESKIE ISSLEDOVANIYA PRIRODNYKH SORBENTOV. *Izvestiya Akademii Nauk Sssr-Seriya Khimicheskaya* **1952,** (3), 406-&.

32. Monthioux, M.; Kuznetsov, V. L., Who should be given the credit for the discovery of carbon nanotubes? *Carbon* **2006,** *44* (9), 1621-1623.

33. Tennent, H. G. Carbon fibrils, method for producing same and compositions containing same. 1987.

34. Hamada, N.; Sawada, S.; Oshiyama, A., New one-dimensional conductors - graphitic microtubules. *Physical Review Letters* **1992,** *68* (10), 1579-1581.

35. Saito, R.; Fujita, M.; Dresselhaus, G.; Dresselhaus, M. S., Electronic-structure of chiral graphene tubules. *Applied Physics Letters* **1992,** *60* (18), 2204-2206.

36. Mintmire, J.; White, C., Electronic and structural-properties of carbon nanotubes. *Carbon* **1995**, 893-902.

37. Iijima, S.; Ichihashi, T., Single-shell carbon nanotubse of 1-nm diameter. *Nature* **1993,** *363* (6430), 603-605.

38. Bethune, D. S.; Kiang, C. H.; Devries, M. S.; Gorman, G.; Savoy, R.; Vazquez, J.; Beyers, R., Cobalt-catalyzed growth of carbon nanotubes with single-atomic-layer walls. *Nature* **1993,** *363* (6430), 605-607.

39. Kroto, H. W.; Heath, J. R.; Obrien, S. C.; Curl, R. F.; Smalley, R. E., C-60 - Buckminsterfullerene. *Nature* **1985,** *318* (6042), 162-163.

40. Drexler, K. E., *Engines of creation*. 1st ed.; Anchor Press/Doubleday: Garden City, N.Y., 1986; p xii, 298 p.

41. Yu, M.; Lourie, O.; Dyer, M.; Moloni, K.; Kelly, T.; Ruoff, R., Strength and breaking mechanism of multiwalled carbon nanotubes under tensile load. *Science* **2000**, 637-640.

42. Berber, S.; Kwon, Y.; Tomanek, D., Unusually high thermal conductivity of carbon nanotubes. *Physical Review Letters* **2000**, 4613-4616.

43. Wallace, P. R., The band theory of graphite. *Physical Review* **1947,** *71* (9), 622-634.

44. Ajiki, H.; Ando, T., Electronic states of carbon nanotubes. *Journal of the Physical Society of Japan* **1993,** *62* (4), 1255-1266.

45. Ouyang, M.; Huang, J. L.; Cheung, C. L.; Lieber, C. M., Energy gaps in "metallic" single-walled carbon nanotubes. *Science* **2001,** *292* (5517), 702-705.

46. Wagner, R. S.; Ellis, W. C., Vapor-liquid-solid mechanism of single crystal growth (new method growth catalysis from impurity whisker epitaxial + large crystal Si e). *Applied Physics Letters* **1964,** *4* (5), 89-&.

47. Sinnott, S. B.; Andrews, R.; Qian, D.; Rao, A. M.; Mao, Z.; Dickey, E. C.; Derbyshire, F., Model of carbon nanotube growth through chemical vapor deposition. *Chemical Physics Letters* **1999,** *315* (1-2), 25-30.

48. Kukovitsky, E. F.; L'Vov, S. G.; Sainov, N. A., VLS-growth of carbon nanotubes from the vapor. *Chemical Physics Letters* **2000,** *317* (1-2), 65-70.

49. Vinciguerra, V.; Buonocore, F.; Panzera, G.; Occhipinti, L., Growth mechanisms in chemical vapour deposited carbon nanotubes. *Nanotechnology* **2003,** *14* (6), 655-660.

50. Nikolaev, P.; Bronikowski, M. J.; Bradley, R. K.; Rohmund, F.; Colbert, D. T.; Smith, K. A.; Smalley, R. E., Gas-phase catalytic growth of single-walled carbon nanotubes from carbon monoxide. *Chemical Physics Letters* **1999,** *313* (1-2), 91-97.

51. Li, X. L.; Tu, X. M.; Zaric, S.; Welsher, K.; Seo, W. S.; Zhao, W.; Dai, H. J., Selective synthesis combined with chemical separation of single-walled carbon nanotubes for chirality selection. *Journal of the American Chemical Society* **2007,** *129* (51), 15770-+.

52. Zheng, M.; Semke, E. D., Enrichment of single chirality carbon nanotubes. *Journal of the American Chemical Society* **2007,** *129* (19), 6084-+.

53. Kong, J.; Franklin, N. R.; Zhou, C. W.; Chapline, M. G.; Peng, S.; Cho, K. J.; Dai, H. J., Nanotube molecular wires as chemical sensors. *Science* **2000,** *287* (5453), 622-625.

54. Wang, J., Carbon-nanotube based electrochemical biosensors: A review. *Electroanalysis* **2005,** *17* (1), 7-14.

55. Pandana, H.; Aschenbach, K. H.; Lenski, D. R.; Fuhrer, M. S.; Khan, J.; Gomez, R. D., A versatile biomolecular charge-based sensor using oxide-gated carbon nanotube transistor arrays. *Ieee Sensors Journal* **2008,** *8* (5-6), 655-660.

56. Landauer, R., Spatial variation of curretns and fields due to localized scatterers in metallic conduction. *IBM Journal of Research and Development* **1957,** *1* (3), 223-231.

57. Landauer, R., Electrical transport in open and closed systems. *Zeitschrift Fur Physik B-Condensed Matter* **1987,** *68* (2-3), 217-228.

58. Kong, J.; Yenilmez, E.; Tombler, T. W.; Kim, W.; Dai, H. J.; Laughlin, R. B.; Liu, L.; Jayanthi, C. S.; Wu, S. Y., Quantum interference and ballistic transmission in nanotube electron waveguides. *Physical Review Letters* **2001,** *87* (10), art. no.-106801.

59. Javey, A.; Guo, J.; Wang, Q.; Lundstrom, M.; Dai, H. J., Ballistic carbon nanotube field-effect transistors. *Nature* **2003,** *424* (6949), 654-657.

60. **Why 50 Ohms?** http://www.microwaves101.com/encyclopedia/why50ohms.cfm (accessed 8/30/2010).

61. Ilani, S.; Donev, L. A. K.; Kindermann, M.; McEuen, P. L., Measurement of the quantum capacitance of interacting electrons in carbon nanotubes. *Nature Physics* **2006,** *2* (10), 687-691.

62. Purewal, M. S.; Hong, B. H.; Ravi, A.; Chandra, B.; Hone, J.; Kim, P., Scaling of resistance and electron mean free path of single-walled carbon nanotubes. *Physical Review Letters* **2007,** *98* (18), 4.

63. Ghanem, T. Electronic transport in low dimensions: carbon nanotubes and mesoscopic silver wires. University of Maryland, College Park, 2008.

64. Zhong, Z.; Gabor, N.; Sharping, J.; Gaeta, A.; McEuen, P., Terahertz time-domain measurement of ballistic electron resonance in a single-walled carbon nanotube. *Nature Nanotechnology* **2008**, 201-205.

65. Baloch, K. Thermal Imaging of Multiwalled Carbon Nanotubes. University of Maryland, College Park, MD, 2010.

66. Leonard, F.; Tersoff, J., Novel length scales in nanotube devices. *Physical Review Letters* **1999,** *83* (24), 5174-5177.

67. Mattis, D. C.; Lieb, E. H., Exact solution of a many-fermion system and its associated boson field. *Journal of Mathematical Physics* **1965,** *6* (2), 304-&.

68. Postma, H. W. C.; Teepen, T.; Yao, Z.; Grifoni, M.; Dekker, C., Carbon nanotube single-electron transistors at room temperature. *Science* **2001,** *293* (5527), 76-79.

69. Salahuddin, S.; Lundstrom, M.; Datta, S., Transport effects on signal propagation in quantum wires. *Ieee Transactions on Electron Devices* **2005,** *52* (8), 1734-1742.

70. Bardeen, J., Surface states and rectification at a metal-semiconductor contact. *Physical Review* **1947,** *71* (10), 717-727.

71. Aguirre, C. M.; Levesque, P. L.; Paillet, M.; Lapointe, F.; St-Antoine, B. C.; Desjardins, P.; Martel, R., The Role of the Oxygen/Water Redox Couple in

Suppressing Electron Conduction in Field-Effect Transistors. *Advanced Materials* **2009,** *21* (30), 3087-+.

72. Suzuki, S.; Bower, C.; Watanabe, Y.; Zhou, O., Work functions and valence band states of pristine and Cs-intercalated single-walled carbon nanotube bundles. *Applied Physics Letters* **2000,** *76* (26), 4007-4009.

73. Suzuki, S.; Watanabe, Y.; Homma, Y.; Fukuba, S.; Heun, S.; Locatelli, A., Work functions of individual single-walled carbon nanotubes. *Applied Physics Letters* **2004,** *85* (1), 127-129.

74. Okazaki, K.; Nakato, Y.; Murakoshi, K., Absolute potential of the Fermi level of isolated single-walled carbon nanotubes. *Physical Review B* **2003,** *68* (3).

75. Vanalme, G. M.; Goubert, L.; Van Meirhaeghe, R. L.; Cardon, F.; Van Daele, P., A ballistic electron emission microscopy study of barrier height inhomogeneities introduced in Au/III-V semiconductor Schottky barrier contacts by chemical pretreatments. *Semiconductor Science and Technology* **1999,** *14* (9), 871-877.

76. Zhu, S. Y.; Van Meirhaeghe, R. L.; Detavernier, C.; Cardon, F.; Ru, G. P.; Qu, X. P.; Li, B. Z., Barrier height inhomogeneities of epitaxial CoSi2 Schottky contacts on n-Si (100) and (111). *Solid-State Electronics* **2000,** *44* (4), 663-671.

77. Palm, H.; Arbes, M.; Schulz, M., Fluctutations of the Au-Si(100) Schottky-barrier height. *Physical Review Letters* **1993,** *71* (14), 2224-2227.

78. Chen, Z. H.; Appenzeller, J.; Knoch, J.; Lin, Y. M.; Avouris, P., The role of metal-nanotube contact in the performance of carbon nanotube field-effect transistors. *Nano Letters* **2005,** *5* (7), 1497-1502.

79. Freitag, M.; Radosavljevic, M.; Zhou, Y. X.; Johnson, A. T.; Smith, W. F., Controlled creation of a carbon nanotube diode by a scanned gate. *Applied Physics Letters* **2001,** *79* (20), 3326-3328.

80. Heinze, S.; Tersoff, J.; Martel, R.; Derycke, V.; Appenzeller, J.; Avouris, P., Carbon nanotubes as Schottky barrier transistors. *Physical Review Letters* **2002,** *89* (10).

81. Appenzeller, J.; Knoch, J.; Derycke, V.; Martel, R.; Wind, S.; Avouris, P., Field-modulated carrier transport in carbon nanotube transistors. *Physical Review Letters* **2002,** *89* (12).

82. Sze, S. M. a. N., Kwok K., *Physics of Semiconductor Devices*. Third Edition ed.; John Wiley & Sons Inc: Hoboken, NJ, 2007.

83. Mohammad, S. N., Contact mechanisms and design principles for (Schottky and Ohmic) metal contacts to semiconductor nanowires. *Journal of Applied Physics* **2010,** *108* (3).

84. Cowley, A. M.; Sorensen, H. O., Quantitative comparison of solid-state microwave detectors. *Ieee Transactions on Microwave Theory and Techniques* **1966,** *MT14* (12), 588-&.

85. Jarillo-Herrero, P.; Sapmaz, S.; Dekker, C.; Kouwenhoven, L. P.; van der Zant, H. S. J., Electron-hole symmetry in a semiconducting carbon nanotube quantum dot. *Nature* **2004,** *429* (6990), 389-392.

86. Yoneya, N.; Watanabe, E.; Tsukagoshi, K.; Aoyagi, Y., Coulomb blockade in multiwalled carbon nanotube island with nanotube leads. *Applied Physics Letters* **2001,** *79* (10), 1465-1467.

87. Durkop, T.; Getty, S. A.; Cobas, E.; Fuhrer, M. S., Extraordinary mobility in semiconducting carbon nanotubes. *Nano Letters* **2004,** *4* (1), 35-39.

88. Pesetski, A. A.; Baumgardner, J. E.; Folk, E.; Przybysz, J. X.; Adam, J. D.; Zhang, H., Carbon nanotube field-effect transistor operation at microwave frequencies. *Applied Physics Letters* **2006,** *88* (11).

89. Jarillo-Herrero, P.; Sapmaz, S.; Dekker, C.; Kouwenhoven, L. P.; Zant, H. S. J. v. d., Electron-hole symmetry in a semiconducting carbon nanotube quantum dot. *Nature* **2004,** *429*, 389-392.

90. Postma, H. W. C.; Teepen, T.; Yao, Z.; Grifoni, M.; Dekker, C., Carbon Nanotube Single-Electron Transistors at Room Temperature. *Science* **2001,** *293*, 76-79.

91. Tarkiainen, R.; Ahlskog, M.; Penttila, J.; Roschier, L.; Hakonen, P.; Paalanen, M.; Sonin, E., Multiwalled carbon nanotube: Luttinger versus Fermi liquid. *Physical Review B* **2001,** *64*, 195412:1-4.

92. Kocabas, C.; Hur, S.; Gaur, A.; Meitl, M.; Shim, M.; Rogers, J., Guided growth of large-scale, horizontally aligned arrays of single-walled carbon nanotubes and their use in thin-film transistors. *Small* **2005**, 1110-1116.

93. Ding, L.; Tselev, A.; Wang, J. Y.; Yuan, D. N.; Chu, H. B.; McNicholas, T. P.; Li, Y.; Liu, J., Selective Growth of Well-Aligned Semiconducting Single-Walled Carbon Nanotubes. *Nano Letters* **2009,** *9* (2), 800-805.

94. Hong, S. W.; Banks, T.; Rogers, J. A., Improved Density in Aligned Arrays of Single-Walled Carbon Nanotubes by Sequential Chemical Vapor Deposition on Quartz. *Advanced Materials* **2010,** *22* (16), 1826-+.

95. Li, Y.; Cui, R. L.; Ding, L.; Liu, Y.; Zhou, W. W.; Zhang, Y.; Jin, Z.; Peng, F.; Liu, J., How Catalysts Affect the Growth of Single-Walled Carbon Nanotubes on Substrates. *Advanced Materials* **2010,** *22* (13), 1508-1515.

96. Rutkowska, A.; Walker, D.; Gorfman, S.; Thomas, P. A.; Macpherson, J. V., Horizontal Alignment of Chemical Vapor-Deposited SWNTs on Single-Crystal Quartz Surfaces: Further Evidence for Epitaxial Alignment. *Journal of Physical Chemistry C* **2009,** *113* (39), 17087-17096.

97. Yuan, D. N.; Ding, L.; Chu, H. B.; Feng, Y. Y.; McNicholas, T. P.; Liu, J., Horizontally aligned single-walled carbon nanotube on quartz from a large variety of metal catalysts. *Nano Letters* **2008,** *8* (8), 2576-2579.

98. Li, Y. M.; Kim, W.; Zhang, Y. G.; Rolandi, M.; Wang, D. W.; Dai, H. J., Growth of single-walled carbon nanotubes from discrete catalytic nanoparticles of various sizes. *Journal of Physical Chemistry B* **2001,** *105* (46), 11424-11431.

99. Theil, E. C., Ferritin - structure, gene-regulation and cellular function in animals, plants and microorganisms. *Annual Review of Biochemistry* **1987,** *56*, 289-315.

100. Kocabas, C., Kim, H., Banks, T., Rogers, J. A., Pesetski, A. A., Baumgardner, J. E., Krishnaswamy and Zhang, H., Radio frequency analog electronics based on carbon nanotubes transitors. *Proceedings of the National Academies of Sciences* **105** (5), 1405-1409, 2008.

101. Kocabas, C., Dunham, S., Cao, Q., Cimino, K., Ho, X., Kim, H., Dawson, D., Payne, J., Stuenkei, M., Zhang, H., Banks, T., Feng, M., Rotkin, S. V., Rogers, J. A. *Nano Letters* **9** (5), 1937-1943, 2009.

102. Nougaret, L., Happy, H., Dambrine, G., Bourgoin, J. P., Green, A. A., Hersam, M. C. 80 GHz field-effect transistors produced using high purity semiconducting single-walled carbon nanotubes, *Applied Physics Letters* **94**, 243505-1, 2009.

103. Yu, Z., Rutherglen, C., Burke, R. J., Microwave nanotube transistor operation at high bias, *Applied Physics Letters* **88 (**23), 233115, 2006.

104. Ho, X., Ye, L., Rotkin, S. V., Xie, X., Du, F., Dunham, S., Zaumseil, J., Rogers, J. A., Theoretical and experimental studies of Schottky diodes that use aligned arrays of single-walled carbon nanotubes, *Nano Research*, **3** (6), 444-451, 2010.

105. Cobas, E. and Fuhrer, M.S., Microwave rectification by a carbon nanotube Schottky diode, *Applied Physics Letters* **93** 043120, 2008.